University of Groningen

Faculty of Science and Engineering, Kapteyn Institute

Cold Molecular Gas in Gravitationally Lensed AGN HE1104−1805

Determining Velocity Structure and Source Characteristics using CO(1-0) Emission

Thesis BSc Astronomy

Author:
Sebastiaan N. Venendaal
venendaal(at)astro.rug.nl

Supervisor:
Prof. Dr. John P. McKean

Co-supervisor:
Dr. Cristiana Spingola

July 2019

Abstract

In this thesis, we first present an introduction on some fundamental concepts used, followed by an in-depth description of the calibration process. We use 34.7 GHz VLA observations of the gravitationally lensed quasar HE1104−1805 to investigate its velocity structure by using CO(1-0) emission to trace its cold molecular gas. In the created zeroth moment maps, we detect two spatially resolved gravitationally lensed images, separated by $\Delta\theta_{1-0} = 3.4 \pm 0.4$ arcsec. The CO(1-0) spectra show a highly asymmetric double horn profile, with a detection of the lower frequency peak about thrice as strong as the higher frequency peak. We argue this can be caused by differential magnification or a gas in- or outflow. We create velocity fields (first moment maps) with respect to the systemic velocity at $z = 2.3221$ and they all show positively dominated gradients, due to the positive velocity peak dominating over the negative velocity peak. We find that the positive and negative component of the velocity structure are marginally spatially offset. The created dispersion fields (second moment maps) all show a peak velocity dispersion in the centre of the images, indicating a more chaotic gas motion in the AGN region. Using the measured integrated flux density of the CO(1-0) emission of $\mu S_{1-0}\Delta v = 0.49 \pm 0.05$ Jy km s^{-1}, we obtain an apparent CO luminosity of $\mu L'_{\rm CO} = (1.32 \pm 0.13) \times 10^{11}$ K km s^{-1} pc^2. To obtain the gas mass of HE1104−1805, we use a CO-H_2 conversion factor of $\alpha_{\rm CO} = 0.8$ M$_\odot$ (K km s^{-1} pc^2)$^{-1}$, empirically derived from local ULIRGs, and a common estimated magnification factor to find $M_{\rm gas} = (1.1 \pm 0.5) \times 10^{10}$ M$_\odot$. Using an assumed spectral index, we extrapolate our measured integrated flux density of $S_{34.7\rm GHz} = 100 \pm 10$ μJy from the continuum emission at 34.7 GHz to 1.4 GHz and relate this to the rest-frame luminosity at 1.4 GHz, to derive a radio-infrared correlation factor of $q_{\rm IR} = 2.05 \pm 0.27$, consistent with the population of star-forming galaxies. We position HE1104−1805 in the $L_{\rm IR} - L'_{\rm CO}$ plane against the K-S relation for high redshift disk galaxies and find it close to the mean position for local ULIRGs, but with an increased SFE, which indicates HE1104−1805 might be a starburst galaxy. We find the continuum emission to be more compact than the CO(1-0) emission, indicating that its emission region must be more compact than the cold molecular gas. Together with a fit of the heated dust emission, we argue the continuum emission is not dominated by heated dust emission due to star formation. Finally, we suggest additional observations at a higher angular resolution and argue a source plane reconstruction through lens modelling might support further investigations into the velocity structure and continuum origin of HE1104−1805.

Acknowledgements

I would like to thank Cristiana for introducing me to the concept of gravitational lensing and the calibration process of VLA data. Furthermore, I commend her for her seemingly unending enthusiasm and tolerance for my avalanches of 'quick' questions. I would like to thank John for providing me with this opportunity and for supporting me throughout. I would like to thank my friends at Kapteyn, with whom I shared the highs and lows of our first research projects. I would like to thank my friends, wholly unfamiliar with the subjects and concepts of this thesis, but interested nonetheless. I would like to thank my parents and 'little' brother, without whose support I would not have been able to follow my interests this freely. Finally, I would like to thank all Kapteyn staff for providing a wonderful environment for the students.

Contents

1 Introduction **1**
- 1.1 Radio Interferometry . . . 1
- 1.2 Gravitational Lensing . . . 3
- 1.3 Cold Molecular Gas in Active Galactic Nuclei (AGN) . . . 6
- 1.4 CO(1-0) Emission . . . 6
- 1.5 Target: HE1104−1805 . . . 8
- 1.6 This Thesis . . . 9

2 Observations **11**
- 2.1 Karl G. Janksy Very Large Array (VLA) . . . 11
- 2.2 Data Reduction and Calibration . . . 11
  - 2.2.1 Inspection of the Observation . . . 12
  - 2.2.2 A Priori Calibration . . . 12
  - 2.2.3 Flagging . . . 13
  - 2.2.4 Setting the Flux Density Scale . . . 14
  - 2.2.5 Bandpass and Delay Calibration . . . 15
  - 2.2.6 Complex Gain (Phase and Amplitude) Calibration . . . 16
  - 2.2.7 Imaging of the Continuum . . . 16
  - 2.2.8 Subtraction of the Continuum . . . 19
  - 2.2.9 Imaging of the CO(1-0) Line . . . 19

3 Results **22**
- 3.1 D-Configuration . . . 22
  - 3.1.1 Continuum Emission . . . 22
  - 3.1.2 CO(1-0) Emission . . . 22
  - 3.1.3 Velocity Fields . . . 29
- 3.2 C-Configuration . . . 30
  - 3.2.1 Continuum Emission . . . 30
  - 3.2.2 CO(1-0) Emission . . . 30
- 3.3 C&D-Configuration . . . 34
  - 3.3.1 Continuum Emission . . . 34
  - 3.3.2 CO(1-0) Emission . . . 35
  - 3.3.3 Velocity Fields . . . 37

4 Discussion **41**
- 4.1 CO(1-0) Emission at Redshift $z = 2.3221$ . . . 41
  - 4.1.1 Spectrum Properties . . . 41
  - 4.1.2 Structure of the Velocity Field . . . 41
- 4.2 Molecular Gas . . . 42
- 4.3 Star Formation . . . 44
  - 4.3.1 Radio-Infrared Luminosity Relation . . . 44
  - 4.3.2 Kennicutt-Schmidt (K-S) Relation . . . 45
- 4.4 Origin of the Continuum Emission . . . 46

5 Conclusions **50**

References **53**

Chapter 1

Introduction

1.1 Radio Interferometry

For a single dish observation, the angular resolution, θ in rad, can be determined using the Rayleigh criterion (or diffraction limit) as follows,

$$\theta_{\text{dish}} \sim \frac{\lambda}{D}, \tag{1.1}$$

where λ is the observing wavelength and D the diameter of the dish. For example, the Hubble Space Telescope with a primary mirror diameter of 2.4 m can observe at a wavelength of 500 nm (green optical light) with an angular resolution of about 0.05 arcsec. For a single radio telescope to achieve the same angular resolution at mm wavelengths, one would require a dish with a diameter of 5 km. Constructing such a dish, which is also steerable, is practically impossible. For example, the largest fully steerable telescope is the Green Bank Telescope with a 100 m dish diameter. Instead, radio astronomers have been using arrays of antennas to observe the same target simultaneously. The signals observed by the antennas are combined coherently; this is a technique known as interferometry. In contrast to single dish telescopes, for an interferometer the angular resolution is set by the distance between the antennas. The distance between two antennas projected on the plane perpendicular to the incoming signal is called the "baseline" of the two antennas, see Figure 1.1. For an two-element interferometer the angular resolution is now determined using

$$\theta_{\text{array}} \sim \frac{\lambda}{B}, \tag{1.2}$$

where λ is the observing wavelength and B is the baseline length. An array is sensitive to a range of angular sizes, $\lambda/B_{\text{max}} < \theta < \lambda/B_{\text{min}}$, where B_{max} is the maximum baseline and the B_{min} the minimum baseline. This implies that spatial scales larger than the smallest baseline cannot be imaged and spatial scales smaller than the largest baseline cannot be spatially resolved. Since $B_{\text{min}} > D$, an interferometer is not sensitive to the largest angular scales and hence cannot recover the total flux of resolved sources. The sensitivity of an interferometer is set by its total collecting area, the combined surface area of the antennas.

The incoming signal from the target arrives at each antenna at a slightly different time due to the difference in distance travelled. The signals are amplified and digitised at the antennas themselves and combined in the correlator, where this delay is compensated for. Precise and accurate timing is required to do this successfully.

An interferometer measures the interference pattern of the multiple antennas (called the visibilities) over all available baselines (pairs of antennas). The baselines are generally not aligned and span a 'messy' 2D plane structure. The plotted transformation of their projected visibilities on the sky is called the uv-plane, see Figure 1.1. The visibilities describe 2D sinusoids that add up to an image of the sky and are a complex quantity consisting of an amplitude A and a phase ϕ,

$$V(A, \phi) = A\mathrm{e}^{-i\phi}. \tag{1.3}$$

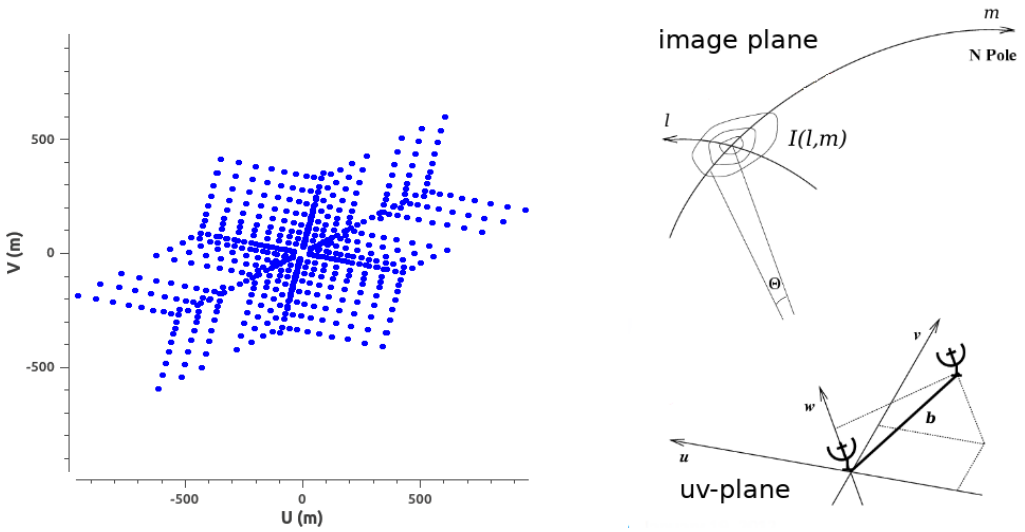

Figure 1.1: Left: Example of a VLA uv-plane in the D-configuration (one frequency channel, one time stamp) **Right:** Schematic depiction of the image plane, with angular coordinates (l, m), and the uv-plane, with spatial coordinates (u, v, w). Source: NRAO (Image altered for use in this thesis).

The visibilities are measured through a baseline vector $\vec{b}$, defining the direction and separation of the antennas. The baseline vector can be expressed in a Cartesian coordinate system (u,v,w). Assuming the measurements take place on a single plane, we can set the w-axis normal to this plane such that

$$\vec{b} = (u, v, w) = (u, v, 0), \tag{1.4}$$

where u and v are commonly given in units of observing wavelength. Therefore, we measure all visibilities in a 2D plane, the uv-plane, defined by the spatial coordinates u and v such that we can simply speak of $V(u, v)$ instead. For small fields of view, the van Cittert-Zernike theorem (Zernike 1938) states that in the small angle approximation the visibility function takes on a simple 2D form,

$$V(u, v) = \iint I(l, m) \mathrm{e}^{2\pi i(ul+vm)} \mathrm{d}l \mathrm{d}m, \tag{1.5}$$

where $I(l, m)$ is the sky brightness distribution and (l,m) are the orthogonal coordinates of the image plane. Finally, the inverse 2D Fourier transform of Eq. 1.5 retrieves the sky brightness distribution as a function of the measured visibilities,

$$I(l, m) = \iint V(u, v) \mathrm{e}^{-2\pi i(ul+vm)} \mathrm{d}u \mathrm{d}v. \tag{1.6}$$

A schematic of both the (u, v, w) and (l, m) coordinate systems is presented in Figure 1.1.

Each visibility samples a discrete point in the uv-plane, giving information about the amount of power on some projected angular size on the sky. The more points in the uv-plane, the more accurate the brightness distribution, as less interpolation is needed. In order to improve on the sampling of the uv-plane, more antennas can be added to increase the number of baselines. Each added antenna N adds a number of $N(N-1)/2$ baselines, therefore many samples in the uv-plane are produced at any given time. Secondly, as the uv-plane coordinates are a function of the observing wavelength, adding frequency channels will increase the radial sampling of the uv-plane. Finally, as the coordinates are dependent on the projected baseline (and not just the distance between the antennas) increasing the observing time also increases the sample amount. This is due to the rotation of the Earth, as it changes the projected baseline lengths over time. These effects are illustrated in Figure 1.2.

Using interferometry, we have been able to achieve excellent angular resolution, even at longer wavelengths. At radio wavelengths, we are able to reach sub-milliarcsec and micro-arcsec angular resolutions.

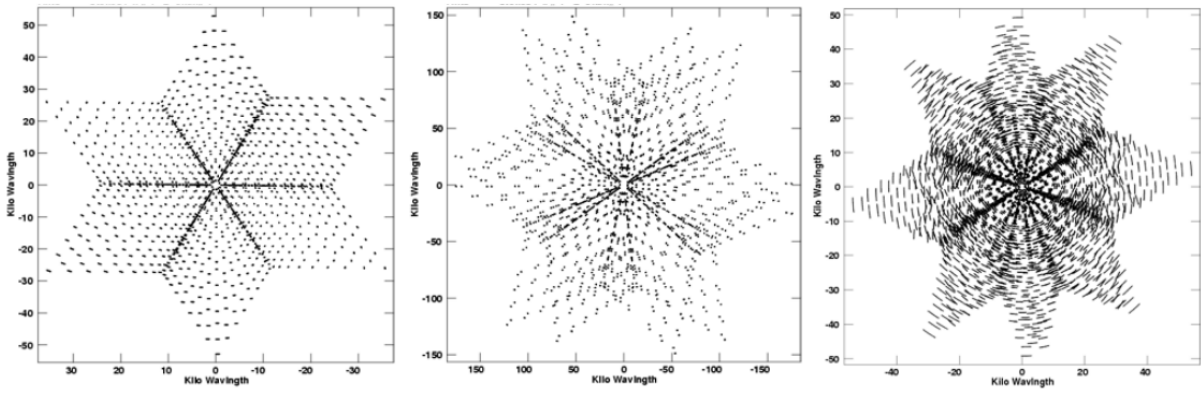

Figure 1.2: Left: Example of a uv-plane of a VLA observation at a single frequency channel and timestamp. **Centre**: Example of a uv-plane with two frequency channels. Note the increased radial sampling. **Right**: Example of a uv-plane with a longer observing time. Note the elongated streaks of visibilities. Source: Lecture slides by McKean (2018).

As an impression, trying to resolve a milliarcsec (one 3.6 millionth of a degree) is like trying to read this thesis at a distance of about one kilometre. Being able to achieve these angular resolutions allows us to study objects in great detail, including high redshift ones.

1.2 Gravitational Lensing

Although we can achieve a high angular resolution using interferometry, we can obtain even higher resolutions when a massive object, such as a galaxy, acts as a telescope. This effect is referred to as "gravitational lensing". Einstein's General Relativity theorem predicts that the presence of matter (a form of energy density) can curve space-time, which will deflect the path of a light ray as a result. This effect is in many cases analogous to the deflection of light by lenses in optics. The effect was the first experimentally verified prediction of General Relativity, when Dyson et al. (1920) found evidence for deflection of light by the Sun's gravitational field.

A lensing system contains the following elements: a background source, one or multiple lenses and an observer, as shown in Figure 1.3. The lenses deflect the light by an amount related to their mass and geometry. The observer sees then the deflected light from the apparent source image(s). The system can be simplified by considering that the light deflection angles are small (weak-field approximation) and that the distances between the elements is much greater than their width (thin-lens approximation). From these assumptions a simplified model can be made and is shown in Figure 1.3. Due to the bending, the images might seem distorted and/or magnified. Furthermore, if more images are present, most likely the paths are not of equal length and hence some of the images will be delayed in time compared to others.

A light ray from the source is deflected towards the observer by an angle $\vec{\hat{\alpha}}(\xi)$, which results in an image of the source at a displaced position. Note that rays straight from the source are most likely deflected away from the observer and hence will not be observed. The angular positions of the apparent image ($\vec{\theta}$) and the source ($\vec{\theta_{\rm S}}$) are related by the lens equation,

$$\vec{\theta_{\rm S}} = \vec{\theta} - \vec{\alpha}(\theta), \tag{1.7}$$

where $\vec{\alpha}(\vec{\theta}) = (D_{\rm L}/D_{\rm S})\vec{\hat{\alpha}}(\vec{\theta})$ is the reduced deflection angle and $\vec{\xi} = D_{\rm LS}\vec{\theta}$ indicates the image position in the lens plane with respect to the lens centre, see Figure 1.3. Describing how the lensed surface brightness distribution in the lens plane is mapped onto the source plane, this equation is fundamental to the concept of gravitational lensing. It becomes more interesting when we consider that the lens equation can support more than one solution $\vec{\theta}$ for a given source position $\vec{\theta_{\rm S}}$. In other words, gravitational lensing can produce more than one image of a single source.

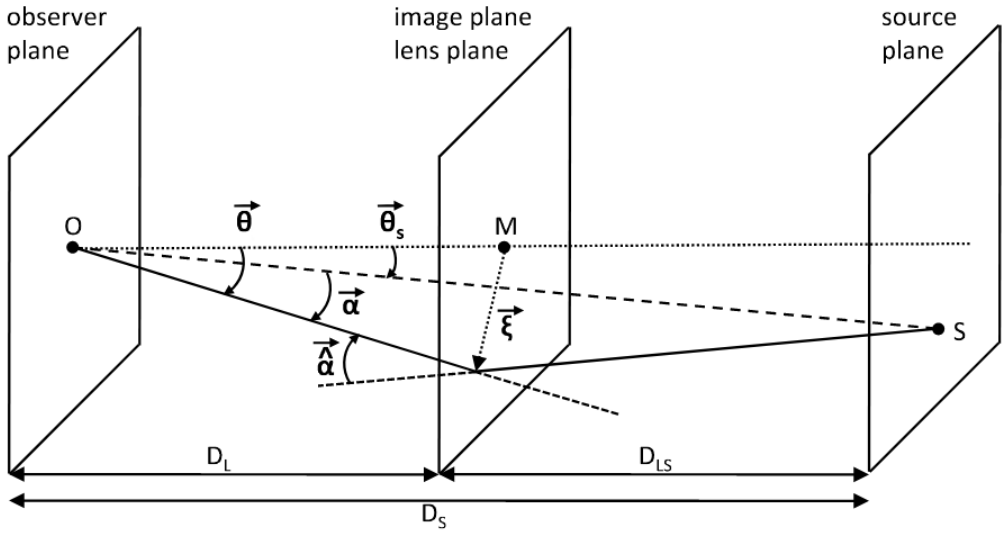

Figure 1.3: Schematic model of a gravitational lensing system containing an observer O, a point-like lens M and a point-like background source S. A light ray from the source S gets deflected by a deflection angle $\vec{\hat{\alpha}}$ at a position $\vec{\xi}$ from the lens centre. The deflected light ray arrives at the observer O and is observed under an angle $\vec{\theta}$. Would there have not been a lens present, the background source would be observed under its true position angle $\vec{\theta_S}$. The observed image of the background source is displaced by the reduced deflection angle $\vec{\alpha}$ with respect to its true position. D_L, D_S and D_{LS} indicate the angular diameter distances between the respective components. Source: Berciano Alba (2009) (Image altered for use in this thesis).

Gravitational lensing events are divided in two main categories: strong lensing and weak lensing. For strong lensing, often the lens is either a galaxy or a cluster of galaxies. For strong lensing to occur, a lens must have a surface mass density greater than the critical surface mass density,

$$\Sigma_{\mathrm{CR}} = \frac{c^2}{4\pi G}\frac{D_{\mathrm{S}}}{D_{\mathrm{L}} D_{\mathrm{LS}}}, \tag{1.8}$$

where the symbols have their aforementioned meaning. If a lens does not meet this criterion, weak lensing occurs. In this case, the lensing is not strong enough to form multiple images or arcs. The image of the source can, however, be distorted. Often this stretches the image, called shear distortion, or magnifies it, called convergence. If the intrinsic properties of the source are known one can use the distorted image to deduce properties of the lens.

In some special cases the source is almost perfectly aligned with the lens, causing light to be deflected such that an annular image, a so-called Einstein ring, can be observed as shown in Figure 1.4. The most common case of gravitational lensing consists of multiple (two or four) compact images of the same background source.

Lensing is a purely geometrical effect, only dependent on gravity and thus the mass (and energy) distribution of the lens(es). Furthermore, it is independent of whether the lensing mass is luminous or dark by nature as well as the dynamical state of the matter. Therefore, gravitational lensing has become a powerful tool in the determination of the amount and distribution of mass in galaxies and galaxy clusters. For small angles of deflection and under the assumption of a point-like mass distribution for the lens, the Einstein radius in radians is given as

$$\theta_{\mathrm{E}} = \left(\frac{4GM}{c^2}\frac{D_{\mathrm{LS}}}{D_{\mathrm{L}} D_{\mathrm{S}}}\right)^{1/2}, \tag{1.9}$$

where M is the mass of the lens enclosed within the Einstein radius and D_{L}, D_{S} and D_{LS} as defined in Figure 1.3 (see derivation by Narayan & Bartelmann (1996)).

One of the most important advantages of gravitational lensing is that it magnifies the background source. The magnification factor, μ, of an image with respect to its source is defined geometrically as

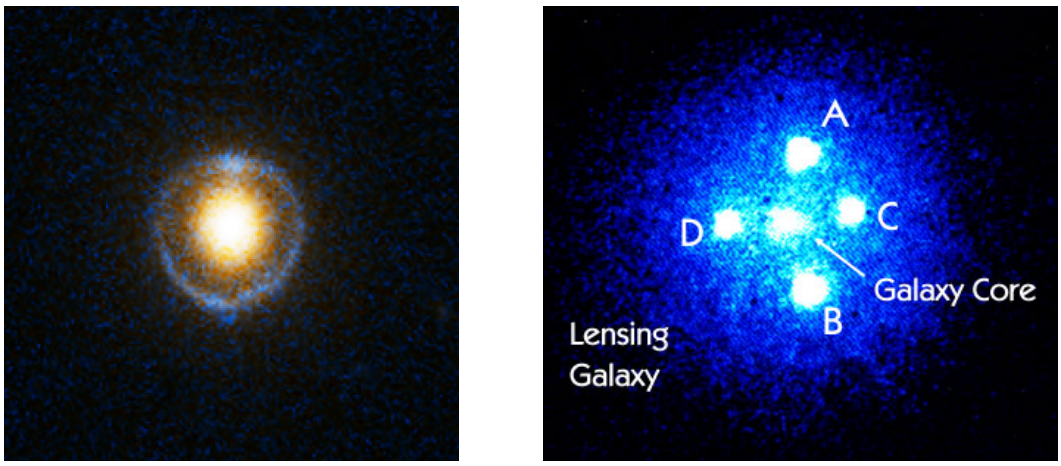

Figure 1.4: Left: A background source (SDSS J162746.44-005357.5) that is gravitationally lensed into an Einstein ring. Source: ESA. **Right**: The Einstein cross (QSO 2237+0305) is a gravitationally lensed quasar. Here, four images (labelled A through D) of the same distant quasar appear around a foreground galaxy due to strong gravitational lensing. Source: SkyHound.

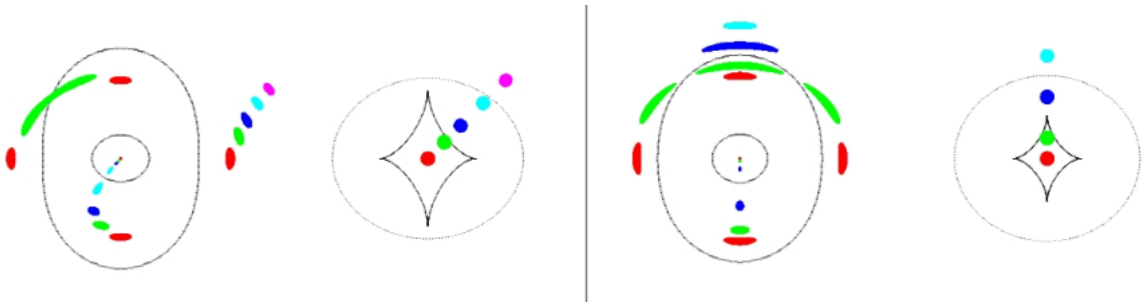

Figure 1.5: Schematic depiction of a source at different positions and its resulting images. The right diagram in both panels depicts the source plane and the caustics. The left diagram depicts the lens plane (the resulting images of the source due to lensing) and the critical curves. Note the position of the sources relative to the caustic lines and the resulting number of images produced. Source: Narayan & Bartelmann (1996).

the ratio between their subtended solid angles,

$$\mu = \frac{\mathrm{d}\Omega_{\mathrm{obs}}}{\mathrm{d}\Omega_{\mathrm{int}}}, \tag{1.10}$$

where $\mathrm{d}\Omega_{\mathrm{obs}}$ is the observed solid angle of the image and $\mathrm{d}\Omega_{\mathrm{int}}$ the intrinsic solid angle of the background source. Liouville's theorem states that the density of states in the phase space of a photon beam remains constant if the interacting forces are non-collisional (like gravity) and if the propagating medium is approximately transparent (like interstellar space) (Mollerach & Roulet 2002). This tells us that the surface brightness of the apparent image compared to its source is conserved in the absence of absorption phenomena, interstellar scattering or Doppler shifts. Therefore we can say $I_{\mathrm{obs}} = I_{\mathrm{int}} = I$, where I stands for surface brightness. The magnification factor hence also tells us the ratio between the measured fluxes of the image and the background source, if it were unlensed.

In the common nomenclature of gravitational lensing, we fine two families of curves, called "caustics" (in the source plane) and "critical curves" (in the lens plane). The position of the background source relative to the caustics determines how many images are created in the lens plane, as shown in Figure 1.5. Sources within the inner caustics create four images, whereas sources outside the inner caustics but inside the outer caustics create only two. Note that in both cases an additional central image is created, but is often heavily de-magnified below the sensitivity level.

1.3 Cold Molecular Gas in Active Galactic Nuclei (AGN)

Although surrounded by vast patches of near emptiness, galaxies are the main building blocks of the Universe. Many show bright cores due to increased star density, but a small fraction are distinguished by their highly luminous nuclei, sometimes even dominating the total emission of their host galaxy. These highly energetic, highly active phenomena in the centre of the building blocks are called Active Galactic Nuclei (AGN). A typical AGN (see Figure 1.6) consists of a central supermassive black hole (SMBH) surrounded by an accretion disk ($R \sim 10^{-3}$-10^{-2} pc), which in turn is surrounded by a molecular dusty torus ($R \sim 10^{2}$-10^{3} pc). The gravity of the SMBH pulls in matter and heats it to incredible temperatures, this together with its morphology results in a range of thermal processes: from optical (VIS), ultraviolet (UV) and X-ray emission due to the central accretion flow of the gas closest to the SMBH, to far-infrared (FIR) emission from the colder dust further away. Some AGN also have jets of relativistic plasma, that are collimated by the dense thermal gas surrounding the nucleus. In these jets, relativistic electrons release synchrotron radiation as they spiral along a magnetic field. Additionally, relativistic charged particles in the accretion flow also emit synchrotron emission as they are accelerated through the magnetic fields embedded in the accretion disk. This synchrotron emission is a non-thermal process, as its radiation does not follow a black-body Planck curve, and is usually responsible for the majority of the observed radio and high energy emission from the AGN. The radio jets can extend up to hundred thousands of parsecs perpendicular to the accretion disk and often end in diffuse radio lobes, see Figure 1.6. The line of sight we have to the AGN determines the types of emission we can observe and plays a role in the classification of the AGN. For instance, if we observe the AGN host galaxy edge-on the emission from the AGN itself is obscured by the dusty torus and cannot be observed. This thesis will use observations of a quasar. For quasars their galaxy axis points towards the Earth such that we can observe all of its emission.

AGN are observed to strongly evolve in time, with the number density of the most luminous AGN increasing by a factor of 10^3 from $z \sim 0$ to $z \sim 2$. This implies that SMBH formed early on in the Universe and that conditions for forming luminous AGN were more common back then. Nowadays, only considerably less luminous or entirely quiescent AGN are observed, indicating something must have quenched the black hole accretion rate over cosmic time. The evolution of AGN, especially low luminosity AGN, is not well understood due to the difficulty of observing these objects at high redshifts.

For a long time, AGN were the highest redshift objects known in the optical and radio due to their high luminosities. Although they still play a significant role in studies of the early universe, it is now known that AGN give a biased picture of the typical high redshift galaxy as we are unable to observe the less luminous ones. For most of the AGN at redshifts $z \sim$ 2-3 the current spatial resolution and sensitivity of interferometric arrays is not good enough to observe them. However, these objects can be magnified by the presence of a gravitational lens and become observable. These objects are especially interesting as observations show that the global star formation rate (SFR) and the SMBH accretion rate trace each other over cosmic time along with the luminous AGN number density, all peaking around $z \sim 2$ (Hirschmann et al. 2014). This co-evolution is thought to be driven by the feedback from the AGN. This can quench the SFR in the host galaxy by introducing an outflow of available matter for star formation, see Figure 1.7, called "negative feedback" (e.g. Croton et al. 2006). Alternatively, the AGN can induce star formation by compressing matter to critical densities, called "positive feedback" (e.g. Ishibashi & Fabian 2012). However, it is currently not clear what the role of AGN is. As (cold) molecular gas regions are the birth chambers of stars, the role of the AGN with respect to the SFR evolution can be clarified by spatially resolving the molecular gas in the AGN and determining its properties.

1.4 CO(1-0) Emission

To trace the molecular gas in the AGN, we need to trace emission (or absorption) from one of its constituents. The first obvious choice would be molecular hydrogen (H_2), as this makes up to about 90% of the molecular gas. However, as H_2 is a symmetric homo-nuclear molecule, it has no dipole moment. Therefore, it is an inefficient radiator, emitting only weak quadrupole transitions ($\Delta J = 2$). Additionally, its small moment of inertia means its energy levels are widely spaced apart and inefficiently populated at the low temperatures typical for molecular clouds. As a result H_2 can only be directly probed weakly in

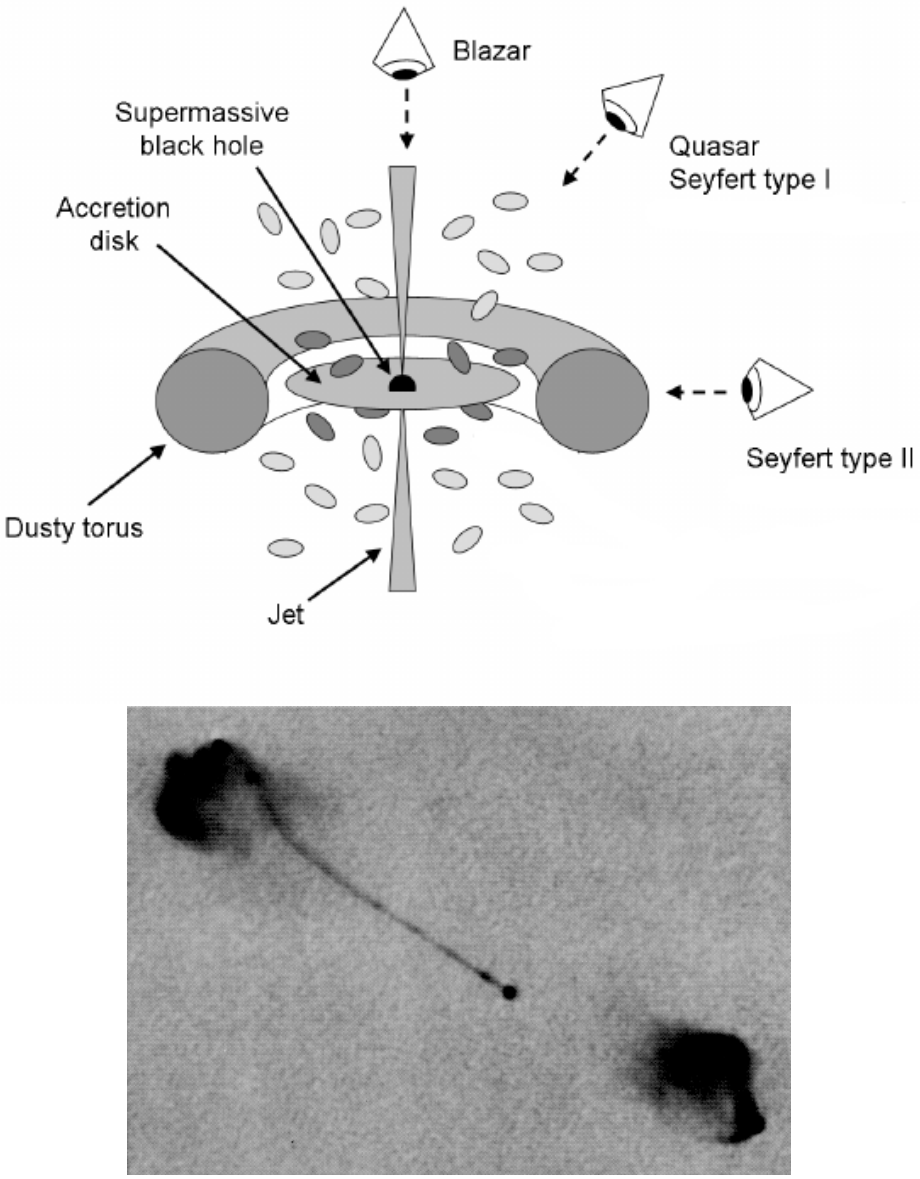

Figure 1.6: Left: Schematic depiction of an AGN. The classification is mainly determined by the observation angle with respect to the galaxy axis, as it determines what types of emission we observe. Source: Zackrisson (2005) (Image altered for use in this thesis). **Right**: VLA image of radio emission from quasar 3C175. The radio source extends about 200 Mpc end-to-end. The central bright part is the region containing the black hole. The two outer lobes mark the end of the two relativistic jets. Source: IPAC-Caltech.

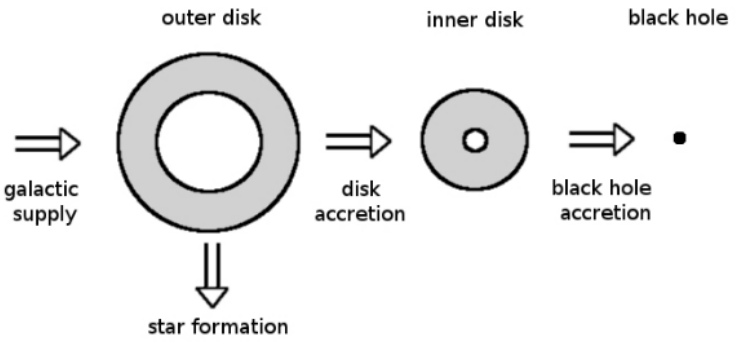

Figure 1.7: Schematic model of the mass flow between the molecular outer disk (dusty torus) and gaseous inner disk (accretion disk). Matter is supplied from the hosting galaxy to the molecular outer disk, which forms stars, reducing the amount of available gas. Through accretion, matter can flow to the accretion disk and be depleted by either the accreting SMBH or an AGN outflow. This mass flow relates star formation and black hole accretion. Source: Wutschik et al. (2013).

the mid/near-IR and UV wavelengths and not in the radio regime. In molecular clouds, carbon monoxide (CO) is the second most abundant molecule by a factor of ten thousand with respect to H_2. As CO does have a dipole moment, its radiation is much stronger and thus easier to detect, more than compensating for its lower abundance. In the microwave regime, multiple transitions of CO are readily observable. Therefore, to trace the molecular gas, observations of CO transitions are commonly used as a proxy for H_2 and these observations are the primary way of identifying giant molecular clouds and determining the corresponding properties.

CO observations are crucial for studies of star formation and galactic structure. Together with observations of HII regions, OB associations and other Population I objects, CO surveys show that most of the star formation occurs in molecular clouds. Surveys of the different CO transitions result in traces of molecular gas with different properties: the lower the transition (in energy), the colder the gas traced. This means that the coldest molecular gas is traced by the ground transition CO(1-0) (shorthand for CO(J=1→0)), which traces a vastly larger amount of gas than the other brighter transitions, like CO(2-1) or CO(3-2), as shown in Figure 1.8.

To date, observations of the molecular gas are mainly limited to higher rotational CO lines as they are brighter than the CO(1-0) line. As a result, observations tracing the coldest molecular gas using the CO(1-0) line are limited to a few bright and extended high redshift galaxies. With the instalment of Ka-band receivers (bandwidth of about 13.5 GHz), the CO(1-0) line can now be observed for less luminous sources, that previously only had higher CO line detections. Therefore, we are now able to get a better view on the morphology and velocity structure of the cold molecular gas in, for instance, gravitationally lensed AGN at redshift $z \sim$ 2-3.

1.5 Target: HE1104−1805

This optically bright quasar was first observed by Wisotzki et al. (1993) as two images separated by 3.19 arcsec. The quasar is observed to be radio quiet, meaning it has no significant jets, and hence its emission spectrum is dominated by the AGN. We can observe the quasar as it is strongly gravitationally lensed by a, likely elliptical, galaxy, located at a redshift of $z = 0.729$ (Lidman et al. 2000). The target quasar is located at a redshift of $z = 2.3221$ (Riechers 2011), so the CO line is expected to be redshifted to $\nu_{\rm CO} = 34.71$ GHz. HE1104−1805 was chosen as the target of this study due to a previous CO(1-0) detection, as presented by Sharon et al. (2016).

HE1104−1805 has an unusual gravitational lensing system as the lens galaxy is near the bright image rather than the faint one, see Figure 1.9. Furthermore, the measured image separation is also much larger than is typically the case, the median being 1.5 arcsec (Lehár et al. 2000). This suggests that the separation is boosted by the presence of a galaxy group or cluster, although none is obviously present

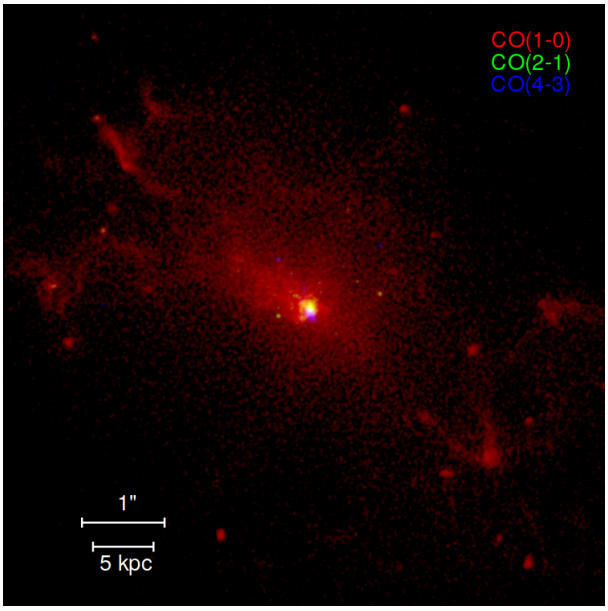

Figure 1.8: Simulation of a galaxy at redshift $z = 4$. The CO(1-0) emission is traced in red, the CO(2-1) in green and the CO(4-3) in blue. Note that the ground state transition traces much more of the molecular gas than the other two emission lines. Particularly, the extent of the cold molecular gas is ∼8 kpc as traced by CO(1-0), whereas the other transitions probe much more compact regions. Source: Casey et al. (2018).

Table 1.1: A summary of the details of VLA observations used in this thesis.

Target	ID	Date	Config.	$t_{\rm on}/t_{\rm tot}$ (hr)	$N_{\rm ant}$	Flagged (%)	Primary Calibrator	Secondary Calibrator
HE1104−1805	15B-329	2015 Dec 3	D	1.46/1.99	24	33	3C286	J1048−1909
	11B-025	2012 Apr 26	C	1.82/3.49	24	29		

from observations at optical and radio wavelengths.

The first observation of HE1104−1805 we used for this thesis has been taken by the VLA in D-configuration on the 3rd of December 2015 (ID: 15B-329, PI: Sharon). It was conducted using 27 antennas over a period of two hours. First, the flux calibrator (3C286) was shortly observed for about 8 minutes. In 15 scans the source was alternatively observed with a nearby phase reference source (J1048−1909) in scans of 5 and 1 minute, respectively. The data were taken with 16 spectral windows with a bandwidth of 128 MHz each, divided into 128 channels. The total bandwidth was 2.048 GHz in a dual-polarisation mode.

The second observation has been taken in the C-configuration on the 26th of April 2012 (ID: 11B-025, PI: Riechers). This observation was conducted over a period of two and a half hours, using 26 antennas. The source was alternatively observed in 26 scans with the same phase reference source for 225 and 50 seconds, respectively. After which, the same flux calibrator was observed for about two minutes. Again 16 spectral windows with the same bandwidth were used, but divided into 64 channels.

A summary of some details of the observations is given in Table 1.1.

1.6 This Thesis

The goal of this thesis is to characterise the velocity structure of the CO(1-0) emission in the lensed AGN host galaxy HE1104−1805. Although the velocity structure of the CO(1-0) traced gas has already been probed by Sharon et al. (2016), it has not been imaged as of yet. Additionally, using a CO(1-0) emission measurement the integrated CO luminosity is determined, from which the gas mass of HE1104−1805

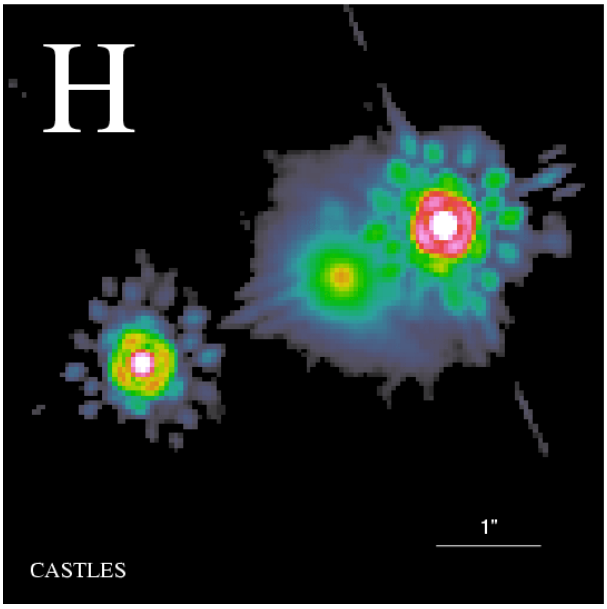

Figure 1.9: *Hubble*/NICMOS image of HE1104−1805 in the infrared H band, centred on 1.65 μm. Source: Kochanek et al. (1999).

is derived. Using a continuum emission measurement, its radio-infrared correlation factor, q_{IR}, is determined and compared to the median value for star-forming galaxies. Furthermore, HE1104−1805 is positioned against the Kennicutt-Schmidt (K-S) relation for local and high redshift objects to determine its relative star forming efficiency (SFE).

We will use observations centred around 34.634 GHz of the VLA to achieve this goal, as described in Chapter 2, together with an in-depth description of the calibration process. The analysis of the acquired data and results is presented in Chapter 3. In Chapter 4, we will discuss the results and their implications, together with a comparison to literature and models. Finally, in Chapter 5, we will conclude this thesis and suggest ideas for further research.

Throughout this thesis, we assume a standard cosmological model, with $H_0 = 67.8$ km s^{-1} Mpc^{-1}, $\Omega_M = 0.308$ and $\Omega_\Lambda = 0.692$, as determined by Planck Collaboration et al. (2016). Spectral luminosities are given in source rest-frame frequencies, flux densities are given in observed frequencies.

Chapter 2

Observations

2.1 Karl G. Janksy Very Large Array (VLA)

The Very Large Array (VLA) (see Figure 2.1) was built in 1973 and consists of 27 antennas, plus one spare. Each antenna has 8 different receivers, covering frequencies between 74 MHz and 50 GHz, and a 25 m radio dish. This gives the VLA a total collecting area of about 13250 m^2. The array is located in New Mexico, USA, at an elevation of 2124 m above sea level. The VLA is part of the National Radio Astronomy Observatory (NRAO), based in the USA. This array is designed to allow observations of a large range of astronomical objects, from pulsars to cosmologically distant galaxies.

All of the antennas are mounted on railroad tracks in a 'Y' shape (see Figure 2.2), such that they can be set up in different configurations with varying radii and densities. There are four antenna configurations, named A (the largest) through D (the most compact). The type of configuration sets the angular resolution of the observation. In this thesis we make use of C and D-configuration observations. The D-configuration has a maximum baseline of 1.03 km, a minimum baseline of 35 m and a half-power synthesized beamwidth for the Ka-band (∼33 GHz) of about 2.1 arcsec. The C-configuration has a maximum baseline of 3.4 km, a minimum baseline of 45 m and a half-power synthesized beamwidth for the Ka-band of about 0.63 arcsec. The antenna locations in both configurations are shown in Figure 2.2.

2.2 Data Reduction and Calibration

All measurement sets have been calibrated using the Common Astronomy Software Applications (`CASA`, version 5.5.0). In this section, we describe the main steps of the calibration process.

As stated in Section 1.1, every visibility consists of an amplitude and a phase. The goal of the calibration process is to scale the measurements to meaningful units and to correct them for atmospheric

Figure 2.1: A photograph taken at the VLA site (Source: NRAO)

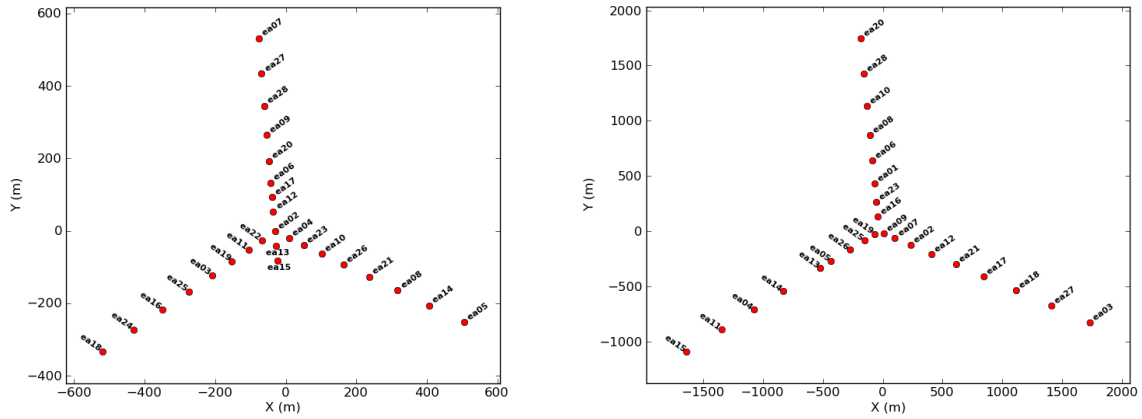

Figure 2.2: Left: The VLA antenna positions in the D-configuration. **Right:** The VLA antenna positions in the C-configuration. Note the different distance scales.

Table 2.1: Summary of the selected data from the observations. The fields are given in order of: primary calibrator, secondary calibrator and target.

Config.	Fields	Spectral Windows	$\nu_{\rm centre}$ (GHz)	$N_{\rm chan}$	$\Delta\nu_{\rm chan}$ (MHz)	$\Delta\nu_{\rm tot}$ (MHz)	Correlations
D	0, 1, 2	8∼15	34.634	128	1	1024	LL, RR
C	5, 2, 3	8∼15	34.634	64	2	1024	LL, RR

and instrumental effects. The used observations include two types of calibrators, a primary (or flux density) calibrator and a secondary (or phase) calibrator. The primary calibrator is used to scale the measured flux densities to meaningful units, commonly chosen to be a bright and stable in time source for which flux models are well known. The secondary calibrator is used to calibrate the amplitudes and phases as function of time. This calibrator has to be a reasonably bright object, commonly a point-like source, close in projection to the scientific target.

We calibrate the observations using a customised script that includes the steps as described in the next sections.

2.2.1 Inspection of the Observation

After downloading the full measurement sets from the NRAO database, a text file is created that contains information about the set-up of the observation: the scan strategy, the different fields/objects, the spectral windows used, etc. From this file, we determine the fields and spectral windows of interest. Only the fields of the primary calibrator, the secondary calibrator and the target are selected. Furthermore, only the spectral window(s) containing the CO line and some around it (for continuum subtraction) are selected. The original data set is split this way to reduce data size and increase processing speed. Details of the inspection are presented in Table 2.1.

2.2.2 A Priori Calibration

The atmospheric opacity affects the flux density scale if any of the calibrators and target are observed at different elevations, which is generally always the case. The effect of the atmospheric opacity is especially important at high frequency observations (e.g. Ka-band, 26.5-40 GHz) and should be corrected for. From seasonal models and weather station measurements, the exact opacities per spectral window are computed, after which the measured flux densities can be corrected as a function of elevation. The corrections are not yet applied to the data, but written to a calibration table, which is used in other calibration steps.

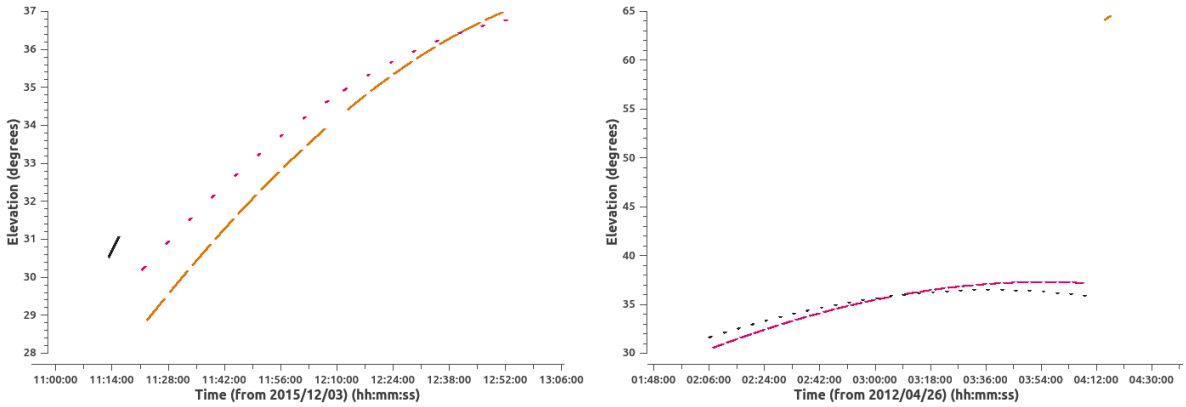

Figure 2.3: Left: The (unflagged) antenna elevation as a function of time for the used D-configuration observation. The primary calibrator is shown in black, the secondary calibrator in red and the target in orange. **Right**: The (unflagged) antenna elevation as a function of time for the used C-configuration observation. The primary calibrator is shown in orange, the secondary calibrator in black and the target in red.

All configurations of the VLA have a standard set-up resulting in specific baselines. However, during the observation, some antennas can be slightly offset, resulting in different baselines. To account for this, a separate calibration table is created which is used in other calibration steps. This step is important as the exact baselines affect the delays between the antennas.

The gaincurves describe how the antenna responses behave as a function of elevation. Furthermore, every antenna has a slightly different efficiency, which should be accounted for as well. A separate calibration table is created for use in further calibration steps.

2.2.3 Flagging

There are a multitude of sources that can cause bad data during the observations. Some of these are systematic and/or easy to filter out using existing algorithms, others have to be manually removed. Firstly, all zero amplitude data is flagged as these are caused by (temporary) errors in the receiver or correlator. Note that due to systemic noise, a pure zero is never actually observed.

Secondly, depending on the target sources, the antennas could point relatively low on the sky such that other antennas might interfere with the measurements, especially when using the more compact VLA configurations, like the D-configuration. Generally, the effects due to shadowing are small or even completely neglected if the antennas do not observe below 40 degrees elevation. The elevation during the full observations is shown in Figure 2.3.

Moreover, during the first few to tens of seconds of every scan the antennas could not yet be on source. This is due to the antenna still moving or leftover vibrations in the antennas after moving. Therefore, after major movement of the antennas (e.g. target switching) the first few to tens of seconds are flagged.

Additional flagging is manually done to filter out bad antennas, scans (time ranges), spectral windows, channels and Radio Frequency Interference (RFI). This is done after the first full calibration run of the data, as we expect the calibrated data of the calibrators to match our expectations. Any outliers or unexpected structure might be caused by bad data. Two examples of bad data are shown in Figures 2.4 and 2.5. Additionally, some antennas are removed on the basis of publicly available observer logs made during the observations, stating any possible problems with the antennas that occurred during the observations. After the manual flagging, the full calibration process is ran again to exclude the bad data from the beginning of the calibration. The effect and importance of the manual flagging are illustrated in Figure 2.10.

For both observations additional manual flagging was required. For the D-configuration observation the following bad data were flagged. Two antennas, 13/ea15 and 23/ea25, were flagged as they produced consistent outliers in both amplitude and phase and were hence labelled as bad antennas. One scan showed a scattered phase plot for the flux calibrator and was flagged completely in all fields. Aside from

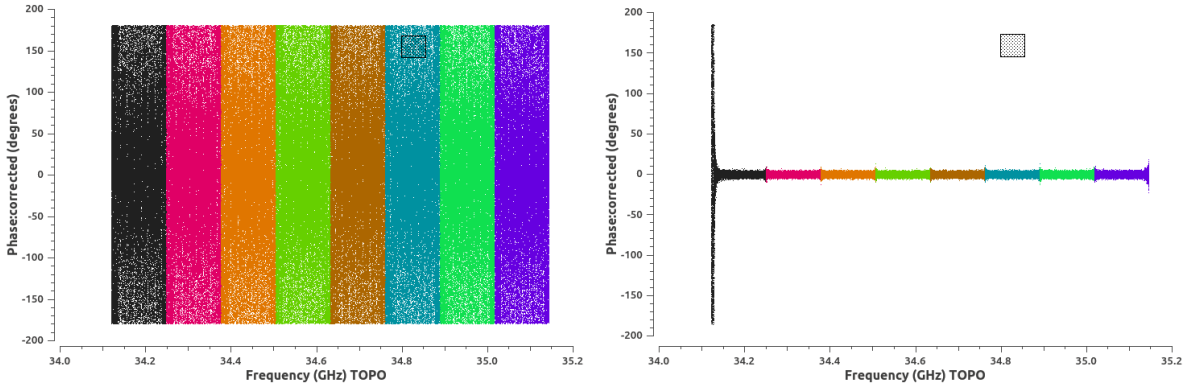

Figure 2.4: Example of bad phase data. The phase as a function of frequency for the primary calibrator (shown colourised by spectral window) is ideally flat, but the left plot shows a significant scatter. All visibilities in the plotted box belong to scan 1, indicating it might be a bad scan. Indeed, leaving out scan 1 yields the right plot. Here the average phase scatter is about ±5 degrees. Note that the initial few channels still show scattering and should be flagged as well. Additionally, the transitions between the spectral windows tend to be slightly noisy.

Table 2.2: Summary of the manual flagging applied to the used observations. If flags are only applied to a selection of antennas, these are given between parentheses. In the 'Spectral Windows' column, the numbers behind the colon (':') indicate the flagged channels of the corresponding spectral windows.

Config.	Antennas (Obs. Logs)	Antennas (Bad Data)	Fields	Spectral Windows	Scans	Time Ranges
D	-	13/ea15 23/ea25	-	0:0∼40 7:100∼127	1	-
C	3/ea04	-	0 (22/ea25) 1 (22/ea25)	4 (2/ea03) 0:0∼8 7:60∼63	63 (8/ea09)	02:04:36.0∼02:05:15.0 (14/ea15, 16/ea17) 03:10:57.0∼03:11:40.0 (16/ea17, 24/ea27)

the standard noise in the channels near the edges of spectral windows, the first ∼40 and last ∼28 channels of the measurement set showed extreme phases and were flagged. For the C-configuration observation the following bad data were flagged. The observer log stated that antenna 3/ea04 has lost data due to Ka-band receiver maintenance. Indeed an inspection of the data set resulted in the flagging of this antenna. Furthermore, antenna 2/ea03 recorded bad data in spectral window 4, antenna 22/ea25 in fields 0 (secondary calibrator) and 1 (target), antenna 8/ea09 in scan 63 and antennas 14/ea15, 16/ea17, and 24/ea27 each in a specific time range. Finally, the initial 8 and final 4 channels showed extreme phases and were flagged. A summary of the manual flagging is given in Table 2.2.

Considering both the automatic and manual flagging, it is not uncommon to flag large parts ($> 25\%$) of the obtained measurements. For the D-configuration observation a total of 33% of the visibilities were flagged and 29% for the C-configuration observation. A summary of the manually flagged data is presented in Table 2.2.

2.2.4 Setting the Flux Density Scale

The flux density scale of an observation is set using pre-determined models for the primary calibrator. These models account for the shape of the calibrator and they consist of empirical polynomial expressions for the spectral flux density as a function of frequency. These expressions are used in combination with the measurements of the primary calibrator to calibrate the flux density scale for the secondary calibrator. Using this scale, the measured signals can be converted to a common unit, which is Jansky. For both the used observations the flux density scale was set using the primary calibrator (3C286), with a flux density model derived by Perley & Butler (2013),

$$\log S_\nu = 1.25 - 0.46 \log \nu_9 - 0.17 \left(\log \nu_9\right)^2 + 0.03 \left(\log \nu_9\right)^3), \tag{2.1}$$

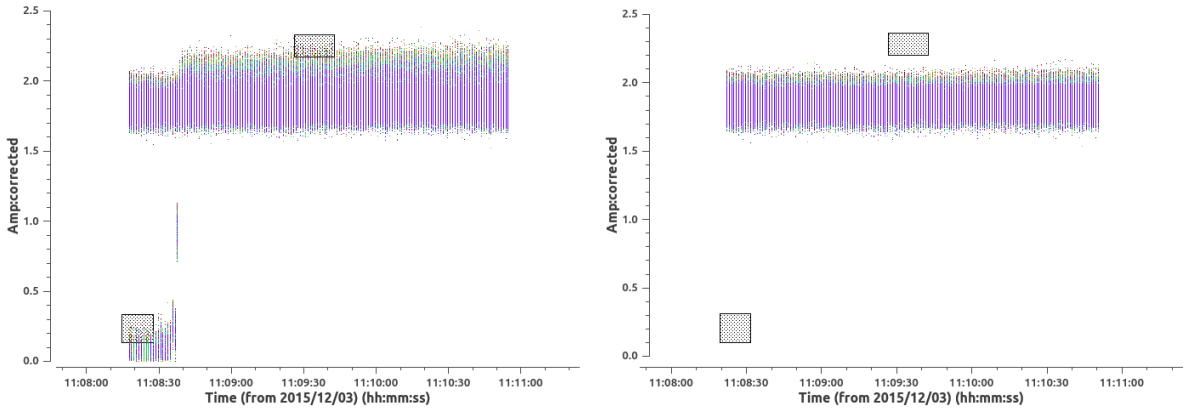

Figure 2.5: Example of bad amplitude data. The amplitude as a function of time for the primary calibrator (shown colourised by spectral window) is ideally flat, but the left plot shows some unexpected structure. All visibilities in both plotted boxes belong to a baseline with antenna 13/ea15, indicating it might be a bad antenna. Indeed, leaving out antenna 13/ea15 yields the right plot. Here, the amplitude shows nearly no trend over time and the amplitude spread is about 10% with respect to the mean value.

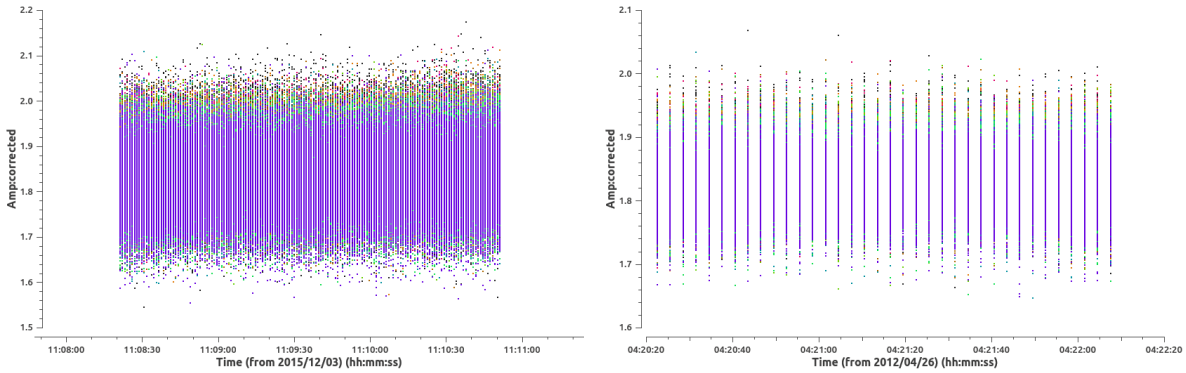

Figure 2.6: The flagged and calibrated amplitude as a function of time of the primary calibrator of the D-configuration data (left) and C-configuration data (right). For the D-configuration the mean amplitude is about 1.85 Jy with an amplitude spread of 10%. For the C-configuration the mean amplitude is about 1.85 Jy with an amplitude spread of 8%.

where S_ν is the spectral flux density in Jy and ν_9 the observing frequency in GHz.

2.2.5 Bandpass and Delay Calibration

Now that we have our measurements in useable units, we still need to calibrate the observed visibilities, $V_{\text{obs}}(t, \nu)$, to retrieve the true visibilities, $V(t, \nu)$. The relation between the two, as a function of time and frequency, can be given as

$$V_{\text{obs}}(t, \nu) = V(t, \nu)G(t)B(t, \nu), \tag{2.2}$$

where $G(t)$ is the complex time-dependent gain and $B(t, \nu)$ the complex frequency-dependent gain, often called the "bandpass". Note that the bandpass is generally either constant over the length of an observation or has a slow time dependence. Bandpass calibration is the process of measuring and correcting the frequency-dependent part of the complex gains that relate the measured visibilities with the true visibilities.

Using the known models for the primary calibrator, the antenna-based delays (phase as a function of frequency) are solved to determine the bandpass solution. Primary calibrators are generally chosen to have flat and featureless spectra, such that we are able to calibrate with great precision. However,

patches of air with different water vapour content (and hence index of refraction) affect the incoming wave front differently as a function of frequency. This causes phase fluctuations which result in: a loss of sensitivity due to low coherence, radio seeing (about 1 arcsec at 1 mm observations), pointing offsets and delay offsets. The delays are solved by fitting the measured phases as a function of frequency. Note that only the central channels (<50%) are used to determine the bandpass solution, as the outer channels of a spectral window are considerably more noisy.

Finally, to check whether this calibration step was successful, we can inspect the phases and amplitudes as a function of frequency. We expect these to be (nearly) flat for our used primary calibrator. A comparison between before and after the bandpass calibration is given in Figure 2.7. For the calibration to be successful, the primary calibrator should have a high signal-to-noise ratio, particularly important if one is trying to observe weak spectral lines, like in the case of this thesis.

2.2.6 Complex Gain (Phase and Amplitude) Calibration

In this step, the primary calibrator, now calibrated as a function of frequency, is used to derive a solution for the time-dependent gain, $G(t)$, as given in Eq. 2.2.

After this calibration step a new model for the secondary calibrator is made with the correct flux density and broad-band spectrum. This improved model is then used to acquire the antenna complex gains as a function of time and frequency. After which, additional manual flagging is done and the calibration process is done again up to this step. This is repeated until the calibrated residual visibilities no longer show major outliers. Finally, if the calibrated measurement set looks satisfactory, the calibration solutions are applied to each calibrator and then the target source by interpolating the solutions of the corresponding secondary calibrator. For this interpolation to be accurate, this calibrator has to be close to the target and must be observed frequently. The interpolation provides a model of atmospheric phase and amplitude change along the line of sight to the science target as a function of time, such that the data can be corrected. This procedure is called "phase referencing". We use a minimum signal-to-noise ratio of 2 for determining these solutions as it is a good compromise of using the best available data without rejecting too many solutions. A comparison between before and after the complex gain calibration is given in Figure 2.7.

In the end, each calibrator is calibrated with its own calibration tables, whereas the target gets the calibration from the secondary calibration. This is done as the interpolation in time will be more accurate than extrapolating the primary calibrator (see Fig. 2.3), even though the latter has a higher signal-to-noise ratio.

2.2.7 Imaging of the Continuum

The background continuum emission can be imaged using multi-frequency synthesis imaging, in which measurements at several observing frequencies are combined into a single image. By excluding the spectral windows containing the CO line and edge channels (to reduce noise) the result is an image of the continuum emission. This image, however, is not a true representation of the source and is what we call a "dirty" image. The measured flux densities in the dirty image are related to the true flux densities as

$$I_{\rm meas} = B_{\rm dirty} \times (B_{\rm prim} \times I_{\rm src}) + N_1, \tag{2.3}$$

where $B_{\rm dirty}$ is the dirty beam, $B_{\rm prim}$ the primary beam and N_1 the noise of the measurements. To be able to reconstruct the true flux densities we need to deconvolve the dirty image for the dirty beam and the primary beam. The noise is a leftover from the calibration process and has already been minimised to the best of our ability.

We can account for the dirty beam by "cleaning" the image. Cleaning removes the dirty beam (or Point Source Function (PSF), see Fig. 2.9), which is responsible for the side lobe structure. This has two main advantages: it removes the side lobe flux from the dirty image such that only the true source flux and noise are left and it lowers the overall image noise such that a higher signal-to-noise detection can potentially be made. The effects of the cleaning process depend greatly on how the cleaning is implemented. The basis of the process is the Högbom algorithm (Högbom 1974), which is described as follows:

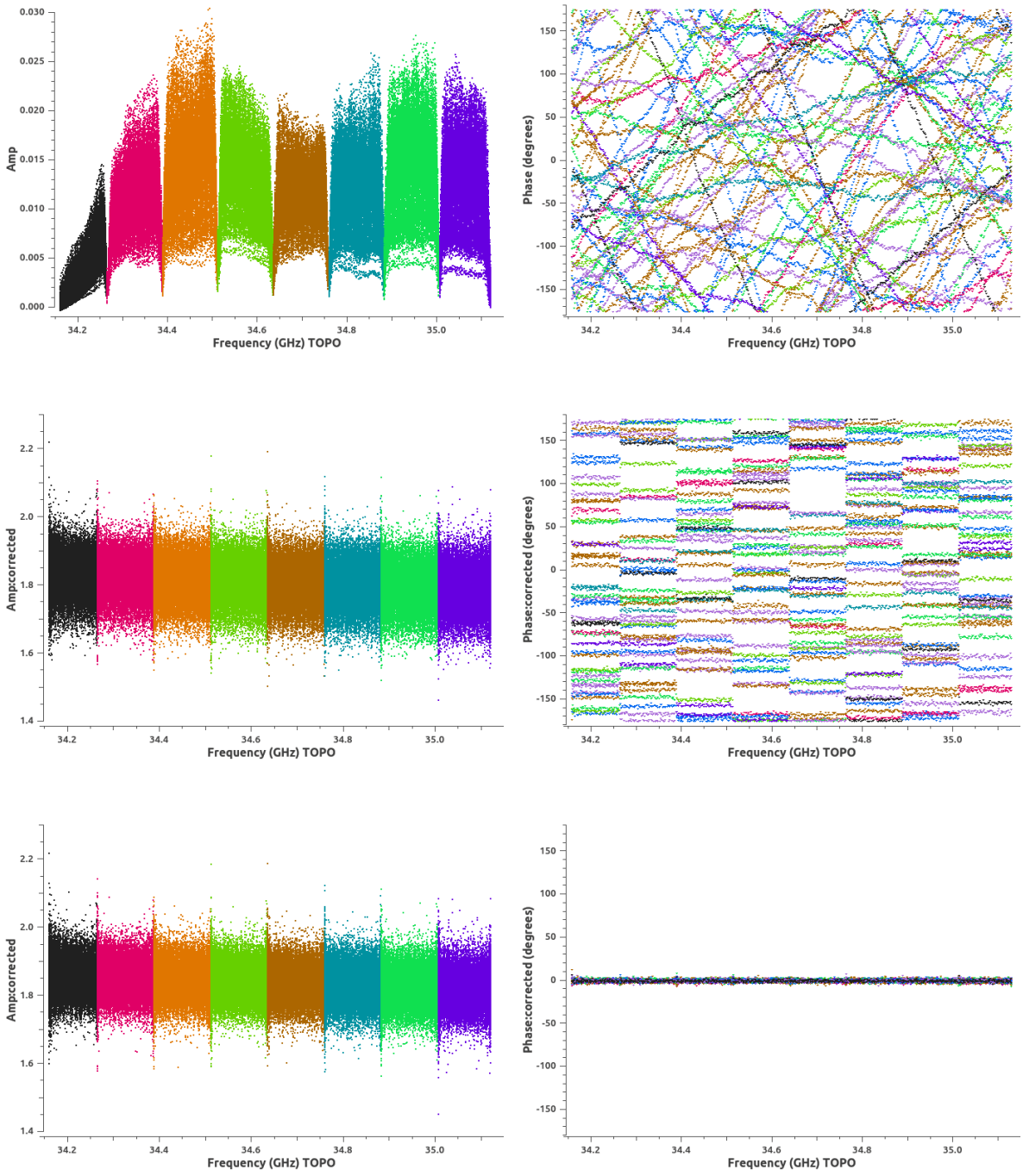

Figure 2.7: Left: Amplitude as a function of frequency of the primary calibrator in the flagged C-configuration observation before calibration (top), after flux scale and bandpass calibration (centre) and after complex gain calibration (bottom). Note the slight frequency dependence of the primary calibrator. Data colourised by spectral window. **Right**: Phase as a function of frequency in the primary calibrator field during the flagged C-configuration observation before calibration (top), after flux scale and bandpass calibration (centre) and after complex gain calibration (bottom). Only the phases of baselines containing the reference antenna (18/ea19) are shown. Note that after the calibration process the phases are constant zero over the frequency range (with a spread of about five degrees), as we expect from the primary calibrator. Data colourised by baseline.

1. Find the position and intensity of the peak value in the dirty image. The search for peaks can be constrained to specified areas of the image.

2. Subtract from the dirty image, at the position of the peak, the dirty beam, B_{dirty}, multiplied by the peak intensity and a loop gain ($G_{\text{loop}} \leq 1$, in our case we use $G_{\text{loop}} = 0.1$). The subtracted image is called a clean component and is stored in a point source model image.

3. Go back to (1), unless the remaining peak in the dirty image is below a user specified threshold, usually set to a multiple of the off-source Root Mean Square (RMS) value. Here the RMS is a quantitative indication for the noise of an image and is computed using

$$\sigma_{\text{RMS}} = \sqrt{\sum I_i^2/n}, \tag{2.4}$$

   where I_i is the intensity of a single pixel, summed over an off-source region of the image, and n the number of pixels in said region.

4. Construct a "clean beam" by fitting an elliptical Gaussian to the central lobe of the dirty beam. Convolve the constructed point source model with the clean beam to construct a clean image.

5. Finally, add the residual dirty image to the clean image.

After the cleaning process, we are left with

$$I_{\text{clean}} = B_{\text{prim}} \times I_{\text{src}} + N_2, \tag{2.5}$$

where N_2 is the noise, affected by the cleaning process. Next, a primary beam correction can be applied by dividing the pixel values of the created maps by the beam flux image (see Fig. 2.8). The primary beam correction mostly affects the measurements of the integrated and peak surface brightness. However, we do not apply a primary beam correction as its effects over the spatial sizes of the (3σ detection) images are negligible, especially compared to the 10% flux density uncertainty, see Figure 2.8. Measured from the pointing centre, the beam flux reaches 99% at 4.5 arcsec, 95% at 10.3 arcsec and 90% at 14.8 arcsec. The clean C&D-configuration line image extends to a distance of 6.5 arcsec from the centre of the primary beam, at 98%. Therefore we can say that the clean image (Eq. 2.5) represents the true flux densities (with noise) as

$$I_{\text{clean}} \approx I_{\text{src}} + N_2. \tag{2.6}$$

The pixel size of the images is determined using the Nyquist sampling criterion. In radio imaging, this commonly entails that the smallest structure is sampled over at least 3 pixels, although we will use 5. From this, the following constraint is set

$$\text{cell size} < \frac{0.2}{B_{\lambda,\text{max}}} \text{ rad}, \tag{2.7}$$

where $B_{\lambda,\text{max}}$ is the maximum baseline in units of the observing wavelength. Note that this might differ from the standard B_{max} of the used configuration due to the potential flagging of outer antennas.

During imaging, the measured visibilities can be weighted in different ways to affect the angular resolution and the sensitivity to certain spatial structure sizes. For this thesis, the imaging is done using three different weightings: natural, Briggs (with *'robust=0'*) and tapered. The natural weighting maximises the point source sensitivity of the image whilst keeping the RMS low. Natural weighting gives equal weight to all samples, but as the inner uv-plane has a higher density of samples it 'naturally' favours short baselines (large spatial scales), which degrades the angular resolution. Briggs weighting gives more weight to the longer baselines (small spatial scales) to gain a higher angular resolution. This degrades the point source sensitivity and increases the RMS, but suppresses any side lobe structure in the image, as most of the side lobe structure is now resolved out. A Gaussian taper can be applied while imaging to smooth the image plane. It favours shorter baselines and, like natural weighting, degrades angular resolution. However, it also degrades point source sensitivity, like Briggs weighting does. This has the advantage of improving sensitivity to any extended structure, which might otherwise be resolved

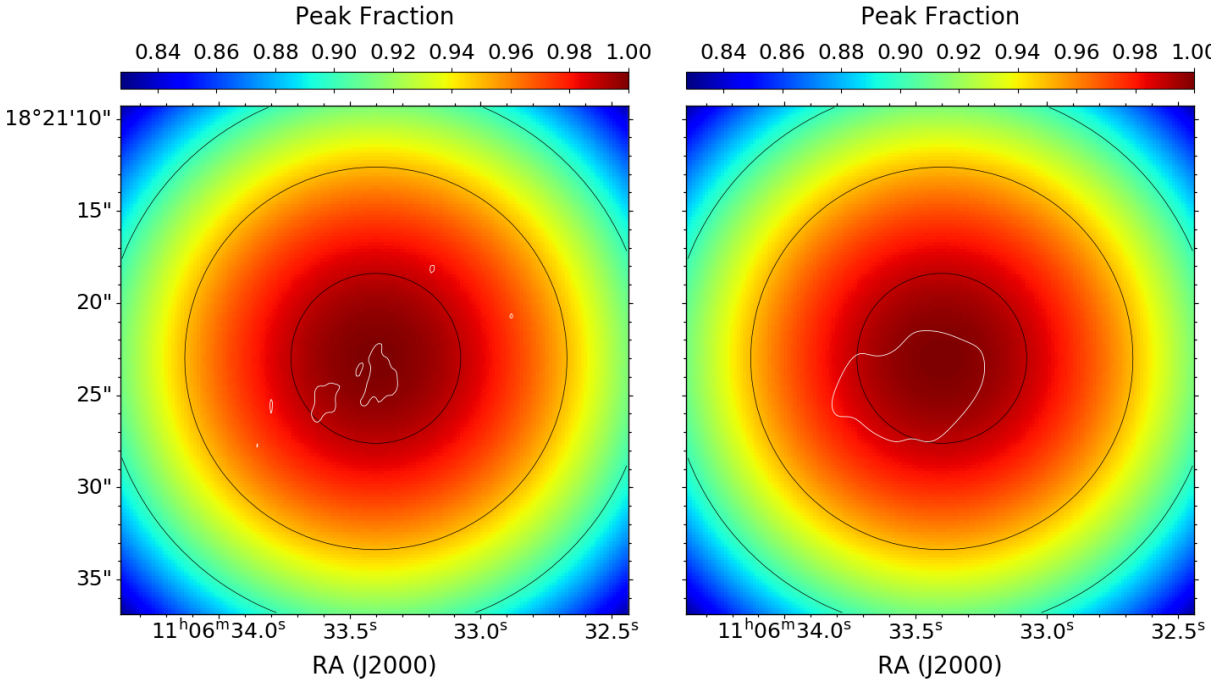

Figure 2.8: The primary beam of the C&D-configuration observation overlaid with the 3σ contours in white of the natural weighted moment 0 map (left) and the $2''$ tapered moment 0 map (right). The black contours are at 99%, 95% and 90% of the central primary beam value, which is set to unity. Note that the 3σ regions are well contained within 98% of the central value, making a primary beam correction insignificant.

out. The size of the applied Gaussian taper depends on the beam sizes of the other weightings, as it should be larger to be useful.

The PSF (or dirty beam) of each weighting is shown in Figure 2.9. The PSF is important during deconvolution of the image and substitutes a large part of the noise in an image. Note that the PSF is determined by the uv-plane coverage of the observation and hence the shape of the uv-plane (see Figure 1.1) can be recognised in the PSFs.

Throughout this thesis, only the clean images and data are presented. Although the dirty images and data are also represented only for the D-configuration, to illustrate the effects of our cleaning process.

2.2.8 Subtraction of the Continuum

If a source has continuum background emission, we subtract this from the data, as it would otherwise contaminate the line emission we are looking for. We fit the continuum emission as a function of frequency using a first order polynomial. For small bandwidths in the radio frequency, a first order fit order is an acceptable approximation to the synchrotron continuum emission. Large bandwidths can contain emission more complex than a first order polynomial. Therefore, for large bandwidths, it is common to determine the continuum separately for different segments of the total bandwidth. In this thesis, the observation bandwidths are sufficiently small to use a single continuum fit. For the fit we exclude the spectral windows containing the line emission and the edge channels, as they are noisier than the central ones.

2.2.9 Imaging of the CO(1-0) Line

For the imaging of the CO(1-0) line we transfer the measured flux densities into a data cube. These cubes are built using two positional axis (in our case: Right Ascension (RA) and Declination (DEC), both in the J2000 system) and a third axis. The third axis can either be the observing frequency or radio velocity with respect to a reference frequency, according to Eq. 2.12. From the created cubes, we make

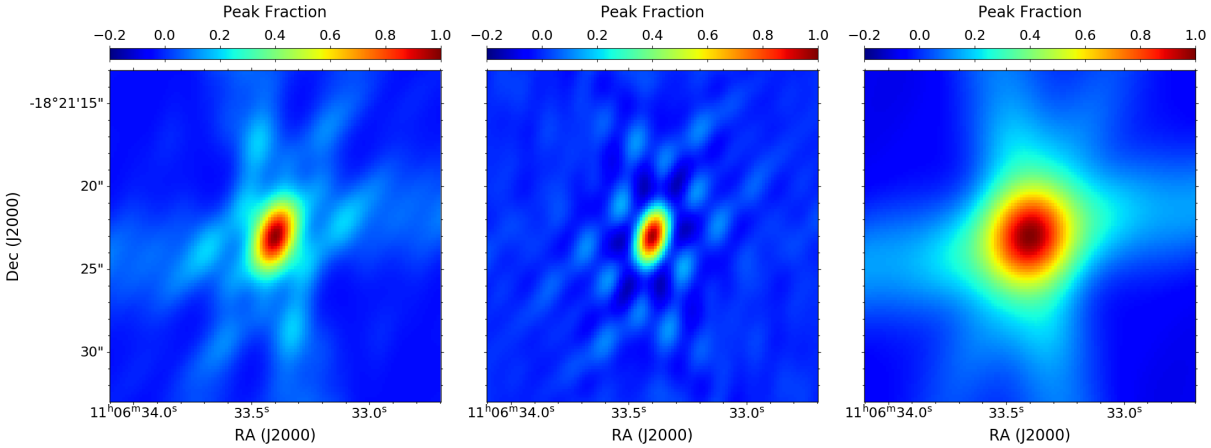

Figure 2.9: The PSF (or dirty beam) of the three different weightings used: natural (left), Briggs (*'robust=0'*) (centre) and (4″) Gaussian tapered. Compared to the natural weighting, Briggs is used to increase spatial resolution in the image, but at the cost of increased noise structure and a Gaussian taper is used to recover as much of the resolved-out flux as possible and to increase sensitivity to extended structures, but at the cost of decreased spatial resolution. These PSFs are used to construct all maps.

a spectral profile (flux density versus radio velocity) only using the data from within a $3\sigma_{\rm cube}$ detection region, where $\sigma_{\rm cube}$ is the average RMS of the channel maps. The spectral profiles are exported and analysed using `Python`.

Finally, we create several moment maps, only using the channels within the cube that contain the line structure. These moment maps are created by collapsing the velocity (or frequency) axis of the cube in several different ways. For this thesis zeroth, first and second moment maps are created. A zeroth moment map presents the integrated value of the cube along its velocity axis, where the value of a given pixel in the map can be calculated as

$$M_0 = \Delta v \sum I_i, \tag{2.8}$$

where Δv is the total velocity bandwidth of the selected channels and I_i the intensity of the i-th pixel along the velocity axis. A first moment map presents the intensity weighted velocity field, where the value of a pixel is given as

$$M_1 = \frac{\sum(I_i v_i)}{M_0}, \tag{2.9}$$

where v_i is the velocity of the i-th pixel along the velocity axis and M_0 the value of the same pixel in the zeroth moment map. A second moment map presents the intensity weighted velocity dispersion field, where the value of a pixel is given as

$$M_2 = \sqrt{\frac{\sum(I_i\,(v_i - M_1)^2)}{M_0}}, \tag{2.10}$$

where M_1 is the value of the same pixel in the first moment map.

In this thesis, we make use of the CO(1-0) transition, with a rest-frame frequency of $\nu_0 = 115.271$ GHz. However, due to cosmological distances to the observed object, the CO line is redshifted to a lower frequency. The observed frequency, $\nu_{\rm obs}$, of any line as function of its rest-frame frequency, ν_0, and redshift of the emission region, z, can be determined as

$$\nu_{\rm obs} = \frac{\nu_0}{z+1}. \tag{2.11}$$

If the gas is moving along our line of sight, the CO emission line might be shifted additionally due to the Doppler effect. Complex velocity structures, like rotating disks, inflow/outflow or jets, can cause the appearance of additional structure in the emission spectrum. For instance, the emission line from

a gas moving towards us will be shifted to higher frequencies and a gas moving away from us will have its emission line shifted to lower frequencies. In the case of a rotating disk, this causes a doubly peaked CO(1-0) emission line as we have both a gas component moving towards us as well as away from us, given the inclination of the rotating disk allows us to observe it. The radio velocity of the gas along line of sight can be determined using

$$v_{\rm radio} = c\left(1 - \frac{\nu_{\rm obs}}{\nu_0}\right). \tag{2.12}$$

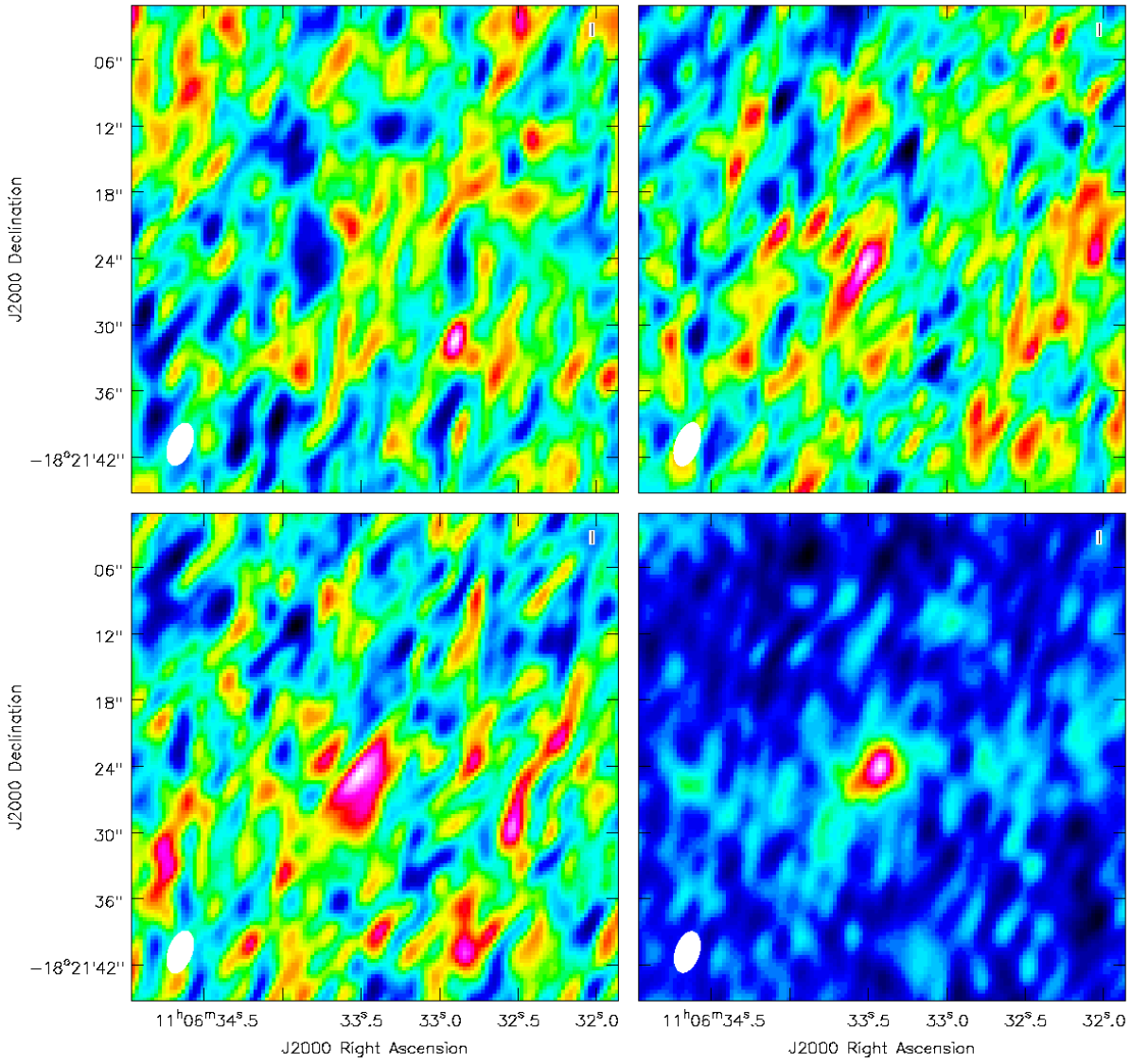

Figure 2.10: These images show the effect of the flagging and calibration process on the outcome of the final imaging. Note that the image becomes recognisable only after all flagging and calibration steps are implemented. Beam sizes are shown at the lower left. **Top left**: imaged using unflagged and uncalibrated data. **Top right**: imaged using unflagged, but calibrated data. **Bottom left**: imaged using flagged and calibrated data, but without additional manual flagging. **Bottom right**: imaged using flagged (including manual flagging) and calibrated data.

Chapter 3

Results

3.1 D-Configuration

3.1.1 Continuum Emission

Continuum maps for all three weightings are shown on the right in Figure 3.1. The restoring beam sizes and position angles of all images are given in Table 3.1. All continuum maps were suitable for cleaning and the clean continuum maps are shown on the right in Figure 3.2. All weightings result in prominent background continuum emission, but only the dirty Briggs weighted map shows the two images spatially resolved, with a separation of $\Delta\theta_{34.7\mathrm{GHz}} = 3.0 \pm 0.3$ arcsec.

The clean natural weighted continuum map yields an integrated flux density of $S_{34.7\mathrm{GHz}} = 92 \pm 10$ μJy, with a single 7.1σ peak surface brightness of $I^{\mathrm{max}}_{34.7\mathrm{GHz}} = 107 \pm 11$ μJy/beam. The Briggs weighted map yields an integrated flux density of $S_{34.7\mathrm{GHz}} = 52 \pm 6$ μJy, which is considerably lower than the natural weighted data. Two continuum peaks (4.7σ and 3.3σ) are spatially resolved with peak surface brightnesses of $I^{\mathrm{max,A}}_{34.7\mathrm{GHz}} = 98 \pm 10$ μJy/beam and $I^{\mathrm{max,B}}_{34.7\mathrm{GHz}} = 70 \pm 7$ μJy/beam, yielding a peak surface brightness ratio of 1.4 ± 0.2. Finally, the $4''$ tapered map yields an integrated flux density of $S_{34.7\mathrm{GHz}} = 98 \pm 10$ μJy, with a single 7.6σ peak surface brightness of $I^{\mathrm{max}}_{34.7\mathrm{GHz}} = 136 \pm 14$ μJy/beam, both slightly higher than the natural weighted data.

3.1.2 CO(1-0) Emission

The dirty moment 0 maps are shown on the left in Figure 3.1. The Briggs weighted moment 0 map shows two fully resolved images of the source quasar, whereas the natural weighted map does show two separate peaks, but not fully resolved. The Gaussian taper weighted map shows only a single peak and so any structure is lost.

Channel maps ($\sim$17.3 km s^{-1} width) selected from the clean natural weighted cube are shown in Figure 3.3. These maps clearly show the presence of the emission line. All other channels contain no significant structure, like the top left channel map of Figure 3.3. In order to clean the data cubes, significant line structure needs to be visible in the channel maps. If a data cube cannot be cleaned, no clean moment 0 map or clean spectral fit can be made. For the D-configuration this is only possible with the natural weighted and $4''$ tapered cubes, as the Briggs weighted channel maps do not show any structure with a sufficiently high signal-to-noise ratio. The resulting cleaned moment 0 maps are shown on the left in Figure 3.2. Note the tightening of the contours and general increase of the signal-to-noise ratio of the image, i.e. number of contours, with respect to the dirty maps. Furthermore, the resulting flux densities of the cleaned maps is lower than the dirty maps, as any contribution of the side-lobes is removed by the cleaning process.

The clean natural moment 0 map yields an integrated flux density of $S_{1-0}\Delta\nu = 0.36 \pm 0.04$ Jy km s^{-1} within a $3\sigma_{\mathrm{RMS}}$ region. In this moment 0 map the two images (10.0σ and 7.9σ) are only partially spatially resolved and separated by $\Delta\theta_{1-0} = 3.0 \pm 0.4$ arcsec. This is consistent with the reported value of $\Delta\theta = 3.19 \pm 0.03$ arcsec by Kochanek et al. (1999) from optical wavelength observations. The brightest

Table 3.1: A summary of the restoring beam sizes and position angle of all moment 0 maps and continuum maps (listed in parentheses if different from the corresponding moment 0 map). The Gaussian taper has a size of 4, 2 and 2 arcsec for the D, C and C&D-configurations, respectively. A hyphen (-) indicates a map not presented in this thesis.

Config.	Type	Natural	Briggs ('robust=0')	Gaussian Taper
D	Dirty	3.81″, 2.10″, -17.91°	2.86″, 1.43″, -15.25°	5.70″, 4.81″, -16.89°
			(2.85″, 1.43″, -15.42°)	(5.67″, 4.80″, -17.17°)
	Clean	3.80″, 2.11″, -17.75°	-	5.70″, 4.82″, -17.02°
		(3.82″, 2.16″, -17.94°)	(2.81″, 1.41″, -14.97°)	(5.67″, 4.81″, -17.31°)
C	Dirty	1.07″, 0.63″, -8.28°	-	2.38″, 2.22″, -8.91°
		(1.09″, 0.64″, -8.30°)	-	(2.37″, 2.21″, -9.10°)
	Clean	-	-	-
		(1.09″, 0.64″, -8.36°)	-	-
C&D	Dirty	1.45″, 0.87″, -8.97°	-	3.34″, 2.65″, -15.28°
		(1.43″, 0.86″, -8.92°)	(0.88″, 0.47″, -8.98°)	(3.31″, 2.64″, -15.23°)
	Clean	1.64″, 1.20″, -12.02°	-	3.39″, 2.69″, -16.33°
		(1.56″, 1.12″, -6.72°)	(1.07″, 0.85″, -2.84°)	(3.41″, 2.70″, -15.00°)

Table 3.2: Summary of measurements from the **dirty** velocity integrated line and continuum maps (all three weightings) of **all configurations**. Integration quantities are measured within $3\sigma_{\rm RMS}$ regions, where σ_{1-0} and $\sigma_{34.7GHz}$ are the used RMS values. If multiple images are resolved, peak surface brightnesses for the fainter images are given in parentheses. A hyphen (-) indicates the quantity was not retrievable from the data and an asterisk (*) indicates repeating units. The uncertainty in surface brightness and flux density are are set to 10%, as derived from the amplitude spread.

Config.	Weighting	$\Delta\theta_{1-0}$ (arcsec)	$S_{1-0}\Delta v$ (Jy km s^{-1})	$I^{\rm max}_{1-0}$ (Jy/beam km s^{-1})	σ_{1-0} (mJy/beam km s^{-1})	$\Delta\theta_{34.7\rm GHz}$ (arcsec)	$S_{34.7GHz}$ (μJy)	$I^{\rm max}_{34.7\rm GHz}$ (μJy/beam)	$\sigma_{34.7\rm GHz}$ (μJy/beam)
D	Natural	3.2 ± 0.4	0.47 ± 0.05	0.28 ± 0.03 (0.21 ± 0.03)	38 ± 2	-	126 ± 13	111 ± 12	15 ± 2
	Briggs	3.4 ± 0.2	0.19 ± 0.02	0.24 ± 0.03 (0.18 ± 0.02)	41 ± 3	3.0 ± 0.3	40 ± 5	93 ± 10 (60 ± 7)	19 ± 2
	4″ Taper	-	0.41 ± 0.05	0.38 ± 0.04	58 ± 7	-	117 ± 12	142 ± 15	19 ± 4
C	Natural	-	-	-	27 ± 3	2.5 ± 0.2	76 ± 8	105 ± 11 (62 ± 7)	18 ± 2
	2″ Taper	-	0.15 ± 0.02	0.18 ± 0.02	48 ± 5	2.6 ± 0.3	53 ± 6	125 ± 13 (84 ± 9)	28 ± 4
C&D	Natural	3.4 ± 0.4	1.3 ± 0.2	0.17 ± 0.02 (0.16 ± 0.02)	22 ± 2	2.5 ± 0.4	301 ± 31	100 ± 10 (68 ± 7)	13 ± 2
	Briggs	-	-	-	-	-	29 ± 3	82 ± 9 (56 ± 6)	20 ± 2
	2″ Taper	-	0.57 ± 0.06	0.26 ± 0.03	32 ± 3	-	151 ± 16	46± 5	16 ±2

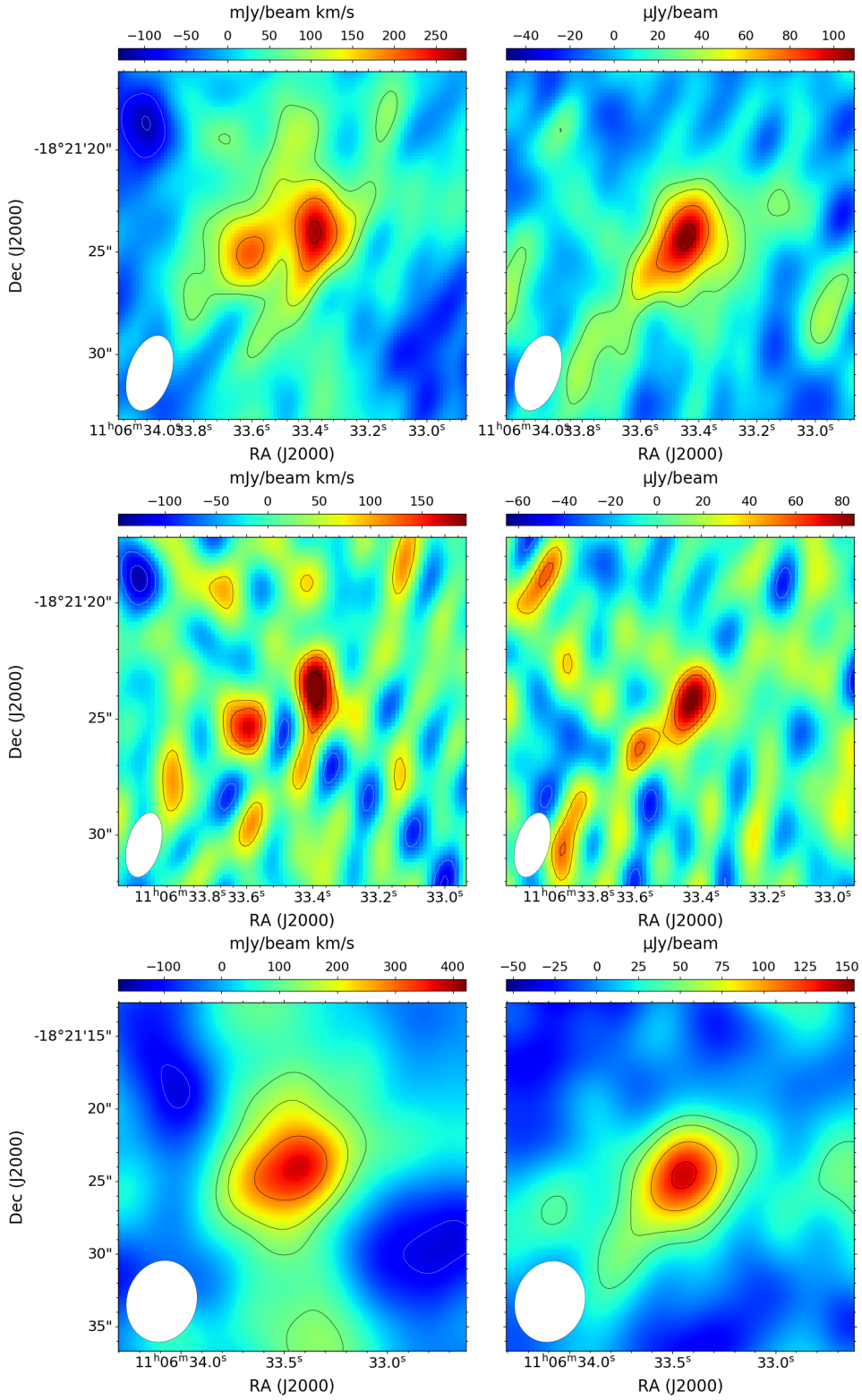

Figure 3.1: The **D-configuration dirty** velocity integrated CO(1-0) moment 0 map (left) and continuum map (right). The maps are made using natural weighting (top), Briggs weighting (centre) and 4″ Gaussian taper (bottom). Contours are in levels of $\pm 2\sigma$, $\pm 3\sigma$, $\pm 5\sigma$, $\pm 7\sigma$ and $\pm 9\sigma$, where σ is the RMS of the respective map. Negative contours are white. The maps are oversampled by a factor of 2 with respect to our Nyquist criterion. Beam sizes are shown at the lower left and are 3.81×2.10 arcsec^2 at a position angle of -17.91 deg, 2.86×1.43 arcsec^2 at a position angle of -15.25 deg and 5.70×4.81 arcsec^2 at a position angle of -16.89 deg for the three weightings, respectively. Continuum map beam sizes may vary slightly with respect to the moment 0 map beam size, see Table 3.1.

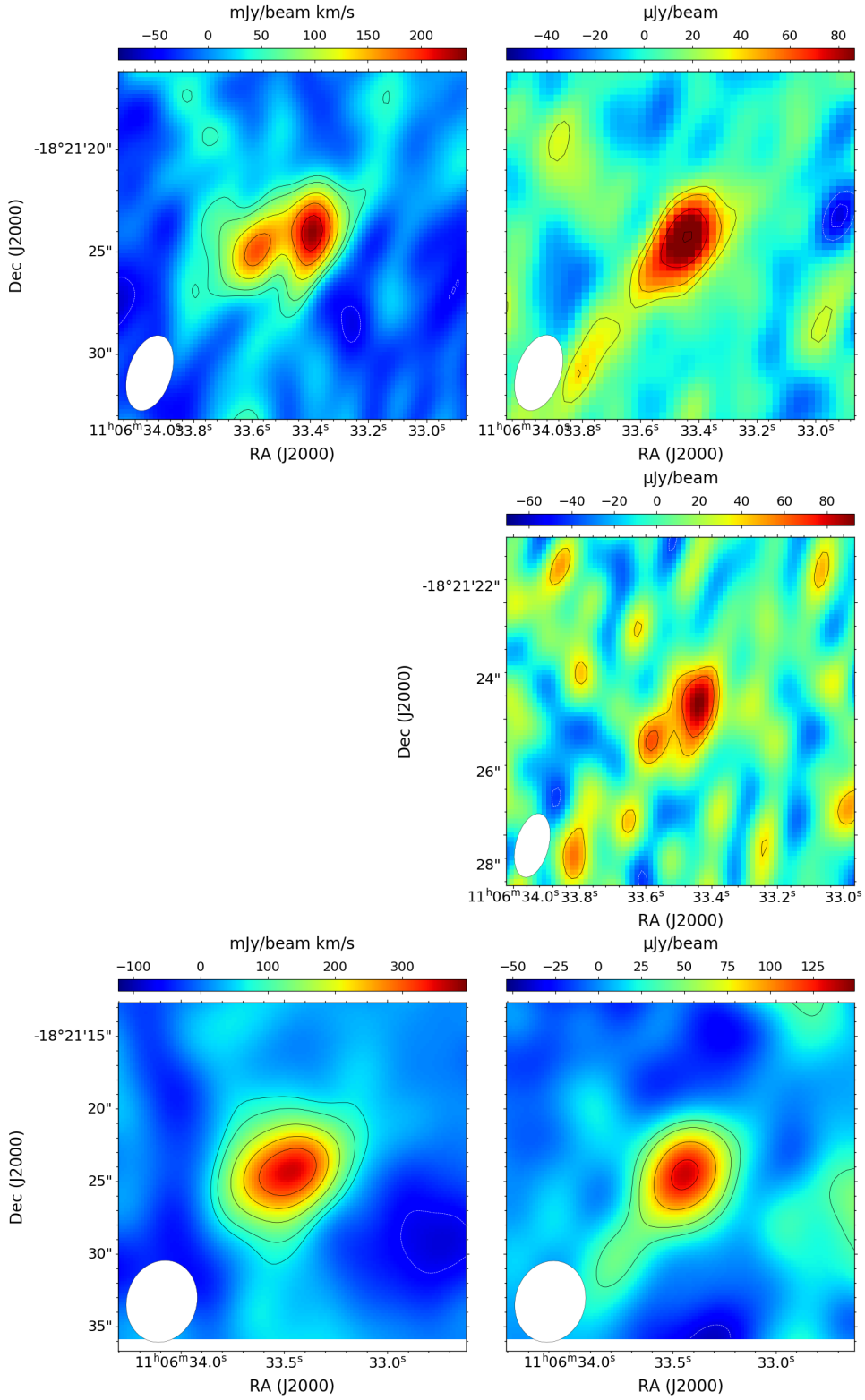

Figure 3.2: The **D-configuration clean** velocity integrated CO(1-0) moment 0 map (left) and continuum map (right). The maps are made using natural weighting (top), Briggs weighting (centre) and 4″ Gaussian taper (bottom). Contours are in levels of $\pm 2\sigma$, $\pm 3\sigma$, $\pm 5\sigma$, $\pm 7\sigma$ and $\pm 9\sigma$, where σ is the RMS of the respective map. Negative contours are white. The maps are oversampled by a factor of 2 with respect to our Nyquist criterion. Beam sizes are shown at the lower left and are 3.80×2.11 arcsec^2 at a position angle of -17.75 deg, 2.81×1.41 arcsec^2 at a position angle of -14.97 deg and 5.70×4.82 arcsec^2 at a position angle of -17.02 deg for the three weightings, respectively. Continuum map beam sizes may vary slightly with respect to the moment 0 map beam size, see Table 3.1.

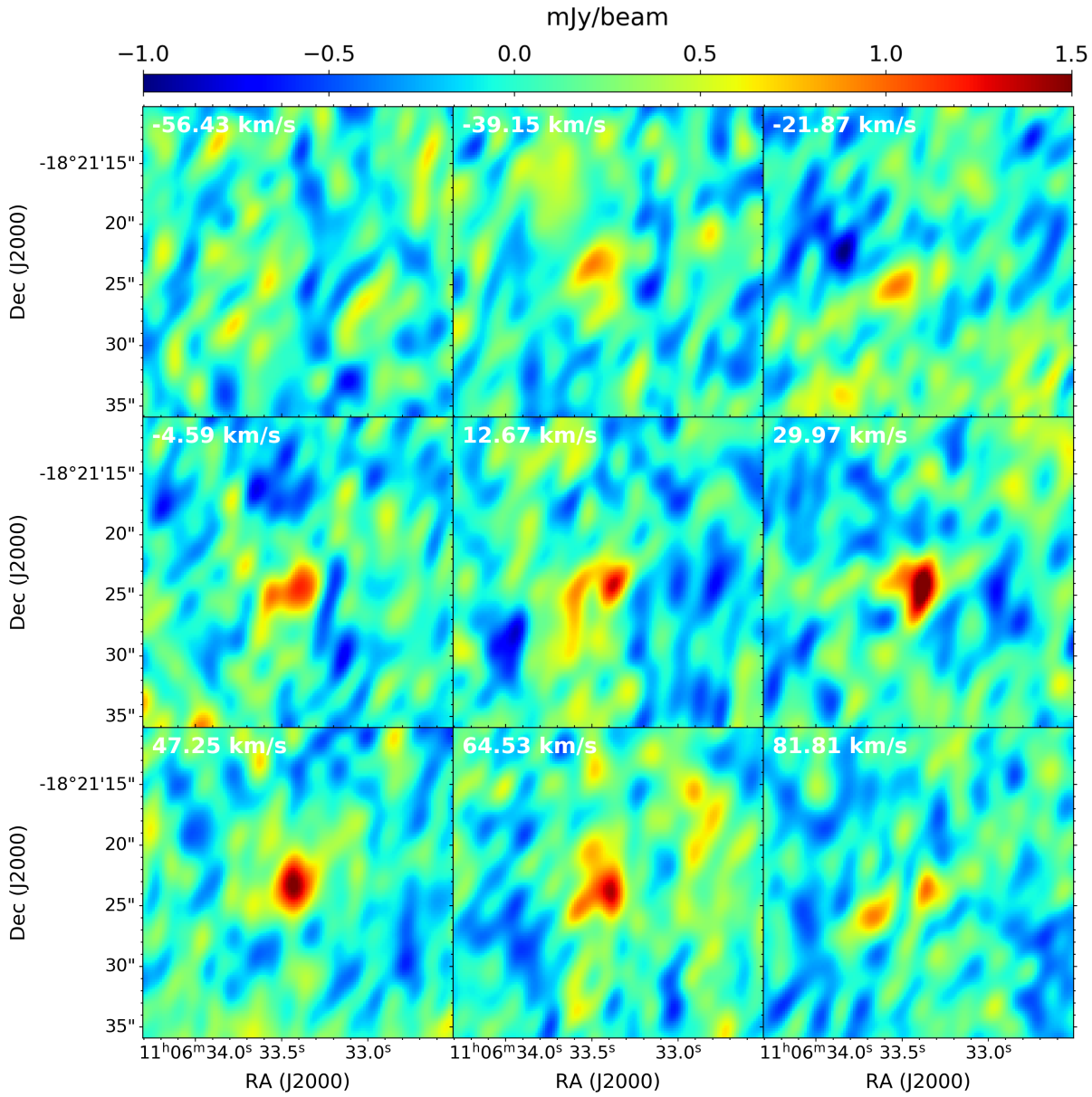

Figure 3.3: Channel maps ($\sim$17.3 km s^{-1} width) for the CO(1-0) emission line, relative to the reference frequency of $\nu_{\rm ref}$ = 34.698233 GHz (CO(1-0) line at a redshift of z = 2.3221). These channel maps are selected from the clean natural weighted cube of the D-configuration data. These maps show clearly that the line emission has a velocity-dependent structure. The top left map contains no (significant) line structure and is given as reference.

Table 3.3: Summary of measurements from the **clean** velocity integrated line and continuum maps (all three weightings) of **all configurations**. Integration quantities are measured within $3\sigma_{\rm RMS}$ regions, where σ_{1-0} and $\sigma_{34.7GHz}$ are the used RMS values. If two images are resolved, peak surface brightnesses for the fainter image are given in parentheses. A hyphen (-) indicates the quantity was not retrievable from the data. The uncertainty in surface brightness and flux density are set to 10%, as derived from the amplitude spreads (see Fig. 2.6).

Config.	Weighting	$\Delta\theta_{1-0}$ (arcsec)	$S_{1-0}\Delta v$ (Jy km s^{-1})	$I_{1-0}^{\rm max}$ (Jy/beam km s^{-1})	σ_{1-0} (mJy/beam km s^{-1})	$\Delta\theta_{34.7\rm GHz}$ (arcsec)	$S_{34.7GHz}$ (μJy)	$I_{34.7\rm GHz}^{\rm max}$ (μJy/beam)	$\sigma_{34.7\rm GHz}$ (μJy/beam)
D	Natural	3.0 ± 0.3	0.36 ± 0.04	0.24 ± 0.03 (0.19 ± 0.02)	24 ± 3	-	92 ± 10	107 ± 11	15 ± 2
	Briggs	-	-	-	-	2.6 ± 0.3	52 ± 6	98 ± 10 (70 ± 7)	21 ± 2
	4″ Taper	-	0.42 ± 0.05	0.36 ± 0.04	33 ± 4	-	98 ± 10	136 ± 14	18 ± 4
C	Natural	-	-	-	-	2.6 ± 0.2	51 ± 6	83 ± 9 (65 ± 7)	18 ± 2
C&D	Natrual	3.4 ± 0.4	0.20 ± 0.02	0.11 ± 0.02 (0.11 ± 0.02)	18 ± 2	2.5 ± 0.3	78 ± 8	82 ± 9 (62 ± 7)	12 ± 2
	Briggs	-	-	-	-	2.6 ± 0.3	76 ± 8	86 ± 9 (80 ± 8)	18 ± 2
	2″ Taper	-	0.49 ± 0.05	0.25 ± 0.03	27 ± 3	-	100 ± 10	108 ± 11	14 ±2

image has a peak surface brightness of $I_{1-0}^{\rm max,A} = 0.24 \pm 0.03$ Jy/beam km s^{-1} and the fainter image $I_{1-0}^{\rm max,B} = 0.19 \pm 0.02$ Jy/beam km s^{-1}, which yields a peak surface brightness ratio of 1.3 ± 0.2. The 4″ tapered map yields an integrated flux density of $S_{1-0}\Delta v = 0.42 \pm 0.05$ Jy km s^{-1} with a single 10.9σ peak surface brightness of $I_{1-0}^{\rm max} = 0.36 \pm 0.04$ Jy/beam km s^{-1}, a slight increase compared to the natural data.

All quantities derived from the clean line and continuum maps are summarised in Table 3.3. For completeness, the quantities derived from the dirty data are summarised in Table 3.2.

By integrating the surface brightness over a $3\sigma_{RMS}$ region for every channel map, a flux density profile is made as a function of radio velocity. The radio velocities are determined using Eq. 2.12 with respect to the reference frequency, $\nu_{\rm ref} = 34.698233$ GHz. The reference frequency is set to the observed frequency of a CO(1-0) line ($\nu_{1-0} = 115.271$ GHz) emitted at a redshift of $z = 2.3221$, according to Eq. 2.11. For all cubes, spectral profiles are obtained, to which a simple Gaussian profile is fitted,

$$S_\nu(v_{\rm radio}) = A \exp\left[\frac{-(v_{\rm radio} - B)^2}{2C^2}\right], \tag{3.1}$$

where A, B and C are the fit parameters representing the amplitude, centre position and shape of the profile, respectively. From the shape parameter C the full width half maximum (FWHM) of the spectral line can be found using

$$\text{FWHM} = 2C\sqrt{2\ln 2}. \tag{3.2}$$

If the spectral profile shows a double horned structure, a double Gaussian profile is fitted additionally. All numerical fits are done using the *curve_fit* function from `SciPy`'s optimize module, which uses non-linear least squares to find the best fit parameters. Finally, the integrated flux of the (single Gaussian) fit profile can be found using standard integration,

$$S_\nu \Delta\nu = \int_{-\infty}^{\infty} S_\nu(v_{\rm radio})\ {\rm d}v_{\rm radio} = AC\sqrt{2\pi}, \tag{3.3}$$

where A and C are the aforementioned fit parameters.

From the dirty and clean cubes, spectral profiles are made and are shown in Figure 3.4. The dirty spectra are shown as comparison for the clean spectra. All spectra show a highly asymmetric double horn profile, consistent with previous observations done by Sharon et al. (2016). For all cubes the single Gaussian profile provides a sub-optimal fit, whereas the double Gaussian profile provides a significantly better fit.

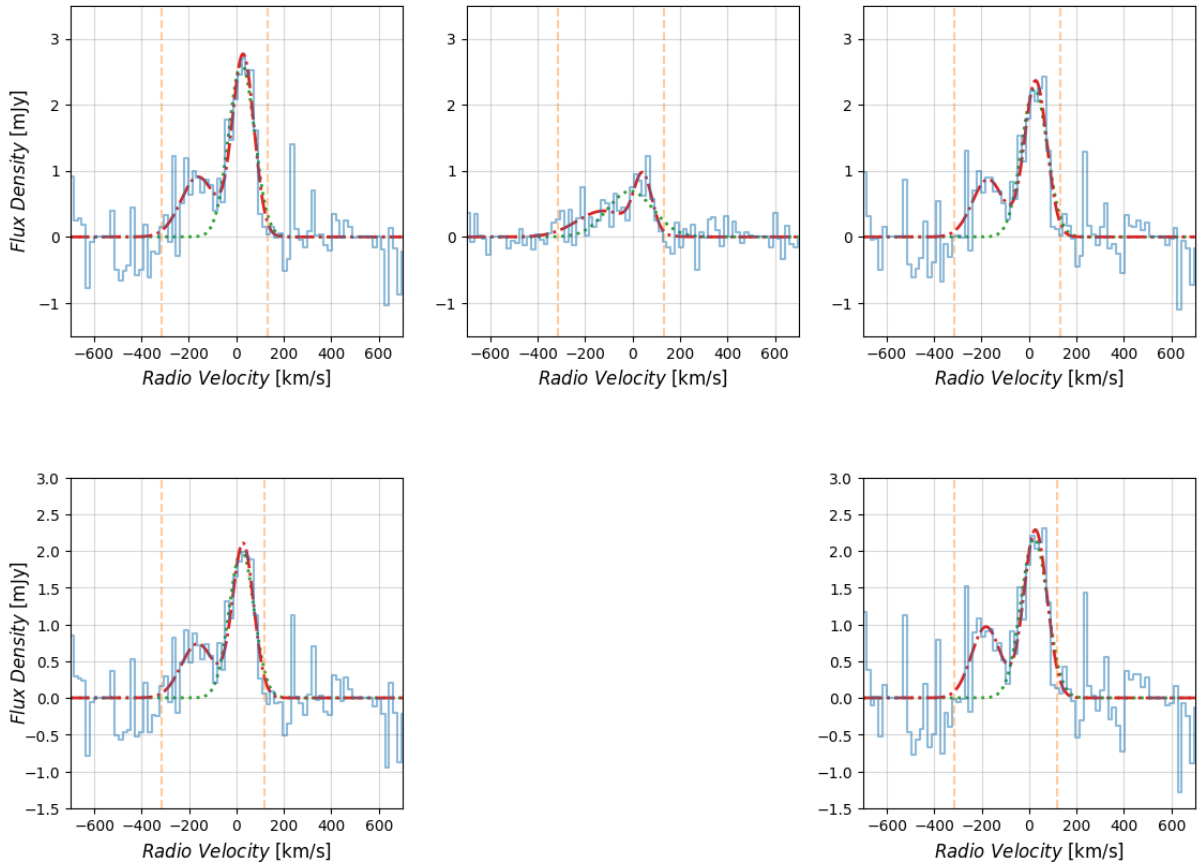

Figure 3.4: Integrated spectra of the CO(1-0) emission from the natural weighted (left), Briggs weighted (centre) and 4″ tapered (right) **D-configuration** data, plotted relative to the systemic velocity for $z = 2.3321$ (Eq. 2.11). The first row shows the dirty spectra and the second row the clean spectra. The Briggs weighted cube could not be cleaned due to poor the signal-to-noise ratio in the channel maps. The dotted line is the best single Gaussian fit and the dashed line the best double Gaussian fit. The data is extracted from a $3\sigma_{\mathrm{RMS}}$ contour of the corresponding moment 0 map. Uncertainties are not shown to improve clarity and no smoothing of the spectrum is applied.

Table 3.4: Summary of best fit parameters as obtained for single and double Gaussian profiles (all three weightings) from the **dirty D-configuration** data. Corresponding spectral profiles and fits are shown in Figure 3.4. The double Gaussian profile is split in two rows: the first row represents the higher frequency peak (lower radio velocity) and the second row the lower frequency peak (higher radio velocity). Uncertainties are those from the numerical fitting algorithm.

Weighting	Fit	S/N	$S_\nu \Delta v$ (mJy km s^{-1})	$I_\nu^{\max}$ (mJy)	FWHM (km s^{-1})	z_{1-0}	Δv_{peaks} (km s^{-1})	$I_A^{\max}/I_B^{\max}$
Natural	Single	5.7	354 ± 8	2.6 ± 0.2	127 ± 11	2.3223 ± 0.0001	-	-
	Double	2.0	478 ± 12	0.9 ± 0.2	170 ± 49	2.3214 ± 0.0002	190 ± 20	3.0 ± 0.8
		6.0		2.7 ± 0.3	107 ± 12			
Briggs	Single	3.2	168 ± 7	0.69 ± 0.08	228 ± 30	2.3220 ± 0.0002	-	-
	Double	1.8	191 ± 11	0.39 ± 0.08	266 ± 102	2.3217 ± 0.0003	166 ± 49	2.1 ± 0.7
		3.8		0.8 ± 0.2	88 ± 23			
4″ Taper	Single	5.0	306 ± 8	2.2 ± 0.2	128 ± 14	2.3223 ± 0.0001	-	-
	Double	2.0	422 ± 12	0.9 ± 0.2	156 ± 45	2.3213 ± 0.0001	201 ± 18	2.7 ± 0.7
		5.3		2.4 ± 0.3	110 ± 14			

For the clean natural weighted cube the single Gaussian profile gives a peak surface brightness of 2.0 ± 0.2 mJy and a FWHM of 123 ± 14 km s^{-1}. The peak of this fit yields a redshift of 2.3223 ± 0.0001, which is consistent with the CO(3-2) determined redshift ($z_{3-2} = 2.3221 \pm 0.0004$) from Riechers (2011) and the CO(1-0) determined redshift ($z_{1-0} = 2.3220 \pm 0.0002$) from Sharon et al. (2016). The double Gaussian provides a better looking fit. We obtain peak surface brightnesses of 0.7 ± 0.2 mJy and 2.1 ± 0.2 mJy and FWHMs of 162 ± 53 km s^{-1} and 106 ± 14 km s^{-1} for the higher and lower frequency peaks, respectively. The flux density ratio between the two peaks is 3.0 ± 0.9, similar to the 2.7 ± 0.7 as found by Sharon et al. (2016). The two peaks are separated by 192 ± 21 km s^{-1} and using the centre between the peaks, we determine a redshift of 2.3213 ± 0.0002, which is not consistent within 3σ with any of the aforementioned values. The two fits yield an integrated flux of 263 ± 8 mJy km s^{-1} and 363 ± 12 mJy km s^{-1}, respectively. The latter is consistent with the measured value from the natural weighted moment 0 map, $S_{1-0}\Delta v = 0.36 \pm 0.04$ Jy km s^{-1}, indicating the double Gaussian profile provides a better fit than a single Gaussian profile.

The 4″ tapered cube yields similar results. The single Gaussian profile gives a peak surface brightness of 2.2 ± 0.3 mJy and a FWHM of 133 ± 17 km s^{-1}. The peak yields a redshift of 2.3223 ± 0.0001, similar to the natural fit. Again, the double Gaussian profile provides a better fit with peak surface brightnesses of 1.0 ± 0.3 mJy and 2.3 ± 0.3 mJy and FWHMs of 144 ± 44 km s^{-1} and 115 ± 16 km s^{-1} for the higher and lower frequency peak, respectively. The peak surface brightness ratio is 2.3 ± 0.8. The two peaks are separated by 208 ± 19 km s^{-1} and using the centre between the peaks, we determine a redshift of 2.3212 ± 0.0002, similar to the natural fit. The two fits yield an integrated flux of 306 ± 9 mJy km s^{-1} and 429 ± 13 mJy km s^{-1}, respectively, which is about 40% more flux than the natural fit. Again, the integrated flux of the double Gaussian fit is consistent with the measured value from the tapered moment 0 map, $S_{1-0}\Delta v = 0.42 \pm 0.05$ Jy km s^{-1}, indicating the double Gaussian profile provides a better fit.

A summary of the best fit parameters of the clean spectra is given in Table 3.5. For comparison, the best fit parameters of the dirty spectra is given in Table 3.4.

3.1.3 Velocity Fields

Three sets of dirty velocity fields (first moment maps) and velocity dispersion fields (second moment maps) are shown in Figure 3.5. However, only the natural weighted and 4″ tapered cube were able to be cleaned and are shown in Figure 3.6. All velocity fields, both dirty and clean, show a velocity gradient between two positive velocity values. In fact, the fields are dominated by positive velocities, which aligns with the dominant lower frequency peak of the according spectra.

The clean natural velocity field has a detection limit of $4\sigma_{\text{cube}}$, where σ_{cube} is the RMS of the natural weighted clean cube. This field shows a gradient of +47 to +30 km s^{-1} along the brighter image from North to South. The 4″ tapered field, also with a detection limit of $4\sigma_{\text{cube}}$, shows a gradient of +64

Table 3.5: Summary of best fit parameters as obtained for single and double Gaussian profiles from the **clean D-configuration** spectra. Corresponding spectral profiles and fits are shown in Figure 3.4. The double Gaussian profile is split in two rows: the first row represents the higher frequency peak (lower radio velocity) and the second row the lower frequency peak (higher radio velocity). Uncertainties are those from the numerical fitting algorithm.

Weighting	Fit	S/N	$S_\nu \Delta v$ (mJy km s^{-1})	$I_\nu^{\max}$ (mJy)	FWHM (km s^{-1})	z_{1-0}	$\Delta v_{\rm peaks}$ (km s^{-1})	$I_A^{\max}/I_B^{\max}$
Natural	Single	5.0	263 ± 8	2.0 ± 0.2	123 ± 14	2.3223 ± 0.0001	-	-
	Double	1.8	363 ± 12	0.7 ± 0.2	162 ± 53	2.3213 ± 0.0002	192 ± 21	3.0 ± 0.9
		5.2		2.1 ± 0.2	106 ± 14			
4″ Taper	Single	4.3	306 ± 9	2.2 ± 0.3	133 ± 17	2.3223 ± 0.0001	-	-
	Double	1.9	429 ± 13	1.0 ± 0.3	144 ± 44	2.3212 ± 0.0002	208 ± 19	2.3 ± 0.8
		4.5		2.3 ± 0.3	115 ± 16			

to +30 km s^{-1} from North to South with a dip in the middle of +20 km s^{-1}, which might be caused by noise structure. The lobe on the lower left of the field has a flat value of +13 km s^{-1} and is most likely not real as it completely disappears at higher σ detection limits. Both clean velocity dispersion fields have a central peak value of 24 and 33 km s^{-1}, respectively. The mean velocity dispersions for the natural field is 16 km s^{-1} (ignoring the near zero pixels) and 18 km s^{-1} for the 4″ tapered field (ignoring the near zero noise lobe). The values derived from velocity dispersion fields are sensitive to the detection limit, decreasing as the detection limit increases. The important feature is that the velocity dispersion peaks at approximately the same location as the peak of the line emission for both maps.

3.2 C-Configuration

3.2.1 Continuum Emission

The resulting dirty continuum maps for the natural weighted and 2″ tapered data are shown on the right in Figure 3.7. The natural continuum map is cleaned and is shown in Figure 3.8. The natural weighted map shows two fully resolved images above the $3\sigma_{\rm RMS}$ detection limit, whereas the 2″ tapered map only shows two partially resolved surface brightness peaks, both above the $3\sigma_{\rm RMS}$ detection limit. The continuum maps are not cleaned as a part of the flux is resolved out, as more focus is given to the CO(1-0) line data and as the C-configuration is mainly used to combine with the D-configuration data later on. The clean measurements are shown in Table 3.3 and the dirty measurements are shown in Table 3.2.

The clean natural weighted continuum map show two spatially resolved images, separated by $\Delta\theta_{34.7GHz} = 2.6 \pm 0.2$ arcsec, not consistent within 3σ with the optical separation. The map yields an integrated flux density of $S_{34.7\rm GHz} = 51 \pm 6$ μJy, with two (4.6σ and 3.6σ) peak surface brightnesses of $I_{34.7\rm GHz}^{\rm max,A} = 83 \pm 9$ μJy/beam and $I_{34.7\rm GHz}^{\rm max,B} = 65 \pm 7$ μJy/beam.

3.2.2 CO(1-0) Emission

The resulting dirty moment 0 maps for the natural weighted and 2″ tapered data are shown on the left in Figure 3.7. The dirty natural weighted moment 0 map shows a collection of scattered peaks which indicates most of the flux is resolved out at this angular resolution. The dirty 2″ tapered map does show a proper detection, including two different surface brightness peaks, but only barely. The fact that the line emission is not detectable in the natural weighted map (with a beam size of 1.07″ × 0.63″) indicates the emission is extended. The channel maps of both the weighted and tapered cubes do not show significant structure for the cleaning and hence no clean maps and no moment maps are presented. Although no clean measurements are made, dirty measurements are shown in Table 3.2.

To make sure the C-configuration observation does actually detect the CO(1-0) emission line, a spectrum is made from the dirty 2″ tapered cube, to check whether or not the spectrum contains two distinct peaks. The lower frequency peak is clearly detected, whereas there is only a marginal detection

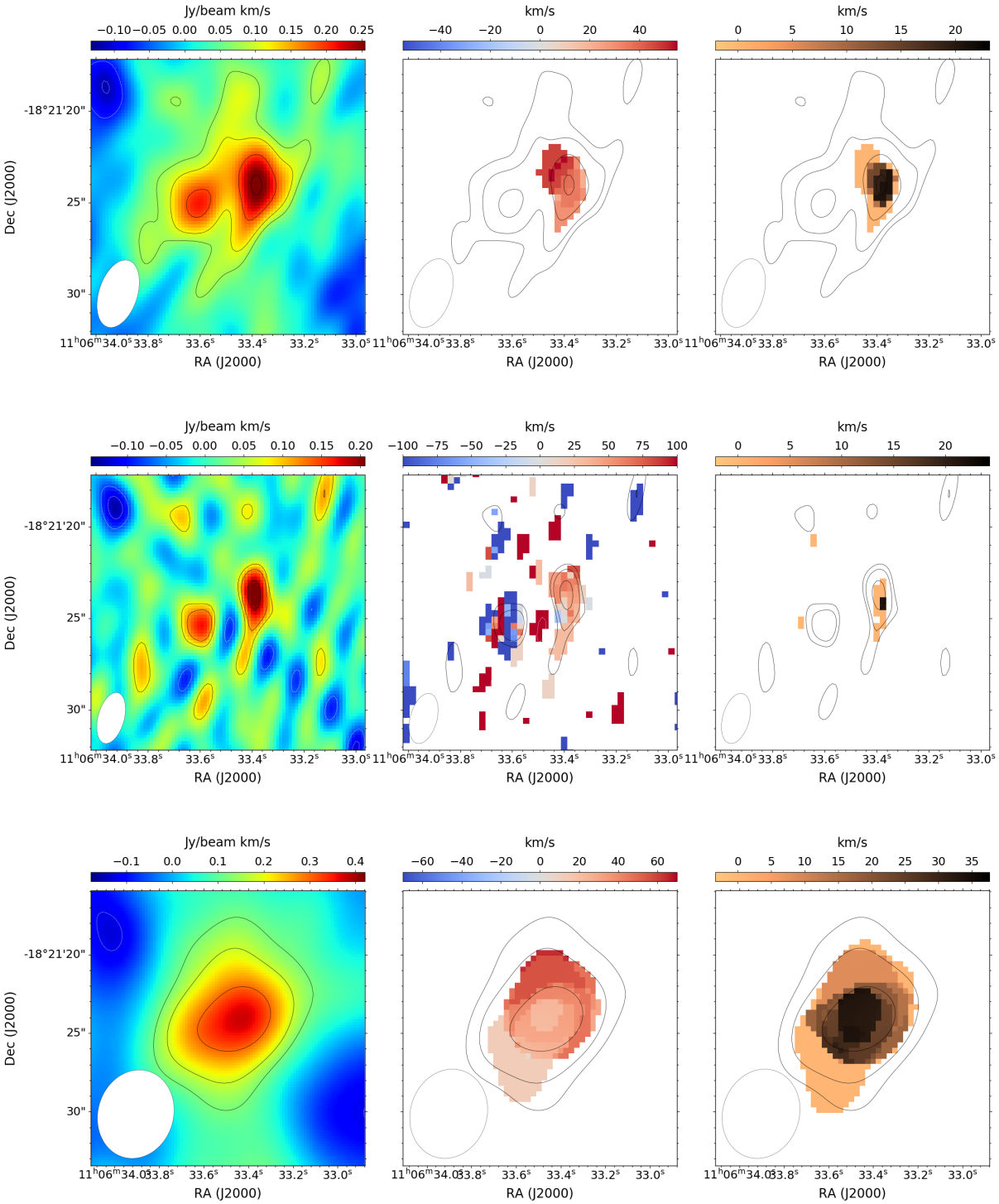

Figure 3.5: The **dirty D-configuration** moment maps for the natural weighted (top), Briggs weighted (centre) and 4″ tapered (bottom) data. From left to right: integrated CO(1-0) moment 0 map (zeroth moment), velocity field (first moment) and velocity dispersion (second moment). The latter two are shown with a $5\sigma_{\rm cube}$ (natural weighted map) and $4\sigma_{\rm cube}$ (Briggs weighted and 4″ tapered maps) detection limit. Contours are in levels of $\pm2\sigma$, $\pm3\sigma$, $\pm5\sigma$, $\pm7\sigma$ and $\pm9\sigma$, where σ is the RMS of the moment 0 map. Negative contours are white. The maps are Nyquist sampled with respect to our Nyquist criterion. Beam sizes are shown at the lower left and are 3.81×2.10 arcsec^2 at a position angle of -17.91 deg, 2.86×1.43 arcsec^2 at a position angle of -15.25 deg and 5.70×4.81 arcsec^2 at a position angle of -16.89 deg for the three weightings, respectively.

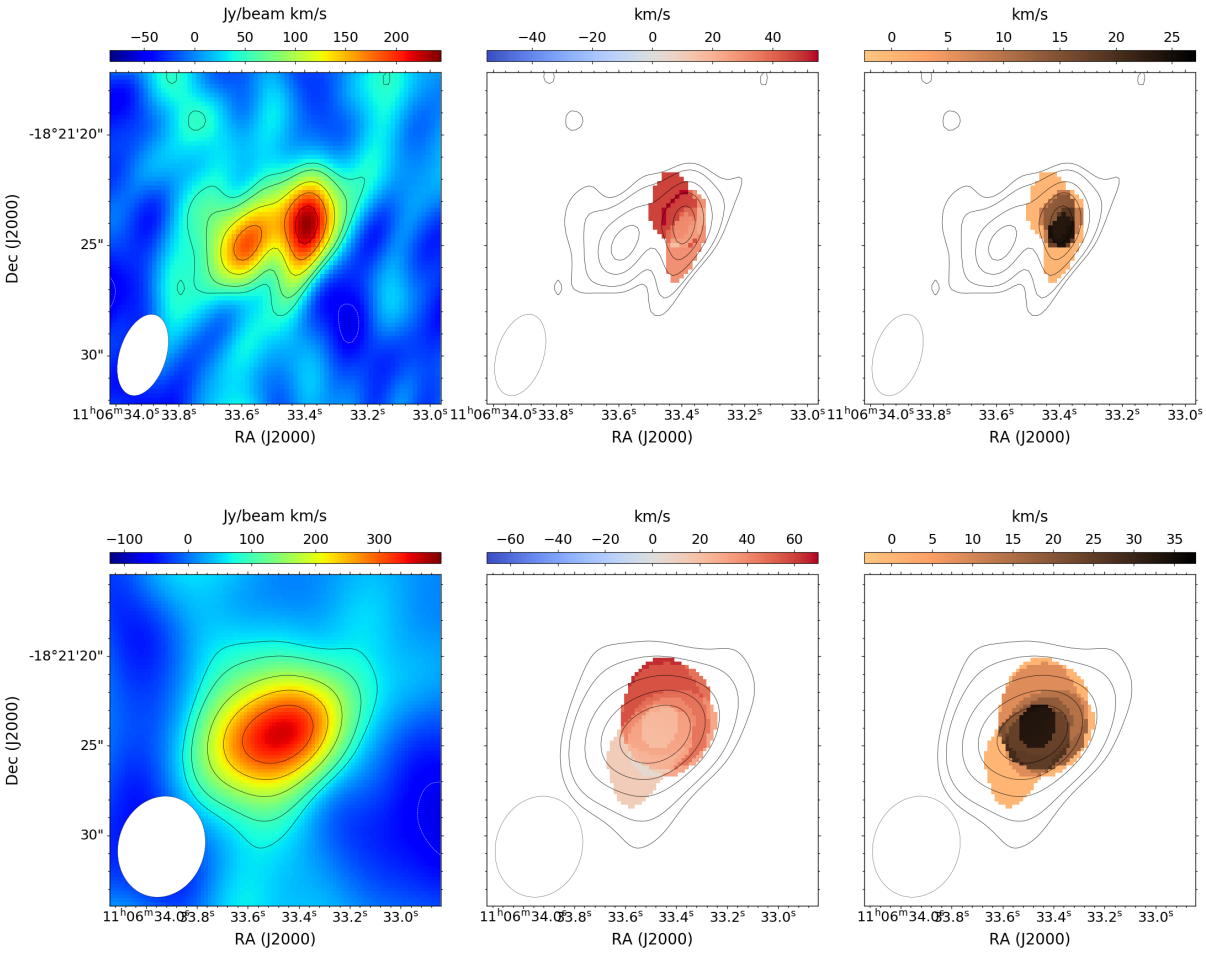

Figure 3.6: The **clean D-configuration** moment maps for the natural weighted (top) and 4″ tapered (bottom) data. From left to right: integrated CO(1-0) moment 0 map (zeroth moment), velocity field (first moment) and velocity dispersion (second moment). The latter two are shown with a $4\sigma_{\rm cube}$ detection limit. Contours are in levels of $\pm 2\sigma$, $\pm 3\sigma$, $\pm 5\sigma$, $\pm 7\sigma$ and $\pm 9\sigma$, where σ is the RMS of the moment 0 map. Negative contours are white. The maps are Nyquist sampled with respect to our Nyquist criterion. Beam sizes are shown at the lower left and are 3.80×2.11 arcsec^2 at a position angle of -17.75 deg and 5.70×4.82 arcsec^2 at a position angle of -17.02 deg for the two weightings, respectively.

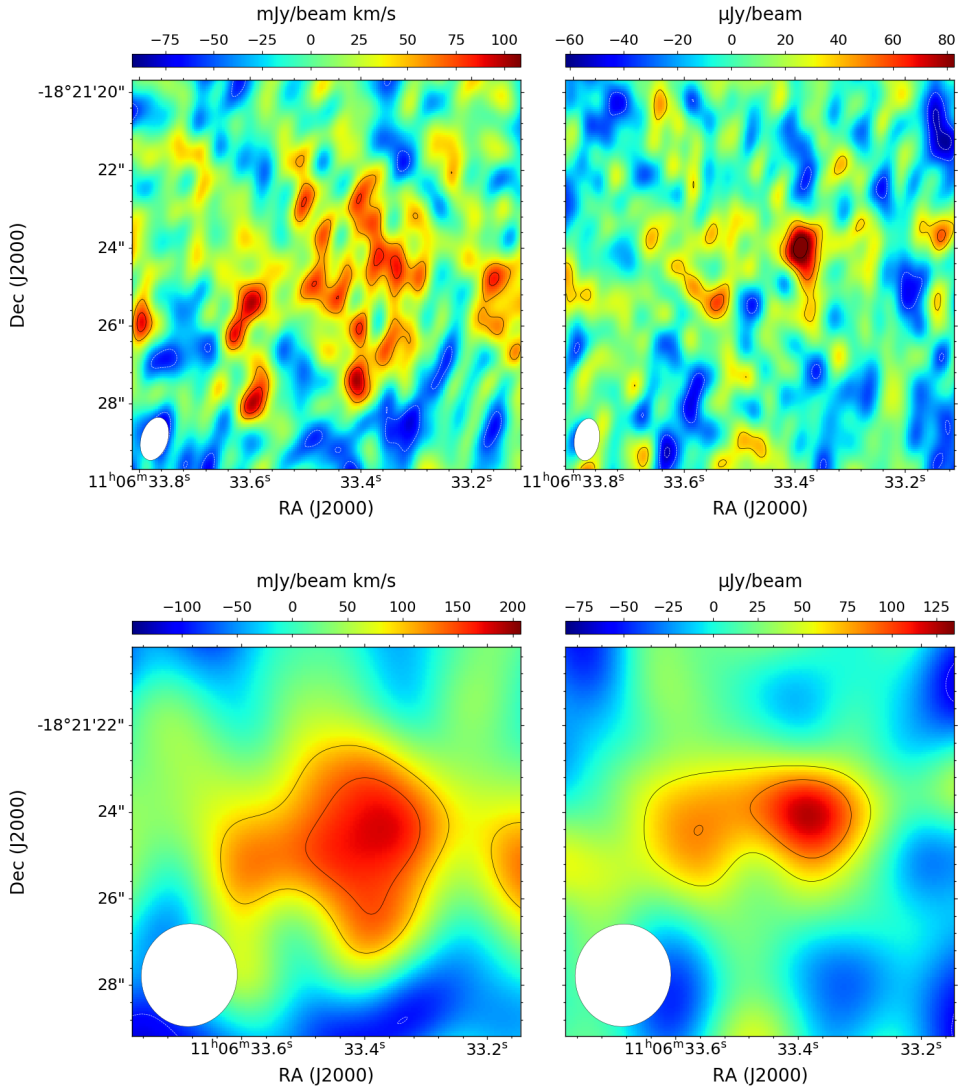

Figure 3.7: The **C-configuration dirty** velocity integrated CO(1-0) moment 0 map (left) and continuum map (right). The maps are made using natural weighting (top) and a 2″ Gaussian taper (bottom). Contours are in levels of $\pm 2\sigma$, $\pm 3\sigma$, $\pm 5\sigma$, $\pm 7\sigma$ and $\pm 9\sigma$, where σ is the RMS of the respective map. Negative contours are white. The maps are oversampled by a factor of 2 with respect to our Nyquist criterion. Beam sizes are shown at the lower left and are 1.07×0.63 arcsec^2 at a position angle of -8.28 deg and 2.38×2.22 arcsec^2 at a position angle of -8.91 deg for the two weightings, respectively. Continuum map beam sizes may vary slightly with respect to the moment 0 map beam size, see Table 3.1.

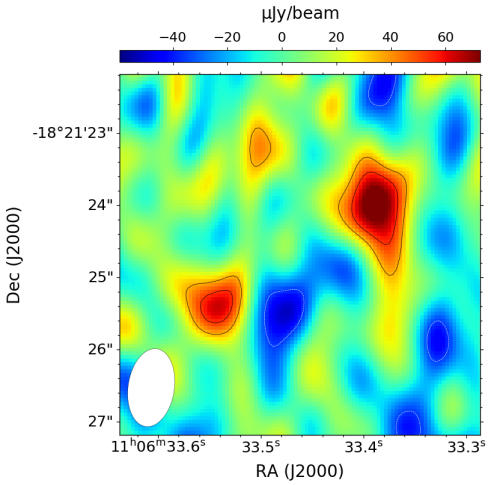

Figure 3.8: The **clean C-configuration** continuum map. The map is made using natural weighting. Contours are in levels of $\pm 2\sigma$, $\pm 3\sigma$, $\pm 5\sigma$, $\pm 7\sigma$ and $\pm 9\sigma$, where σ is the RMS of the respective map. Negative contours are white. The map is Nyquist sampled with respect to our Nyquist criterion. Beam sizes are shown at the lower left and are 1.09×0.64 arcsec^2 at a position angle of -8.36 deg.

Table 3.6: Summary of best fit parameters as obtained for single and double Gaussian profiles from the **dirty C-configuration** data. Corresponding spectral profile and fit are shown in Figure 3.9. The double Gaussian profile is split in two rows: the first row represents the higher frequency peak (lower radio velocity) and the second row the lower frequency peak (higher radio velocity). Uncertainties are those from the numerical fitting algorithm.

Weighting	Fit	S/N	$S_\nu \Delta v$ (mJy km s^{-1})	$I_\nu^{\max}$ (mJy)	FWHM (km s^{-1})	z_{1-0}	$\Delta v_{\rm peaks}$ (km s^{-1})	$I_A^{\max}/I_B^{\max}$
2″ Taper	Single	3.1	129 ± 8	1.2 ± 0.3	99 ± 21	2.3229 ± 0.0001	-	-
	Double	0.7	146 ± 10	0.3 ± 0.3	63 ± 78	2.3218 ± 0.0002	182 ± 35	4.0 ± 4.0
		3.1		1.2 ± 0.3	99 ± 21			

of the higher frequency peak, as shown in Figure 3.9. No clean measurements can be made, but dirty measurements are provided for completeness in Table 3.6.

3.3 C&D-Configuration

3.3.1 Continuum Emission

All clean continuum maps are shown on the right of Figure 3.10. Both the natural weighted and Briggs weighted maps show two fully spatially resolved images, separated by $\Delta\theta_{34.7\rm GHz} = 2.5 \pm 0.3$ arcsec and $\Delta\theta_{34.7\rm GHz} = 2.6 \pm 0.3$ arcsec, respectively. These separations are inconsistent with the moment 0 map separations of the D-configuration data. The 2″ tapered map shows a single image with a single flux density peak.

The clean natural weighted continuum map yields an integrated flux density of $S_{34.7\rm GHz} = 78 \pm 8$ μJy, with two fully resolved surface brightness peaks (6.8σ and 5.2σ) of $I^{\rm max,A}_{34.7\rm GHz} = 82 \pm 9$ μJy/beam and $I^{\rm max,B}_{34.7\rm GHz} = 62 \pm 7$ μJy/beam, yielding a peak surface brightness ratio of 1.3 ± 0.2. The Briggs weighted map yields an integrated flux density of $S_{34.7\rm GHz} = 76 \pm 8$ μJy, similar to the natural weighted data. It contains two fully resolved surface brightness peaks (4.8σ and 4.4σ) of $I^{\rm max,A}_{34.7\rm GHz} = 86 \pm 9$ μJy/beam and $I^{\rm max,B}_{34.7\rm GHz} = 80 \pm 8$ μJy/beam, yielding a peak surface brightness ratio of 1.1 ± 0.2, which is lower than the natural peak surface brightness ratio but within uncertainty range. Finally, the 2″ tapered map yields an integrated flux density of $S_{34.7\rm GHz} = 100 \pm 10$ μJy, which is an increase of about 30% over the

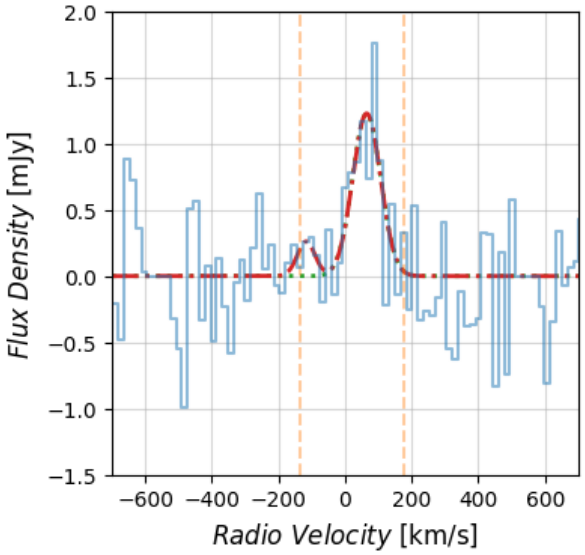

Figure 3.9: Integrated spectrum of the CO(1-0) emission from 2″ tapered **dirty C-configuration** data, plotted relative to the systemic velocity for $z = 2.3321$. No data could be extracted form the Briggs weighted cube due to poor S/N in the channel maps. The dotted line is the best single Gaussian fit and the dashed line the best double Gaussian fit. The data is extracted from a $3\sigma_{\rm RMS}$ contour of the corresponding moment 0 map. Uncertainties are not shown to improve clarity and no smoothing of the spectrum is applied.

other two maps. The single detected 7.7σ peak has a peak surface brightness of $I^{\rm max}_{34.7{\rm GHz}} = 108 \pm 11$ μJy/beam.

3.3.2 CO(1-0) Emission

The natural weighted and 2″ tapered channel maps contained significant structure, whereas the Briggs weighted channel maps did not and hence were not cleaned. The resulting clean moment 0 maps are shown on the left in Figure 3.10. The clean natural moment 0 map shows two fully resolved images with a separation of $\Delta\theta_{1-0} = 3.4 \pm 0.4$ arcsec, consistent with both the measured moment 0 map separation of the D-configuration data and the aforementioned literary value. The tapered map does not show two spatially resolved images, but does contain two barely distinct peaks.

The clean natural moment 0 map yields an integrated flux density of $S_{1-0}\Delta v = 0.20 \pm 0.02$ Jy km s^{-1} within a $3\sigma_{\rm RMS}$ region. In this moment 0 map the two images are fully spatially resolved and separated by $\Delta_{1-0} = 3.4 \pm 0.4$ arcsec, also consistent with Kochanek et al. (1999). Both peaks (6.1σ and 6.1σ) have a peak surface brightness of $I^{\rm max}_{1-0} = 0.11 \pm 0.02$ Jy/beam km s^{-1}, yielding a flux density ratio of 1.0 ± 0.3. The 2″ tapered map yields an integrated flux density of $S_{1-0}\Delta v = 0.49 \pm 0.05$ Jy km s^{-1}, an increase of 145% compared to the clean natural C&D-configuration data and an increase of 17% compared to the clean 4″ tapered D-configuration data. The map has a single 9.3σ peak surface brightness of $I^{\rm max}_{1-0} = 0.25 \pm 0.03$ Jy/beam km s^{-1}.

All quantities derived from the clean line and continuum maps are summarised in Table 3.3. For completeness the quantities derived from the dirty data are summarised in Table 3.2.

From the clean cubes spectral profiles were made and are shown in Figure 3.11. All spectra show an asymmetric double horn profile and the double Gaussian profile provides the best fits.

For the clean natural weighted cube the single Gaussian profile gives a peak surface brightness of 1.3 ± 0.2 mJy and a FWHM of 118 ± 23 km s^{-1}. The peak of this fit yields a redshift of 2.3229 $\pm$ 0.0002, inconsistent with the aforementioned literary values. Again caused by the single Gaussian fitting itself onto the brighter peak and hence not providing a good measure of the redshift. The double Gaussian obtained peak surface brightnesses of 0.4 ± 0.2 mJy and 1.3 ± 0.2 mJy for the higher and lower frequency peaks, respectively. The flux density ratio between the two peaks is 3.3 ± 1.7, which has

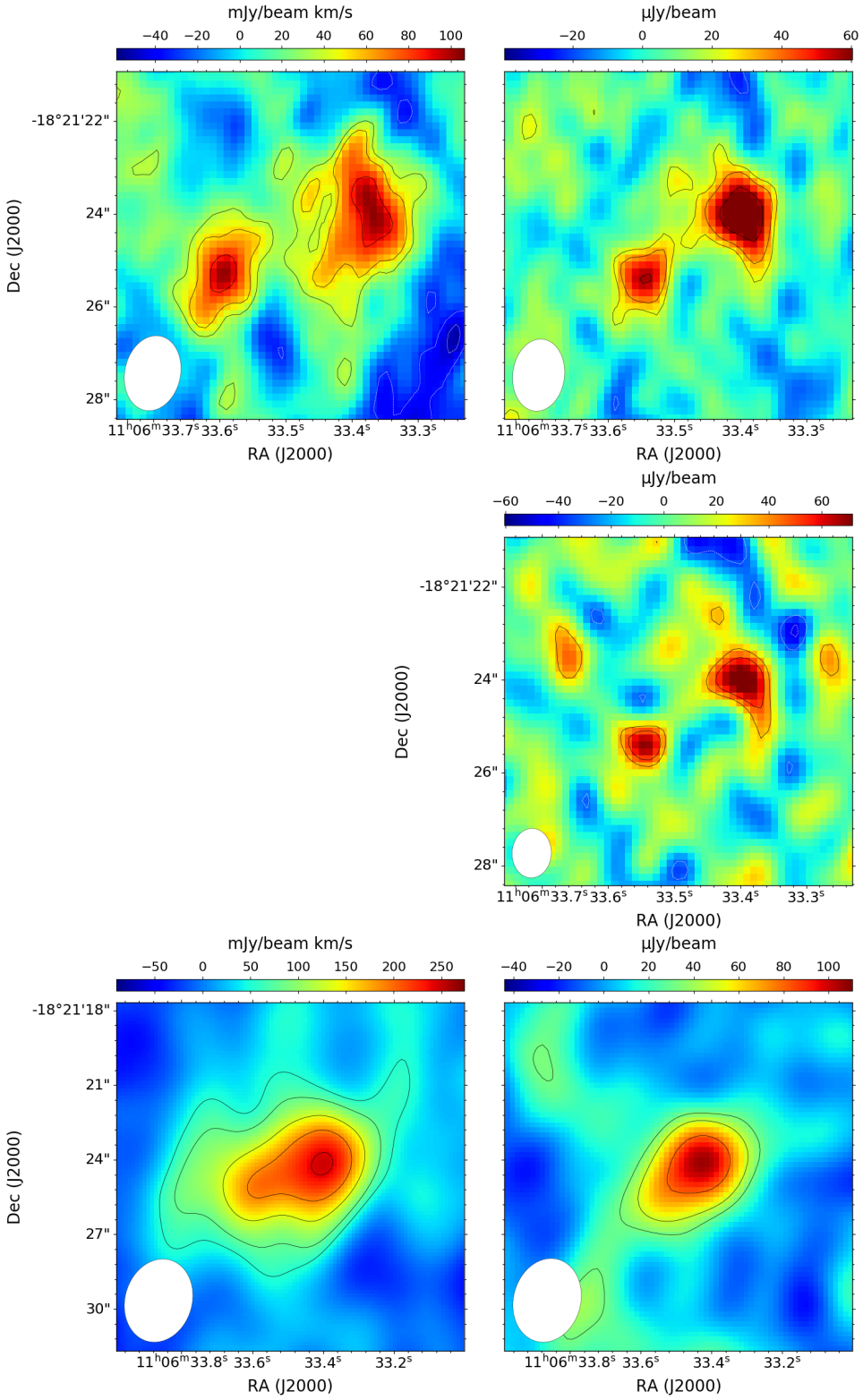

Figure 3.10: The **clean C&D-configuration** velocity integrated CO(1-0) line (left) and continuum (right) maps. The maps are made using natural weighting (left), Briggs weighting (centre) and a $2''$ Gaussian taper (bottom). Contours are in levels of $\pm 2\sigma$, $\pm 3\sigma$, $\pm 5\sigma$, $\pm 7\sigma$ and $\pm 9\sigma$, where σ is the RMS of the respective map. Negative contours are white. The maps are Nyquist sampled with respect to our Nyquist criterion. Beam sizes are shown at the lower left and are 1.64×1.20 arcsec^2 at a position angle of -12.02 deg, 1.07×0.85 arcsec^2 at a position angle of -2.84 deg and 3.39×2.69 arcsec^2 at a position angle of -16.33 deg for the three weightings, respectively. Continuum map beam sizes may vary slightly with respect to the moment 0 map beam size, see Table 3.1.

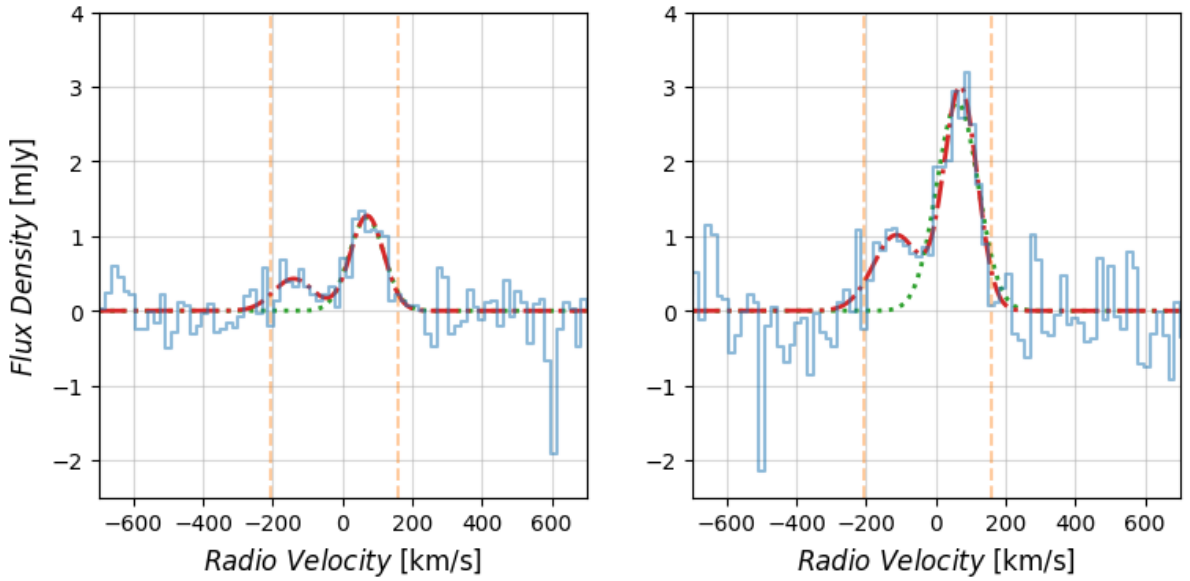

Figure 3.11: Integrated spectra of the CO(1-0) emission from the natural weighted (left) and 2″ tapered (right) **clean C&D-configuration** data, plotted relative to the systemic velocity for $z = 2.3321$ (Eq. 2.11). The Briggs weighted cube could not be cleaned due to poor signal-to-noise ratio of the channel maps. The dotted line is the best single Gaussian fit and the dashed line the best double Gaussian fit. The data is extracted from a $3\sigma_{\mathrm{RMS}}$ contour of the corresponding moment 0 map. Uncertainties are not shown to improve clarity and no smoothing of the spectrum is applied.

a large uncertainty as the fainter peak is at noise level. The two peaks are separated by 211 ± 32 km s^{-1} and using the centre between the peaks we determine a redshift of 2.3217 ± 0.0002, consistent with both the CO(3-2) determined redshift from Riechers (2011) and the CO(1-0) determined redshift from Sharon et al. (2016). The two fits yield an integrated flux of 157 ± 8 mJy km s^{-1} and 214 ± 11 mJy km s^{-1}. Similar to the D-configuration data only the double Gaussian profile has a similar integrated flux density to the measured value from the corresponding moment 0 map, $S_{1-0}\Delta v 0.20 \pm 0.02$ Jy km s^{-1}, indicating the double Gaussian profile provides a better fit.

The 2″ tapered cube yielded significantly higher flux density values. The single Gaussian profile gives a peak surface brightness of 2.8 ± 0.4 mJy and a FWHM of 140 ± 19 km s^{-1}. The peak yields a redshift of 2.3228 ± 0.0001, similar to the natural fit. The double Gaussian profile provided peak surface brightnesses of 1.0 ± 0.4 mJy and 3.0 ± 0.4 mJy and FWHMs of 157 ± 77 km s^{-1} and 113 ± 21 km s^{-1}. The peak surface brightness ratio is 3.0 ± 1.2, where the fainter peak is again at noise level. The two peaks are separated by 184 ± 32 km s^{-1} and using the centre between the peaks we determine a redshift of 2.3219 ± 0.0002, consistent with both aforementioned literary values. The two fits yield an integrated flux of 416 ± 11 mJy km s^{-1} and 528 ± 16 mJy km s^{-1}, respectively, which is about 150% more flux than the natural fit. This indicates the natural fit resolves out a lot of flux from the extended emission structure. Again, the integrated flux of the double Gaussian fit is consistent with the measured value from the tapered moment 0 map of $S_{1-0}\Delta v = 0.49 \pm 0.05$ Jy km s^{-1}, indicating the double Gaussian profile provides a better fit.

A summary of the best fit parameters of the clean spectra is given in Table 3.7.

3.3.3 Velocity Fields

Two sets of clean velocity fields (first moment maps) and velocity dispersion fields (second moment maps) are presented in Figures 3.12 and 3.13. All clean velocity fields show at least a marginal velocity gradient between two positive velocity values. In fact, the fields are dominated by positive velocities, which aligns with the dominant lower frequency peak of the according spectra.

Table 3.7: Summary of best fit parameters as obtained for single and double Gaussian profiles from the natural weighted and 2″ tapered **clean C&D-configuration** data. Corresponding spectral profiles and fits are shown in Figure 3.11. The double Gaussian profile is split in two rows: the first row represents the higher frequency peak (lower radio velocity) and the second row the lower frequency peak (higher radio velocity). Uncertainties are those from the numerical fitting algorithm.

Weighting	Fit	S/N	$S_\nu \Delta v$ (mJy km s^{-1})	$I_\nu^{\max}$ (mJy)	FWHM (km s^{-1})	z_{1-0}	$\Delta v_{\rm peaks}$ (km s^{-1})	$I_A^{\max}/I_B^{\max}$
Natural	Single	3.1	157 ± 8	1.3 ± 0.2	118 ± 23	2.3229 ± 0.0002	-	-
	Double	1.1	214 ± 11	0.4 ± 0.2	135 ± 76	2.3217 ± 0.0002	211 ± 32	3.3 ± 1.7
		3.2		1.3 ± 0.2	112 ± 23			
4″ Taper	Single	3.9	416 ± 11	2.8 ± 0.4	140 ± 19	2.3228 ± 0.0001	-	-
	Double	1.4	528 ± 16	1.0 ± 0.4	157 ± 77	2.3219 ± 0.0002	184 ± 32	3.0 ± 1.3
		4.1		3.0 ± 0.4	113 ± 21			

The presented clean natural velocity field has a detection limit of $3\sigma_{\rm cube}$, where $\sigma_{\rm cube}$ is the RMS of the natural weighted clean cube. This field shows a gradient of +123 to +71 km s^{-1} along the brighter image from North to South and another gradient of +54 to +37 km s^{-1} along the fainter image from South-West to North-East. The image contains a lot of unexpected structure most likely caused by the low signal-to-noise ratio of the detection. Both gradients remain in a $4\sigma_{\rm cube}$ detection limit moment map, but the noise structure is significantly reduced. The 2″ tapered field shows a single gradient of +96 to +64 km s^{-1} from North to South. In the $4\sigma_{\rm cube}$ field one can even marginally recognise a second gradient of +87 to +37 km s^{-1} from South-West to North-East. The natural velocity dispersion fields clearly show a peaked velocity dispersion at the centre of the line emission. The peaks have a value of 26 and 35 km s^{-1} for the brighter and fainter image, respectively. The region around both centre values quickly drop off to near zero dispersion values. The tapered velocity dispersion field has an average flat value of about 30 km s^{-1}, which decreases to 24 km s^{-1} in the higher detection limit fields. However, most notably is the lack of two peak central values compared to the natural dispersion field. Instead, the peak velocity dispersion is located in between the two surface brightness peaks, possibly because the two images are not fully spatially resolved, similar to the D-configuration tapered dispersion field.

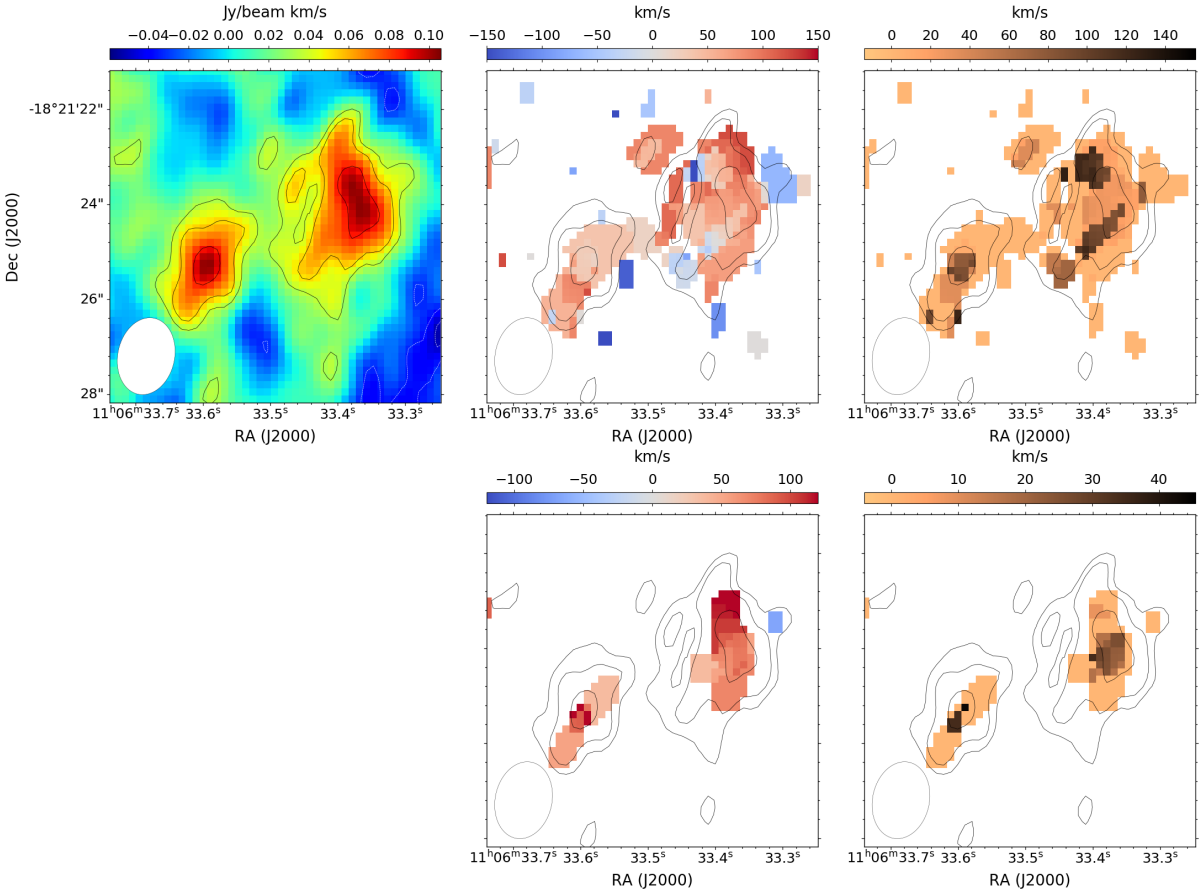

Figure 3.12: The **clean C&D-configuration** moment maps for the **natural weighted** data. From left to right: integrated CO(1-0) moment 0 map (zeroth moment), velocity field (first moment) and velocity dispersion (second moment). The latter two are shown with a $3\sigma_{\rm cube}$ (upper row) and $4\sigma_{\rm cube}$ (bottom row) detection limit. Contours are in levels of $\pm2\sigma$, $\pm3\sigma$, $\pm5\sigma$, $\pm7\sigma$ and $\pm9\sigma$, where σ is the RMS of the moment 0 map. Negative contours are white. The maps are Nyquist sampled with respect to our Nyquist criterion. Beam sizes are shown at the lower left and are 1.64×1.20 arcsec^2 at a position angle of -12.02 deg.

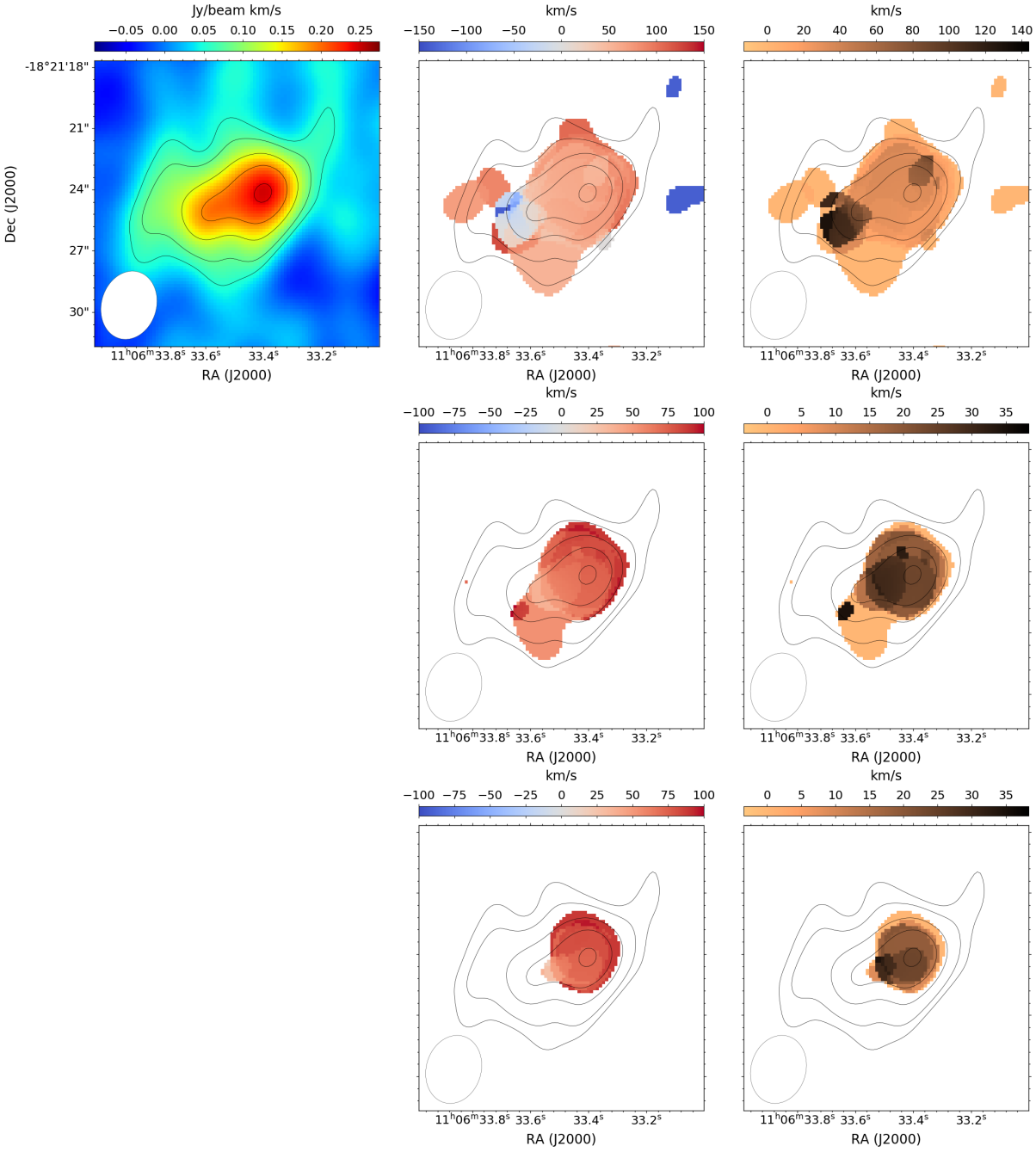

Figure 3.13: The **clean C&D-configuration** moment maps for the **2″ tapered** data. From left to right: integrated CO(1-0) moment 0 map (zeroth moment), velocity field (first moment) and velocity dispersion (second moment). The latter two are shown with a $3\sigma_{\rm cube}$ (upper row), $4\sigma_{\rm cube}$ (centre row) and $5\sigma_{\rm cube}$ (bottom row) detection limit. Contours are in levels of $\pm2\sigma$, $\pm3\sigma$, $\pm5\sigma$, $\pm7\sigma$ and $\pm9\sigma$, where σ is the RMS of the moment 0 map. Negative contours are white. The maps are Nyquist sampled with respect to our Nyquist criterion. Beam sizes are shown at the lower left and are 3.39×2.69 arcsec^2 at a position angle of -16.33 deg.

Chapter 4

Discussion

4.1 CO(1-0) Emission at Redshift $z = 2.3221$

4.1.1 Spectrum Properties

All spectra show a highly asymmetric double horn profile (see Figures 3.4, 3.9 and 3.11). In the clean spectra, the relative flux ratio between the two peaks is roughly about a factor of 3. The two peaks are an indication that the observed cold molecular gas has a velocity structure with at least two resolved velocity components. Compared to the systemic velocity at redshift $z = 2.3221$, this amounts to a negative and a positive velocity component. The negative component, at higher frequency, is detected with a signal-to-noise ratio of about 1-2 and the positive component, at lower frequency, is detected with a signal-to-noise ratio of about 3-5. Because the lower frequency component, which moves away from us in the line of sight, is stronger, Doppler beaming is not a valid explanation. A possible explanation could be differential magnification. If the gas responsible for the lower frequency peak is located closer to the caustics of the lens galaxy, its emission is magnified more strongly than the emission from the gas responsible for the higher frequency peak. However, this would require the two emission regions to be spatially offset, which our observations can only marginally support, see Figure 4.1. Higher angular resolution observations of the CO(1-0) emission are needed to verify the spatial offset. Differential magnification has been reported in other systems (e.g. Spingola et al. in prep.; Paraficz et al. 2018; Riechers et al. 2011). To investigate whether differential magnification could cause the asymmetry in the CO(1-0) spectra, the lens galaxy should be modelled to reconstruct the source plane. However, we only have two images of HE1104−1805, leaving us with few constraints on the lens mass model (Lehár et al. 2000). Although differential magnification is certainly a possible explanation, we cannot know for sure without proper lens modelling.

Aside from cleaning, another way to improve the spectral line signal-to-noise is through averaging the velocity cube over frequency (radio velocity). By creating larger bins, the noise becomes smoother and fluctuates less extreme, increasing the spectral line signal-to-noise per channel. However, averaging also removes features from the spectral line and can even remove the double horn structure if overdone. We averaged all the measurement sets down to 64 channels ($\sim$17.3 km s^{-1} width) per spectral window, leaving more than enough spectral resolution without being dominated by noise spikes.

There is a slight disagreement between the redshifts as determined from the spectra of the D and C-configuration (see Tables 3.5 and 3.7). Inspection of the raw spectra leads us to the conclusion that there is a frequency offset of about 40 km s^{-1} in the CO(1-0) spectra between the two observations, which can explain the differences between the determined redshifts.

4.1.2 Structure of the Velocity Field

The velocity fields, as presented in this thesis, all show gradients at each image of the source quasar, indicative of a possible rotational velocity structure, consistent with the obtained spectra. However, the gradients are strongly positively dominated, caused by the asymmetry in the double horn profiles. The

negative velocity component is often completely lost in the 3σ, 4σ or 5σ detection limits. The dispersion fields all show a central peaked velocity dispersion, with often a constant surrounding value. This is indicative of more chaotic motion in the AGN, caused by the presence of a SMBH, accelerating the matter to high speeds. Although the CO molecule is not expected to survive close to the SMBH, the inner parts of the traced CO region can still be accelerated sufficiently to give a higher velocity dispersion than its surrounding. However, aside from a rotational velocity structure, other structures can also satisfy the found structure in the velocity fields and spectra, such as an in- or outflow. To verify which velocity structure is present a lens model analysis (of higher angular resolution observations) should be carried out. If it turns out the gas is indeed differentially magnified, then a source plane reconstruction should yield more symmetric CO(1-0) spectra. This would allow us to create velocity fields containing both components and to further investigate the velocity structure of HE1104−1805.

We can investigate the two velocity components further by imaging them separately. Separate moment 0 maps are shown in Figure 4.1. Overlaying the velocity component maps with the contours of the other shows there is a marginal offset between the emission region of the two components. To further verify this spatial offset, higher angular resolution observations are required.

To construct reliable moment maps we need a sufficiently high signal-to-noise ratio in the channel maps of the constructed velocity cubes. However, some cubes include a noise spike in the channel selection (e.g. Figure 3.4 at around -250 km s^{-1}). This kind of spiky noise structure can inject false structures into the moment maps, as can be seen in Figure 3.12. Luckily, most of these injected structures are lost when taking higher detection limits, as Figure 3.12 clearly shows as well. However, by being restrained to use only the higher detection limits we are left with smaller regions and hence less data, decreasing the spatial resolution of the map. Furthermore, we quickly lose the negative velocity component at higher detection limits. Nevertheless, it should be said that no moment map is dominated by noise structure, that the created velocity fields all show a reoccurring positively dominated velocity gradients and that the dispersion fields all show peaked central velocity dispersions.

4.2 Molecular Gas

To determine some source characteristics, often the CO line luminosity is used as a proxy measure for the present gas mass in the system. The CO line luminosity can be derived from the integrated flux density measurements of the CO(1-0) moment 0 maps using

$$\left(\frac{L'_{\rm CO}}{1\ {\rm K\ km\ s^{-1}\ pc^2}}\right) = 3.25\times10^7 \left(\frac{S_{\rm CO}\Delta v}{1\ {\rm Jy\ km\ s^{-1}}}\right)\left(\frac{\nu_{\rm obs}}{1\ {\rm GHz}}\right)^{-2}\left(\frac{D_{\rm L}}{1\ {\rm Mpc}}\right)^2 (1+z)^{-3}, \tag{4.1}$$

where $S_{\rm CO}\Delta v$ is the integrated flux of the line, $\nu_{\rm obs}$ the observing frequency, D_L the luminosity distance and z the source redshift (Solomon & Vanden Bout 2005). From the clean C&D-configuration tapered moment 0 map with magnified integrated flux $\mu S_{1-0}\Delta v = 0.49\pm0.05$ Jy km s^{-1} we obtain an apparent CO luminosity of $\mu L'_{\rm CO} = (1.32\pm0.13)\times10^{11}$ K km s^{-1} pc^2. The intrinsic CO luminosity can be retrieved by correcting for the magnification,

$$L'_{\rm int} = \frac{L'_{\rm app}}{\mu}. \tag{4.2}$$

Assuming a standard estimated magnification of $\mu_{\rm est} = 10\pm5$, we determine an intrinsic CO luminosity of $L_{\rm CO} = (1.3\pm0.7)\times10^{10}$ K km s^{-1} pc^2. This is consistent with the value determined by Sharon et al. (2016) of $L'_{\rm CO(1-0)} = (1.4\pm0.2)\times10^{10}$ K km s^{-1} pc^2.

We can use the derived CO luminosity to derive an estimate of the total molecular gas mass (H_2 and He). This can be done using the empirical mass-to-CO luminosity relation, expressed as

$$M_{\rm gas} = \alpha_{\rm CO} L'_{\rm CO}, \tag{4.3}$$

where $\alpha_{\rm CO}$ is determined observationally. For the Milky Way Bolatto et al. (2013) found that $\alpha_{\rm CO} = 4.3$ M$_\odot$ (K km s^{-1} pc^2)$^{-1}$, whereas for high redshift starburst galaxies a conversion factor of $\alpha_{\rm CO} = 0.8$ M$_\odot$ (K km s^{-1} pc^2)$^{-1}$ is often used, as derived by Downes & Solomon (1998) from local ultra-luminous

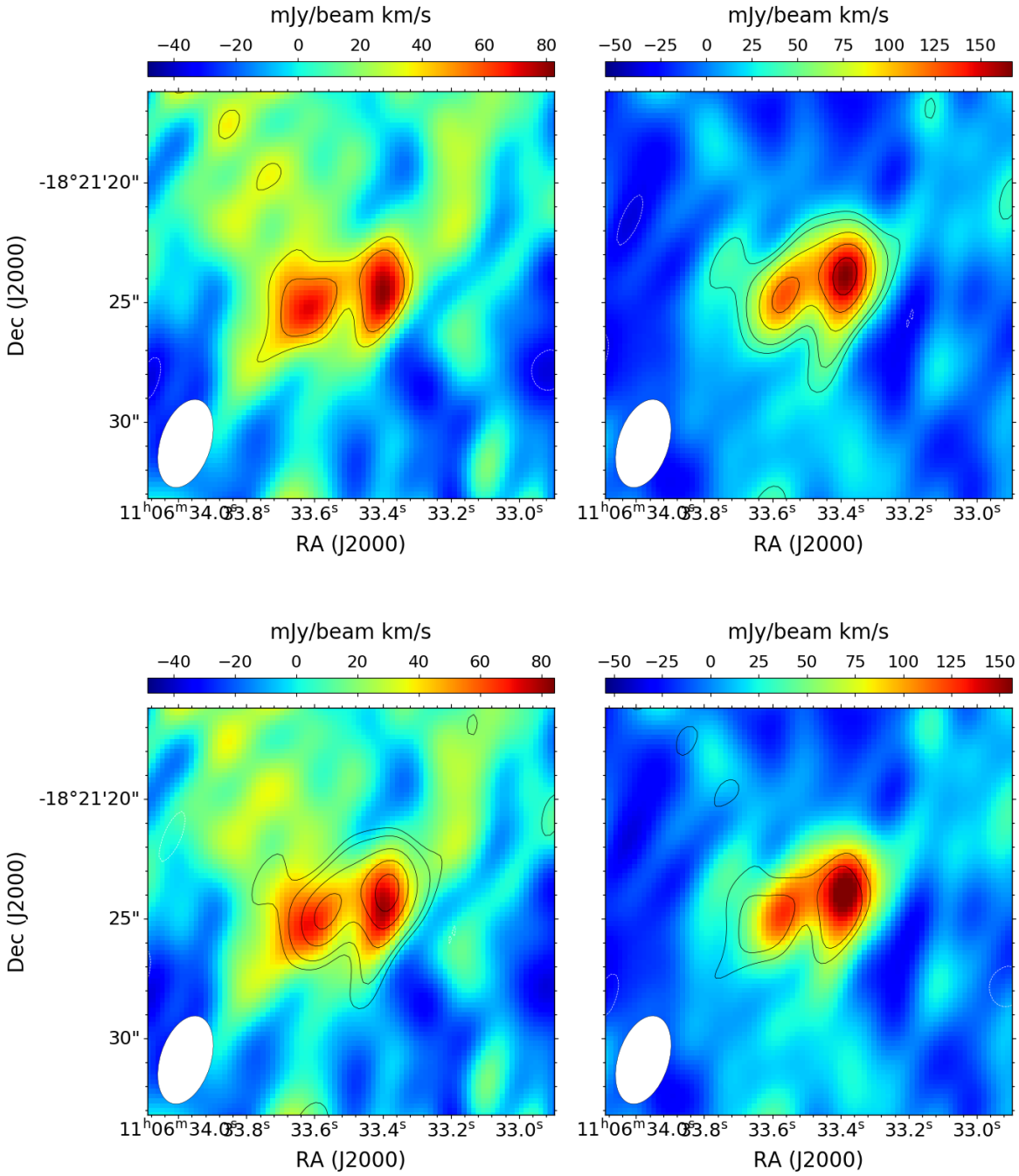

Figure 4.1: Velocity integrated zeroth moment maps of the CO(1-0) emission using only the higher frequency peak (left) and lower frequency peak (right) from the **clean D-configuration** natural data. The top row maps are overlaid with their own contours and the bottom row maps are overlaid with the contours of the other frequency peak. The bottom row maps clearly show the marginal offset between the two peaks. Contours are in levels of $\pm 2\sigma$, $\pm 3\sigma$, $\pm 5\sigma$, $\pm 7\sigma$ and $\pm 9\sigma$, where σ is the RMS of the moment 0 map. The maps are Nyquist sampled with respect to our Nyquist criterion. Beam sizes are shown at the lower left and are 3.80×2.11 arcsec^2 at a position angle of -17.75 deg for all maps.

Table 4.1: Summary of derived quantities from the clean C&D-configuration CO(1-0) moment 0 map and continuum map integrated flux densities as presented in Table 3.3. Along with derived quantities from the infrared luminosity as determined by Stacey et al. (2018).

Weighting	$\mu L'_{\rm CO}$ (10^{10} K km s^{-1} pc^2)	$M_{\rm gas}$ (10^9 M$_\odot$)	$\mu L_{1.4\rm GHz}$ (10^{25} W Hz^{-1})	$\mu L_{\rm IR}$ (10^{13} L$_\odot$)	$q_{\rm IR}$	SFR (M$_\odot$ yr^{-1})
Natural	5.4 ± 0.5	4.3 ± 2.2	2.4 ± 1.4	3.17 ± 0.29	2.16 ± 0.27	5.5 ± 2.8
2″ Taper	13.2 ± 1.3	11 ± 5	2.9 ± 1.8	3.17 ± 0.29	2.05 ± 0.27	5.5 ± 2.8

infrared galaxies. However, more recent studies (Narayanan et al. 2012) have shown that this assumption does not generally hold on an individual basis for observed high redshift AGN. Furthermore Narayanan et al. (2012) argues that the conversion factor requires a more complex description than the simple bimodal model commonly used.

Sticking to the bimodal model and using the conversion factor for high redshift starburst galaxies of $\alpha_{\rm CO} = 0.8$ M$_\odot$ (K km s^{-1} pc^2)$^{-1}$, we derive a gas mass of $M_{\rm gas} = (1.1 \pm 0.5) \times 10^{10}$ M$_\odot$, which is consistent with the gas mass found in local ultra-luminous infrared galaxies (ULIRGs) of $\sim 10^9$-10^{10} M$_\odot$ (Papadopoulos et al. 2012). However, it is slightly below the typical gas mass found in intermediate and high redshift (z = 1-3) ULIRGs of $\sim 10^{10}$-10^{11} M$_\odot$ Tacconi et al. (2013). A summary of the obtained results is presented in 4.1.

4.3 Star Formation

4.3.1 Radio-Infrared Luminosity Relation

Assuming the continuum radio emission follows a simple power-law of the form

$$S_\nu \propto \nu^\alpha, \tag{4.4}$$

where α is the spectral index of the source, the emission at a certain frequency can be extrapolated to another (nearby) frequency. We assume $\alpha = -0.70 \pm 0.14$, a typical value for starburst galaxies (Stacey et al. 2018). The 1.4 GHz data from NVSS yields no clear detection up to 3σ. With $\sigma \approx 0.5$ mJy we can assume an upper limit flux density of $\mu S_{1.4\rm GHz} < 1.5$ mJy. Comparing this to the measured integrated flux density at 34.7 GHz of the clean C&D-configuration tapered data of $\mu S_{34.7\rm GHz} = 100 \pm 10$ μJy gives a lower limit on the spectral index of $\alpha > -0.84$, which implies the used assumption is not unreasonable. Using this power-law, we extrapolate the measured background emission at 34.7 GHz to an emission at 1.4 GHz of $\mu S_{1.4\rm GHz} = 0.9 \pm 0.4$ mJy. Note that these flux densities are still affected by the magnification of the lensing, which is assumed to be constant between these frequencies. This sounds reasonable as gravitational lensing is a purely geometrical event, independent of the frequency of the light affected. However, this assumes that both frequencies are emitted from the same region; if they trace different regions the magnification can be different. However, not having enough information, we assume the dust emission is traced by the molecular gas and hence the CO emission, such that their magnification is the same. For radio sources at cosmological distances, assuming isotropic radiation, the spectral luminosity at rest-frame frequency relates to the flux density at the same observed frequency as

$$L_{1.4\rm GHz} = S_{1.4\rm GHz} \, \frac{4\pi D_{\rm L}^2}{(1+z)^{1+\alpha}}, \tag{4.5}$$

where a k-correction for the spectral index α of the source and a relativistic correction for the frequency shift are applied. Using this relation, we derive a magnified spectral luminosity at 1.4 GHz of $\mu L_{1.4\rm GHz} = (2.9 \pm 1.8) \times 10^{25}$ W Hz^{-1}.

The radio-infrared correlation is defined by Condon et al. (1991) as

$$q_{\rm IR} = \log_{10} \left(\frac{L_{\rm IR}}{3.75 \times 10^{12} L_{1.4\rm GHz}} \right). \tag{4.6}$$

For determining the q_{IR} factor for HE1104−1805, we make use of the magnified FIR luminosity of $\mu L_{FIR} = (1.66 \pm 0.14) \times 10^{13}$ $L_\odot$, as determined from observational data by Stacey et al. (2018). To extrapolate the FIR luminosity of $\mu L_{FIR} = (1.66 \pm 0.15) \times 10^{13}$ $L_\odot$ to the total IR luminosity, we need to correct for the contribution from MIR spectral features. This can be done by applying a colour correction factor of 1.91 as given by Dale et al. (2001) such that

$$L_{IR} = 1.91 L_{FIR}. \tag{4.7}$$

This gives a total magnified infrared luminosity of $\mu L_{IR} = (3.17 \pm 0.29) \times 10^{13}$ $L_\odot$, yielding a radio-infrared correlation of $q_{IR} = 2.05 \pm 0.27$. Ivison et al. (2010) find a median value of $\langle q_{IR} \rangle = 2.40 \pm 0.24$ for a flux-limited sample of star-forming galaxies selected from 250 μm *Herschel*/SPIRE data with 1.4 GHz VLA flux densities. We found a radio-infrared correlation consistent within 2σ, with a slight radio-excess for HE1104−1805 compared to their sample population. As our target is radio-quiet, it has little to no radio emission from possible jets and thus the radio-excess is likely contributed by AGN activity or synchrotron emission due to star formation

Assuming a Salpeter initial mass function, an estimation of the SFR is defined by Robert C. Kennicutt (1998) as

$$\mathrm{SFR}(M_\odot\ \mathrm{yr}^{-1}) = \frac{L_{IR}}{5.8 \times 10^9}, \tag{4.8}$$

where L_{IR} is given in solar luminosities. Again, assuming a standard magnification of $\mu_{est} = 10 \pm 5$ yields an infrared luminosity of $L_{IR} = (3.2 \pm 1.6) \times 10^{12}$ $L_\odot$, resulting in a SFR of $(5.5 \pm 2.8) \times 10^2$ $M_\odot$ yr^{-1}. In typical spiral galaxies the SFR is about a few solar masses per year. For HE1104−1805, this is a good two orders of magnitudes higher, indicating it might be in a starburst phase. A summary of the obtained results is presented in Table 4.1.

4.3.2 Kennicutt-Schmidt (K-S) Relation

The Kennicutt-Schmidt (K-S) relation is an empirical law relating the gas density and the SFR density in a given region. The relation, as first examined by Schmidt (1959), states that the SFR surface density scales as some positive power n of the local gas surface density,

$$\Sigma_{SFR} \propto (\Sigma_{gas})^n, \tag{4.9}$$

where Σ_{SFR} is the SFR surface density in $M_\odot$ yr^{-1} pc^{-2} and Σ_{gas} the gas surface density in g pc^{-2}. Kennicutt (1998) examined nearly 100 nearby galaxies to estimate a scaling power of $n = 1.4 \pm 0.15$. However, as expressed in Eq. 4.3, the gas mass can be directly related to the integrated CO line luminosity using CO-H_2 conversion factors. Furthermore, as expressed in Eq. 4.8, the SFR can be directly related to the IR luminosity. This implies we also expect a relation between the observed integrated CO line luminosity and the IR luminosity similar to the K-S relation. The advantage of this variant is that it relies only on directly observed quantities. Figure 4.2 shows the observed IR and CO luminosities of HE1104−1805 for the clean C&D-configuration 2″ tapered data. The observed values are compared to other galaxy samples that have comparable observations of low-J CO lines: high redshift (z = 2-3) AGN and SMGs (Sharon et al. 2016), low redshift ($z < 1$) luminous infrared galaxies (LIRGs) (Papadopoulos et al. 2012), main sequence galaxies at redshifts z = 1-2 (Leroy et al. 2008), local ULIRGs (Solomon et al. 1997) and high redshift radio loud AGN (Spingola et al. in prep.). Two K-S relations are also plotted (Aravena et al. 2016), one for local spiral galaxies following

$$\log_{10} L_{IR} = 1.12 \log_{10} L'_{CO} + 0.5 \tag{4.10}$$

and one for high redshift disk galaxies,

$$\log_{10} L_{IR} = 1.12 \log_{10} L'_{CO} + 1.0, \tag{4.11}$$

which is representative of a higher star formation efficiency and consistent with high redshift AGN and local ULIRGs, often assumed to resemble compact starbursts at high redshift (Bothwell et al. 2013).

The star formation efficiency (SFE) is commonly defined as the ratio between the SFR and the molecular gas mass of a region,

$$\mathrm{SFE} = \mathrm{SFR}/M_{\mathrm{gas}}, \tag{4.12}$$

often expressed in units of yr^{-1}. Taking the inverse of the SFE gives an indicative timescale over which the galaxy's gas reservoir will be depleted, assuming a constant SFR. For our measurements of HE1104−1805, we derive this timescale to be $\tau_{\mathrm{SFR}} = 19.3 \pm 2.6$ Myr, which is quite short on cosmic timescales. Using the same reasoning as for the K-S relation, the IR and CO luminosities can be used as a proxy indicator for the SFE as

$$\mathrm{SFE} \propto L_{\mathrm{IR}}/L'_{\mathrm{CO}}, \tag{4.13}$$

often expressed in units of $\mathrm{L}_{\odot}$ $(\mathrm{K\ km\ s^{-1}\ pc^2})^{-1}$. Using this proxy one can obtain more information from the position of an object in Figure 4.2. Objects with a low SFE are positioned more to the bottom-right of the plot as their $L_{\mathrm{IR}}/L'_{\mathrm{CO}}$ decreases and may experience long-lasting, but slow star formation, whereas objects with a high SFE are positioned more to the top-left of the plot and may experience short-lived bursts of fast star formation. The latter of which can be caused by, for example, galaxy mergers or positive AGN feedback, whereas a reduced SFE can be caused by, for example, negative AGN feedback.

In the $L_{\mathrm{IR}} - L'_{\mathrm{CO}}$ plane (see Fig. 4.2) HE1104−1805 is positioned close to the mean value for local ULIRGs and at a higher SFE than the K-S relation for high redshift disk galaxies, indicating it might be a starburst. As it is positioned close to the mean value for local ULIRGs, the assumed conversion factor of $\alpha_{\mathrm{CO}} = 0.8\ \mathrm{M}_{\odot}\ (\mathrm{K\ km\ s^{-1}\ pc^2})^{-1}$ might be suitable for HE1104−1805. The shown uncertainties have no influence on the SFE as their main contributor is the estimated magnification factor of $\mu_{\mathrm{est}} = 10 \pm 5$. Assuming this factor is the same for the IR and CO line emission, this will only displace its position on the $L_{\mathrm{IR}} - L'_{\mathrm{CO}}$ plane nearly along the K-S relation and hence keep its SFE constant. However, a significant difference between μ_{IR} and μ_{CO} might affect its SFE beyond the K-S relation.

Compared to a similar population of AGN at z = 2-3 (Sharon et al. 2016), HE1104−1805 shows a deficit in both IR and CO luminosity of about a factor of 4. This might seem inconsistent, however, the deficit can be explained by the fact that we have observed a lensed AGN, whereas the plotted data from Sharon et al. (2016) are unlensed AGN. Since they observed unlensed AGN, their sample selection suffered from Malmquist bias as the unlensed less luminous AGN population at redshift z = 2-3 is too faint to be observed with current sensitivity limits.

4.4 Origin of the Continuum Emission

The observed 34.7 GHz continuum (115.3 GHz in source rest-frame) has multiple components: thermal emission by heated dust, which is linked to star formation, synchrotron emission by AGN activity, synchrotron emission by star forming regions and free-free emission. As HE1104−1805 is radio-quiet and has no detectable jets in the optical and radio regime, it is not dominated by synchrotron emission from the jets. To find out some more about its radio emission, we can take a look at its structure (extended or compact emission), the presence of X-ray emission and the spectral energy distribution (SED) in the radio regime. First, it is important to note that from our observations, it becomes clear that there is no significant contribution to the measured continuum by the lensing galaxy, as we do not observe it, see Figs. 3.2, 3.8 and 3.10. Moreover, recent Gaia observations have not detected the lensing galaxy either (Lemon et al. 2018, 2019).

The structure of the continuum emission is expected to be extended if dominated by star formation, as it would trace the extended cold molecular gas and expected to be compact if dominated by AGN activity or free-free emission as this is limited to a more compact region in the AGN. A comparison of the moment 0 maps and continuum maps (see most notably Figure 3.10) indicates the continuum originates from a slightly more compact region. However, the difference seems small and is not consistent over all imaging, see Figure 3.2, such that it might be an artefact of the imaging process. More interestingly, in the C-configuration observation (see Figure 3.7) we see that the CO(1-0) is barely detected, whereas the continuum is still detected clearly. This can be an indication that the CO(1-0) emission is mostly being resolved out at the angular resolution of the C-configuration, whereas the continuum emission is not. This makes sense if the continuum emission originates from a more compact region than the region spanned by the cold molecular gas, as traced by CO(1-0). Therefore, the C-configuration observation

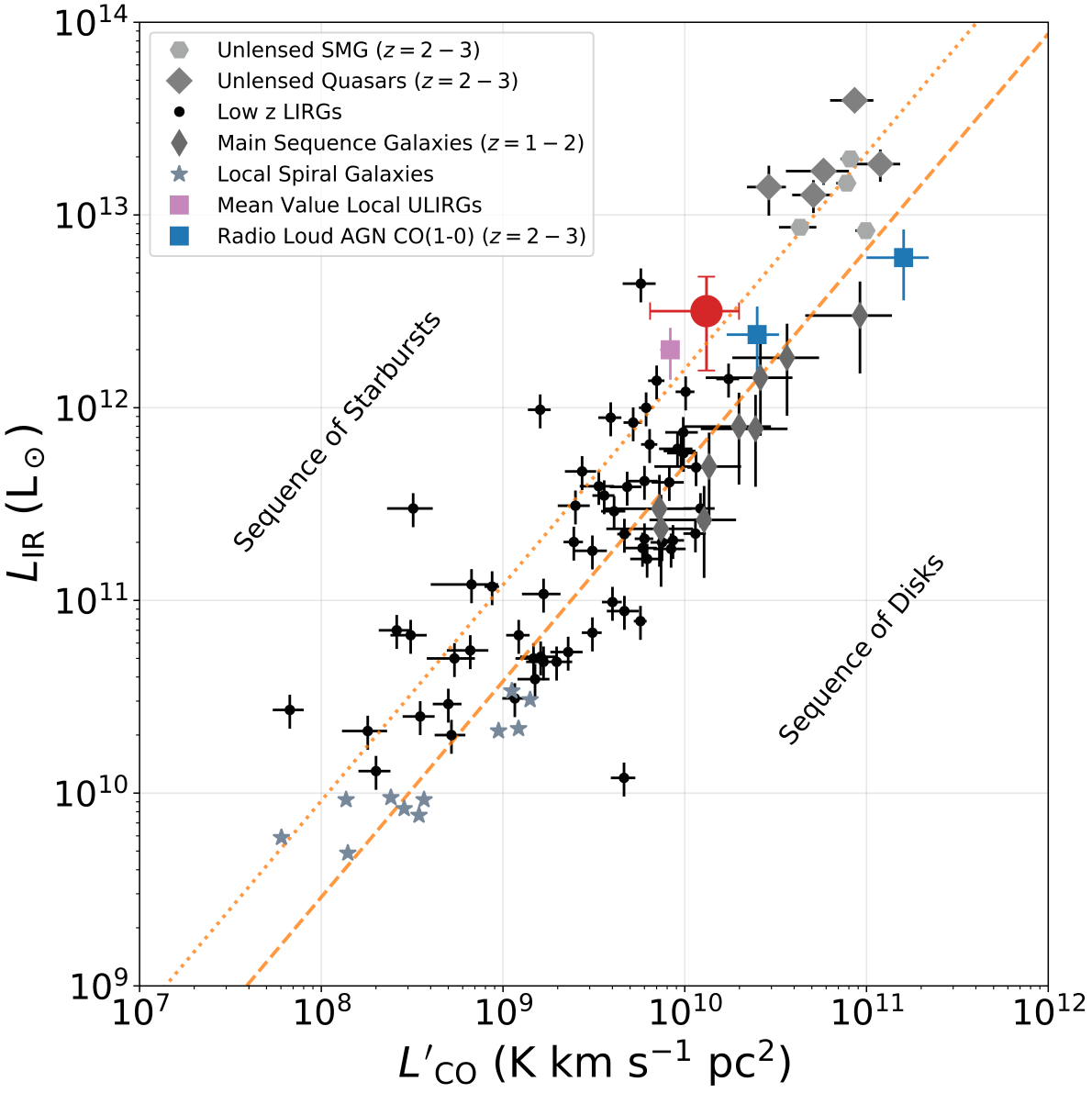

Figure 4.2: The infrared luminosity (integrated from 8 to 1000 μm), $L_{\rm IR}$, versus integrated CO line luminosity, $L'_{\rm CO}$, for different unlensed galaxy populations. The red circle represent the derived values from the 2″ tapered clean C&D-configuration data. Two variants of the K-S relation are plotted, the dashed line for local spiral galaxies (Eq. 4.10) and the dotted line for high redshift disk galaxies (Eq. 4.11) (Aravena et al. 2016). The K-S relations divide the $L_{\rm IR}$-$L'_{\rm CO}$ plane into a sequence of starbursts with high SFE and a sequence of disks with low SFE. Data taken (in order of legend labels) from Sharon et al. (2016), Papadopoulos et al. (2012), Daddi et al. (2010), Leroy et al. (2008), Solomon et al. (1997) and Spingola et al. (in prep.).

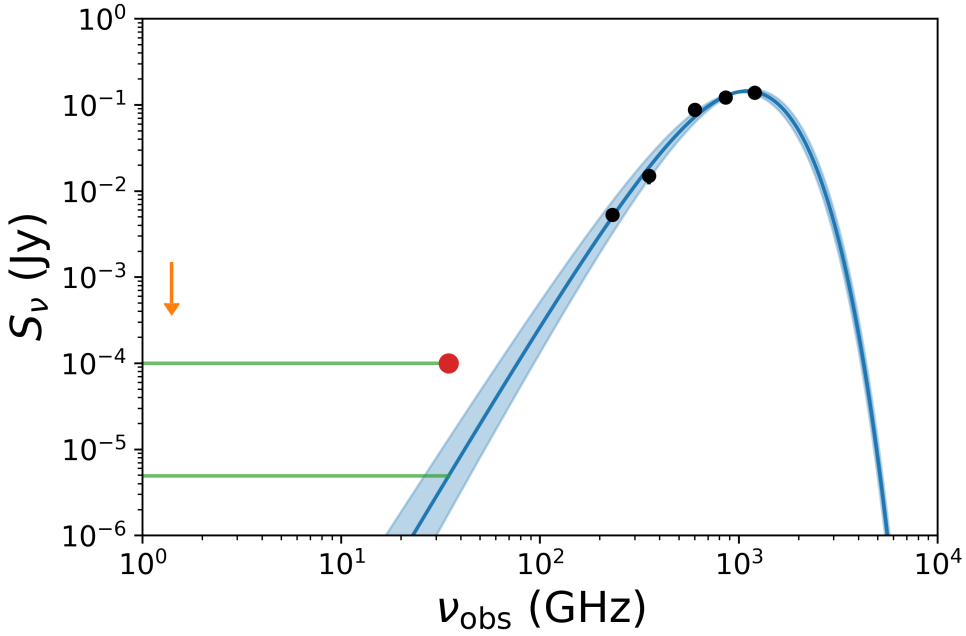

Figure 4.3: Fitted modified black-body Spectral Energy Distribution (SED) to describe the heated dust component, with dust temperature $T_{\rm d} = 36.1 \pm 4.1$ K and emissivity index $\beta = 1.9 \pm 0.3$. Data and best fit parameters are taken from Stacey et al. (2018). The shaded region represents the uncertainty in the SED fit. The red data point is the continuum measurement from this thesis, the clean C&D-configuration 2″ tapered data, and the orange upper limit is the NVSS non-detection. This plot clearly shows that the continuum emission is not dominated by the heated dust component, which indicates it might be dominated by AGN activity or synchrotron emission from star formation.

might be an indication that the continuum is largely due to AGN activity instead of star formation. Observations at higher angular resolution should be made to verify this.

If there is emission due to AGN activity, we should also be able to directly observe X-ray emission from a compact region in the AGN. Using a stacking analysis of *Chandra* observations Walton et al. (2015) show there is in fact X-ray emission originating from HE1104−1805. However, as they do not discuss the results for their targets individually, the origin of the X-ray emission has not yet been defined.

Star formation heats up patches of dust throughout the molecular gas region, such that we can observe thermal emission from the heated dust, usually in the (far-)infrared regime (in the source rest-frame). Stacey et al. (2018) used infrared *Herschel*/SPIRE observations to fit a modified black body to describe the heated dust emission,

$$S_\nu \propto \frac{\nu_0^{3+\beta}}{e^{h\nu_0/kT_{\rm d}} - 1}, \tag{4.14}$$

where ν_0 is the rest-frame frequency, which is related to the observed frequency by Eq. 2.11, β the emissivity index and $T_{\rm d}$ the (effective) dust temperature. They found best fit values of $T_{\rm d} = 36.1 \pm 4.1$ K and $\beta = 1.9 \pm 0.3$, as shown in Figure 4.3. Also shown in Figure 4.3 is our measurement of the continuum emission at an observed frequency of 34.7G GHz. The plot clearly shows that the continuum emission is not dominated by the heated dust component, which indicates it might be dominated by either synchrotron from star formation, AGN activity or free-free emission instead.

In Figure 4.4, the clean natural weighted moment 0 map is presented overlaid with continuum emission contours. Although the CO emission is clearly associated with the synchrotron continuum, the emission peaks are slightly spatially offset. A similar spatial offset is found between the continuum and the CO(3-2) emission, as observed by Riechers (2011). They argue this could be an indication that the AGN might not reside in the centre of the molecular gas reservoir as traced by the CO(1-0) emission. Another explanation might be that the offset is be caused by smaller scale dynamics of the molecular gas being

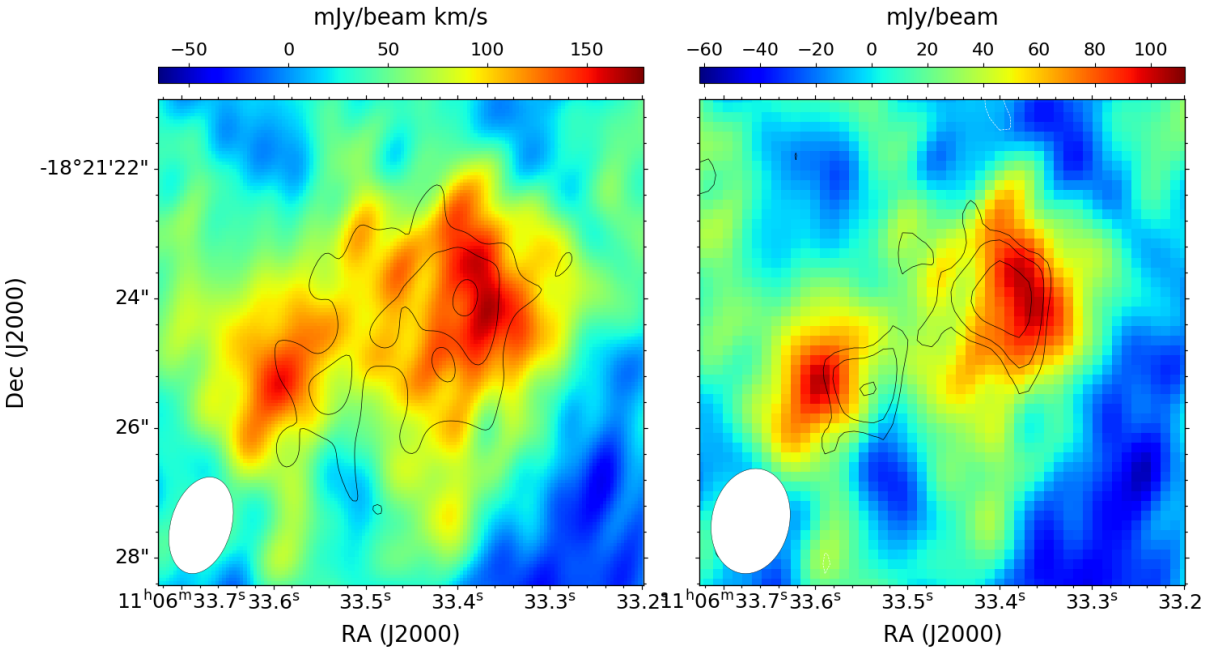

Figure 4.4: The dirty (left) and clean (right) natural weighted moment 0 map with continuum contours for the C&D-configuration observation. Note the position offset between the line and continuum emission. In the clean moment 0 map the separation of the two line images is $\Delta\theta_{1-0} = 3.4 \pm 0.3$ arcsec, whereas for the continuum it is $\Delta\theta_{34.7GHz} = 2.5 \pm 0.3$ arcsec. Although the offset can be explained by a different emission region the different separation is an unexpected result. Contours are in levels of $\pm 2\sigma$ through $\pm 5\sigma$, in steps of 1σ, where σ is the RMS of the continuum map. Beam sizes are shown at the lower left. The maps are Nyquist sampled with respect to our Nyquist criterion.

averaged over in the moment 0 map. To determine whether this is the case, observations at higher spatial resolution and sensitivity should be carried out to be able to study the structure and dynamics of the molecular gas reservoir in more detail.

More alarming is the different separations between the images in the moment 0 and continuum maps. In the moment 0 map the images are separated by $\Delta\theta_{1-0} = 3.4 \pm 0.3$ arcsec (see Figure 3.2), whereas in the continuum map they are separated by $\Delta\theta_{34.7GHz} = 2.5 \pm 0.3$ arcsec (see Figure 3.10). The moment 0 map separation is consistent with the literature value of $\Delta\theta = 3.19 \pm 0.03$ arcsec (Kochanek et al. 1999), but the continuum is only consistent within 3σ. The separation between the two images is expected to be equal to twice the Einstein radius as determined by Eq. 1.9, which is independent of frequency and unaffected by the relatively miniscule difference in luminosity distances of the emission regions. Assuming Eq. 1.9 and its implicit approximations hold, this can imply the emission region of the continuum is located at a different redshift to produce an image separation different from the moment 0 map separation and is thus might not be associated with the CO line emission. This, however, should be further investigated using higher angular resolution observations of both the CO(1-0) line emission and the continuum emission, before any definitive claim can be made.

Chapter 5

Conclusions

Using 34.7 GHz VLA observations in C and D-configuration, we are able to detect the gravitationally lensed quasar HE1104−1805. After the data calibration, the analysis of the constructed moment maps and continuum maps yields the following:

- ◇ We find the two images of the CO(1-0) emission to be separated by $\Delta\theta_{1-0} = 3.0 \pm 0.3$ arcsec in the D-configuration moment 0 map and by $\Delta\theta_{1-0} = 3.4 \pm 0.4$ arcsec in the C&D-configuration moment 0 map. Both are consistent within 1σ with the separation in optical observations of $\Delta\theta = 3.19 \pm 0.03$ arcsec.

- ◇ The spectra show a highly asymmetric double horn profile, clearly showing the presence of two resolved peaks. This indicates the velocity structure has at least two components: one with a negative line-of-sight velocity and one with a positive line-of-sight velocity. The lower frequency (or positive velocity) peak is detected about thrice as strong as the higher frequency peak. This can be explained by differential magnification or an in- or outflow of gas.

- ◇ All created velocity fields show positively dominated gradients along the images. The negative velocity component is lost in the presented velocity fields because of its low signal-to-noise ratio. All dispersion fields show a central peaked dispersion velocity, indicating a more chaotic gas motion in the AGN region. Furthermore, we find a marginal spatial offset between the negative and positive velocity components of the CO(1-0) emission.

- ◇ Using the measured (magnified) integrated flux density of the CO(1-0) emission of $\mu S_{1-0}\Delta v = 0.49 \pm 0.05$ Jy km s^{-1}, we obtain an apparent CO luminosity of $\mu L'_{\mathrm{CO}} = (1.32 \pm 0.13) \times 10^{11}$ K km s^{-1} pc^2. To obtain the gas mass of HE1104−1805, we use a CO-H_2 conversion factor of $\alpha_{\mathrm{CO}} = 0.8\ \mathrm{M}_\odot\ (\mathrm{K\ km\ s^{-1}\ pc^2})^{-1}$, empirically derived from local ULIRGs, and a common estimated magnification factor to find $M_{\mathrm{gas}} = (1.1 \pm 0.5) \times 10^{10}\ \mathrm{M}_\odot$.

- ◇ Assuming a spectral index of $\alpha = -0.70 \pm 0.14$, we extrapolate our measured (magnified) integrated flux density of $S_{34.7\mathrm{GHz}} = 100 \pm 10$ μJy from the continuum emission at 34.7 GHz to 1.4 GHz, $\mu S_{1.4\mathrm{GHz}} = 0.9 \pm 0.4$ mJy. We relate this to the rest-frame luminosity, which gives $\mu L_{1.4\mathrm{GHz}} = (2.9 \pm 1.8) \times 10^{25}$ W Hz^{-1}. Using the far-infrared luminosity as derived by Stacey et al. (2018), we arrive at a radio-infrared correlation factor of $q_{\mathrm{IR}} = 2.05 \pm 0.27$, consistent with the population of star-forming galaxies.

- ◇ We position HE1104−1805 in the $L_{\mathrm{IR}} - L'_{\mathrm{CO}}$ plane against the K-S relation for high redshift disk galaxies to find it close to the mean position for local ULIRGs, but with an increased SFE, which indicates HE1104−1805 might be a starburst galaxy. This in turn might be indicative of a past merger or positive AGN feedback.

- ◇ We find the continuum emission to be more compact than the CO(1-0) emission, indicating it largely originates from a more compact region than the cold molecular gas, most likely the AGN region. Comparing our measured continuum emission to a fit of the heated dust emission, shows

us that the continuum emission is not dominated by the heated dust component. Furthermore, we find a slight spatial offset between the CO(1-0) emission and the continuum emission.

For further research into HE1104−1805 we should consider new observations at a higher angular resolution than used in this thesis. A possibility might be a VLA observation in B-configuration or combined B&C-configuration, or a Very Long Baseline Interferometer (VLBI) observation. We can use these observations to further inspect the velocity structure of the cold molecular gas and the origin of the continuum emission. It might also be interesting to use these observations to build a lens model and to reconstruct the source plane of HE1104−1805. We can use this reconstruction to further investigate the velocity structure and to estimate the dynamical mass, and hence also the gas fraction, of the quasar and compare it to similar populations, to help verify if HE1104−1805 is a disk or a starburst galaxy.

References

Aravena, M., Spilker, J. S., Bethermin, M., et al. 2016, MNRAS, 457, 4406

Berciano Alba, A. 2009, PhD thesis, relation: https://www.rug.nl/ Rights: University of Groningen

Bolatto, A. D., Wolfire, M., & Leroy, A. K. 2013, ARA&A, 51, 207

Bothwell, M. S., Smail, I., Chapman, S. C., et al. 2013, MNRAS, 429, 3047

Casey, C. M., Narayanan, D., Carilli, C., et al. 2018, in Astronomical Society of the Pacific Conference Series, Vol. 517, Science with a Next Generation Very Large Array, ed. E. Murphy, 629

Condon, J. J., Anderson, M. L., & Helou, G. 1991, ApJ, 376, 95

Croton, D. J., Springel, V., White, S. D. M., et al. 2006, MNRAS, 365, 11

Daddi, E., Elbaz, D., Walter, F., et al. 2010, ApJ, 714, L118

Dale, D. A., Helou, G., Contursi, A., Silbermann, N. A., & Kolhatkar, S. 2001, ApJ, 549, 215

Downes, D. & Solomon, P. M. 1998, ApJ, 507, 615

Dyson, F. W., Eddington, A. S., & Davidson, C. 1920, Philosophical Transactions of the Royal Society of London Series A, 220, 291

Hirschmann, M., Dolag, K., Saro, A., et al. 2014, MNRAS, 442, 2304

Högbom, J. A. 1974, A&AS, 15, 417

Ishibashi, W. & Fabian, A. C. 2012, MNRAS, 427, 2998

Ivison, R. J., Magnelli, B., Ibar, E., et al. 2010, A&A, 518, L31

Kennicutt, Jr., R. C. 1998, ApJ, 498, 541

Kochanek, C. S., Falco, E. E., Impey, C., et al. 1999, The CASTLES Survey, `https://www.cfa.harvard.edu/castles/`, accessed: 10-06-2019

Lehár, J., Falco, E. E., Kochanek, C. S., et al. 2000, ApJ, 536, 584

Lemon, C. A., Auger, M. W., & McMahon, R. G. 2019, MNRAS, 483, 4242

Lemon, C. A., Auger, M. W., McMahon, R. G., & Ostrovski, F. 2018, MNRAS, 479, 5060

Leroy, A. K., Walter, F., Brinks, E., et al. 2008, AJ, 136, 2782

Lidman, C., Courbin, F., Kneib, J. P., et al. 2000, A&A, 364, L62

Mollerach, S. & Roulet, E. 2002, Gravitational lensing and microlensing (Singapore: World Scientific)

Narayan, R. & Bartelmann, M. 1996, arXiv e-prints, astro

Narayanan, D., Krumholz, M. R., Ostriker, E. C., & Hernquist, L. 2012, MNRAS, 421, 3127

Papadopoulos, P. P., van der Werf, P. P., Xilouris, E. M., et al. 2012, MNRAS, 426, 2601

Paraficz, D., Rybak, M., McKean, J. P., et al. 2018, A&A, 613, A34

Perley, R. A. & Butler, B. J. 2013, ApJS, 204, 19

Planck Collaboration, Ade, P. A. R., Aghanim, N., et al. 2016, A&A, 594, A13

Riechers, D. A. 2011, ApJ, 730, 108

Riechers, D. A., Hodge, J., Walter, F., Carilli, C. L., & Bertoldi, F. 2011, ApJ, 739, L31

Robert C. Kennicutt, J. 1998, The Astrophysical Journal, 498, 541

Schmidt, M. 1959, ApJ, 129, 243

Sharon, C. E., Riechers, D. A., Hodge, J., et al. 2016, ApJ, 827, 18

Solomon, P. M., Downes, D., Radford, S. J. E., & Barrett, J. W. 1997, ApJ, 478, 144

Solomon, P. M. & Vanden Bout, P. A. 2005, ARA&A, 43

Spingola, C., McKean, J. P., Vegetti, S., et al. in prep., submitted to MNRAS, 2019arXiv190506363

Stacey, H. R., McKean, J. P., Robertson, N. C., et al. 2018, MNRAS, 476, 5075

Tacconi, L. J., Neri, R., Genzel, R., et al. 2013, ApJ, 768, 74

Walton, D. J., Reynolds, M. T., Miller, J. M., et al. 2015, ApJ, 805, 161

Wisotzki, L., Koehler, T., Kayser, R., & Reimers, D. 1993, A&A, 278, L15

Wutschik, S., Schleicher, D. R. G., & Palmer, T. S. 2013, A&A, 560, A34

Zackrisson, E. 2005

Zernike, F. 1938, Physica, 5, 785